Background Rejection for the Neutrinoless Double Beta Decay Experiment SNO+

Philip G. Jones

Lincoln College, Oxford

Thesis submitted in partial fulfilment of the requirements for the degree of Doctor of Philosophy at the University of Oxford

Michaelmas Term, 2011

Background Rejection for the Neutrinoless Double Beta Decay Experiment SNO+

Philip G. Jones
Lincoln College, Oxford

Thesis submitted in partial fulfilment of the requirements for the degree of Doctor of Philosophy at the University of Oxford

Michaelmas Term, 2011

Abstract

The SNO+ experiment will use a liquid scintillator based detector to study solar, geo, and reactor neutrinos and double beta decay. This thesis discusses the effect of backgrounds on the measurement of neutrinoless double beta decay and describes analysis techniques developed to reduce their impact.

Details of the modeling of the photomultiplier tubes in the SNO+ Monte Carlo RAT are first described and comparisons are made with the SNO Monte Carlo SNOMAN. SNOMAN has been extensively verified with calibration sources and RAT is shown to be in good agreement. The event reconstruction techniques are then presented and predict an achievable 15cm position and 7% energy resolution.

The backgrounds are discussed and pileup backgrounds identified, including many previous unknown pileup backgrounds. Techniques to reject the pileup background are presented and shown to give over 99% rejection in the region of the double beta decay end point (3-4MeV), below the irreducible background from solar neutrinos. Finally the resulting limit on the effective Majorana neutrino mass SNO+ could achieve in 2015 is predicted to be 270meV and this is compared with other experiments that are underway.

Contents

List of Figures

List of Tables

Chapter 1

Neutrinos

1.1 Brief History of Neutrinos

The history of neutrinos began with the observations of beta rays (decays), by C. D. Ellis. C. D. Ellis showed that the beta rays were associated with an internal conversion[1], and later in 1927 with W. A. Wooster that the mean beta energy was only a third of the total allowed[2]. This continuous energy spectrum was contrary to the observed two-body decay, which should result in a discrete spectrum. Two unpleasant solutions were suggested: the law of energy conservation be weakened by N. Bohr, or an electrically neutral *Neutron* is emitted with the electron by W. Pauli in his famous 1930 letter to "...Dear Radioactive Ladies and Gentlemen..."[3].

Pauli's massive *Neutron* served the role of both the neutron and neutrino as we know them today. The discovery of the neutron by J. Chadwick 1932[4] and F. Perrin's 1933 observation that the *Neutron* mass be significantly smaller than the electron[5], separated the ideas of the neutron and *Neutron*. E. Fermi's 1934 theory of beta decay renamed it the neutrino (little neutral one)[6], and gave a theoretical understanding analogous to electromagnetic radiation.

First direct observation of the neutrino would prove to be difficult, indeed in 1934 H. Bethe and R. Peierls calculated the neutrino interaction cross section to be

less than 10^{-44}cm^2 leading them to conclude observation would be impossible[7]. However, 22 years later in 1956 F. Reines and C. Cowan observed inverse beta decay caused by reactor anti-neutrinos, $\bar{\nu} + p \rightarrow n + e^+$. A concurrent experiment in 1955 by R. Davis looked for $\bar{\nu} + {}^{37}\text{Cl} \rightarrow {}^{37}\text{Ar} + e^-$, which was not observed[8], suggesting a neutrino anti-neutrino distinction, as predicted by lepton number conservation introduced in 1953 by E. Konopinski and H. Mahmoud[9].

The neutrino helicity was measured in 1958 by M. Goldhaber *et al.*, to be negative i.e spin anti-parallel to the momentum[10]. Then in 1962 a new distinct type of neutrino, the muon neutrino was discovered by Lederman *et al.* [11]. Following the muon neutrino discovery, Maki, Nakagawa and Sakata suggested these two neutrinos mix[12]. Pontecorvo suggested that neutrinos oscillate, originally proposed between neutrino-anti-neutrino states and later between the flavour states[13].

In 1968 R. Davis *et al.* working on the Homestake experiment measured the solar electron neutrino flux for the first time[14]. The flux was found to be significantly less than that predicted by the solar models, giving rise to the solar neutrino problem. A similar atmospheric neutrino anomaly was subsequently observed in 1988 by the IMB[15] and Kamiokande[16] experiments. In between in 1976 M. Perl *et al.* discovered the tau lepton, evidence that another neutrino type existed[17].

The number of neutrino flavours was set to three in 1989 by LEP[18], suggesting the observed electron, muon, and predicted tau neutrinos are the only flavour neutrinos. Confirmation came in 2000 when the tau neutrino was observed by the DONUT experiment[19]. The LEP result constrains the number of neutrinos which couple to the weak interaction neutral Z boson with a mass less than half that of the Z boson to 3.

The atmospheric neutrino anomaly was solved by Super-Kamiokande in 1998, finding an energy and zenith angle dependent deficit of the muon neutrinos; evidence towards neutrino oscillations and implying a neutrino mass[20, 21]. Shortly

after in 2002 SNO solved the solar neutrino problem, showing a deficit in the electron neutrino flux and no deficit in the muon plus tau neutrino flux, implying oscillation of the electron neutrinos into muon or tau neutrinos[22].

Recently the T2K experiment in Japan has reported a possible appearance of electron neutrinos, having oscillated from muon neutrinos. This allows the T2K experiment to set a tentative non-zero lower limit on mixing angle, θ_{13}[23]. A non zero value is required for CP violation in neutrino oscillation physics.

1.1.1 Neutrino Mass Limits

The neutrino mass has not been directly measured, instead upper limits have been placed via multiple experimental techniques. Furthermore, only since the neutrino oscillation observations has it been known that neutrinos have mass, with the previous standard model assuming massless neutrinos. Even so the mass is experimentally known to be very small compared with other existing fermions.

Beta Decay Limits

Beta decay is the process whereby a down quark in a nucleus transforms via a weak interaction into an up quark emitting an electron and electron anti-neutrino. A Kurie plot of the distribution of electron energies for a massless neutrino will differ from the same plot with a massive neutrino. This difference is predominantly a small change near the end point of the decay. Hence, as the spectroscopic resolving power is $E/\Delta E$ a small end point decay is preferred, resulting in tritium, $Q_\beta = 18.6$keV, as the isotope of choice for experimental measurements of neutrino mass.

The current best limit $m_\beta < 2$eV at 95% CL[24], is based on the Troitsk[25] and Mainz[26] tritium experimental measurements. The KArlsruhe TRItium Neutrino, KATRIN, experiment expects to lower this limit to $m_\beta < 0.2$eV in 2015, assuming

data taking starts in 2012[27].

Cosmological Limits

Neutrinos are the second most numerous particle in the universe after photons, therefore even a small neutrino mass will constitute a large fraction of the universe. Thus, a large neutrino mass will alter the large scale structure of the universe and give rise to visible structure in the Cosmic Microwave Background. This allows the Wilkinson Microwave Anisotropy Probe, WMAP, to set a limit on the summed neutrino mass $M = \sum_{i=1}^{3} m_i$ at 95% CL as $M < 0.63$eV[28].

1.2 Neutrino Theory

In the standard model of particle physics there are three distinct neutrino flavours, ν_e, ν_μ, ν_τ along with their corresponding anti-neutrinos. These neutrinos only interact with the weak force and gravity, coupling the $W^{\pm}$ and Z bosons to negative chirality neutrinos and positive chirality anti-neutrinos. As neutrinos are massless in the standard model this implies that right handed chiral neutrinos and left handed chiral anti-neutrons are sterile if they exist.

Following the SNO and Super-Kamiokande results neutrinos are known to oscillate and change flavour, thus the neutrino flavour is a weak eigenstate and neutrinos have mass. This oscillation is accounted for by introducing mass eigenstates of the Hamiltonian in free space, these neutrinos ν_1, ν_2, ν_3 with masses m_1, m_2, m_3 are related to the weak eigenstates by (using natural units):

$$|\nu_l\rangle = \sum_{j=1}^{3} U_{lj}^{*} |\nu_j\rangle , \qquad l \in \{e, \mu, \tau\}, \quad j \in \{1, 2, 3\} \tag{1.1}$$

where U_{li} is the PNMS Unitary Matrix:

$$
\begin{aligned}
U_{li} &= \begin{pmatrix} U_{e1} & U_{e2} & U_{e3} \\ U_{\mu 1} & U_{\mu 2} & U_{\mu 3} \\ U_{\tau 1} & U_{\tau 2} & U_{\tau 3} \end{pmatrix} \\
U_{li} &= \begin{pmatrix} 1 & 0 & 0 \\ 0 & c_{23} & s_{23} \\ 0 & -s_{23} & c_{23} \end{pmatrix} \begin{pmatrix} c_{13} & 0 & s_{13}e^{-i\delta} \\ 0 & 1 & 0 \\ -s_{13}e^{i\delta} & 0 & c_{13} \end{pmatrix} \begin{pmatrix} c_{12} & s_{12} & 0 \\ -s_{12} & c_{12} & 0 \\ 0 & 0 & 1 \end{pmatrix} \begin{pmatrix} e^{i\alpha_1/2} & 0 & 0 \\ 0 & e^{i\alpha_2/2} & 0 \\ 0 & 0 & 1 \end{pmatrix}
\end{aligned}
$$

where $c_{jk} = \cos\theta_{jk}, s_{jk} = \sin\theta_{jk}$ with θ_{jk} is the mixing angle, δ is the CP phase, and α_j are Majorana phases.

The probability of neutrino oscillation in vacuum is given by:

$$
\begin{aligned}
|\nu_l(t)\rangle &= \sum_{j=1}^{3} e^{-iE_j t} U_{lj}^* |\nu_j\rangle , \qquad l \in \{e,\mu,\tau\}, \quad j \in \{1,2,3\} && (1.2) \\
&= \sum_{j=1}^{3} e^{-iE_j t + ip_j x} U_{lj}^* \sum_{h=1}^{3} U_{jh} |\nu_h\rangle , \qquad h \in \{e,\mu,\tau\} && (1.3) \\
P(\nu_l \to \nu_k) &= |\, \langle \nu_k | \, e^{iE_h t - ip_h x} \sum_{h=1}^{3} |\nu_h\rangle \sum_{j=1}^{3} e^{-iE_j t + ip_j x} U_{lj}^* U_{jh} \,|^2 && (1.4) \\
&= |\sum_{j=1}^{3} e^{-i(E_j - E_h)t + i(p_j - p_h)x} U_{lj}^* U_{jk} \,|^2 && (1.5)
\end{aligned}
$$

where E_h is the value of the vacuum Hamiltonian and p_h is the momentum operator. Expressing the exponent of e in equation 1.5 as:

$$
\begin{aligned}
-(E_j - E_h)t + (p_j - p_h)x &= -(E_j - p_j)x + E_j(x-t) + (E_h - p_h)x - E_h(x-t) \\
&= -\frac{E_j^2 - p_j^2}{E_j + p_j} x + E_j(x-t) + \frac{E_h^2 - p_h^2}{E_h + p_h} x - E_h(x-t) \\
E_x + p_x &\approx 2E \\
-(E_j - E_h)t + (p_j - p_h)x &= -\frac{m_j^2}{2E} + \frac{m_h^2}{2E} + (x-t)(E_j - E_h) \\
-(E_j - E_h)t + (p_j - p_h)x &= \frac{\Delta m_{h,j}^2}{2E} + (x-t)\Delta E_{j,h}
\end{aligned}
$$

where E is the mean energy. Hence:

$$P(\nu_l \rightarrow \nu_k) = \mid \sum_{j=1}^{3} e^{i(\frac{\Delta m^2_{h,j}}{2E} + (x-t)\Delta E_{j,h})} U^*_{lj} U_{jk} \mid^2 \tag{1.6}$$

Typically detected neutrinos are ultra-relativistic allowing t = x and thus reducing the equation above to the standard expression for the neutrino oscillation probability[29].

1.3 Double Beta Decay Theory

Double beta decay, $2\beta 2\nu$ is the simultaneous occurrence of two beta decays, first predicted by M. Goeppert-Mayer in 1935[30]. Double beta decay is identifiable in isotopes where a single beta decay is energetically forbidden. For $^{150}_{60}$Nd the beta decay to $^{150}_{61}$Pm is energetically forbidden, as Pm is 61keV more massive, whereas double beta decay to $^{150}_{62}$Sm is allowed with $Q_{\beta\beta}$ = 3.37138(20)MeV [31]. The A=150 mass parabolas are shown in figure 1.1.

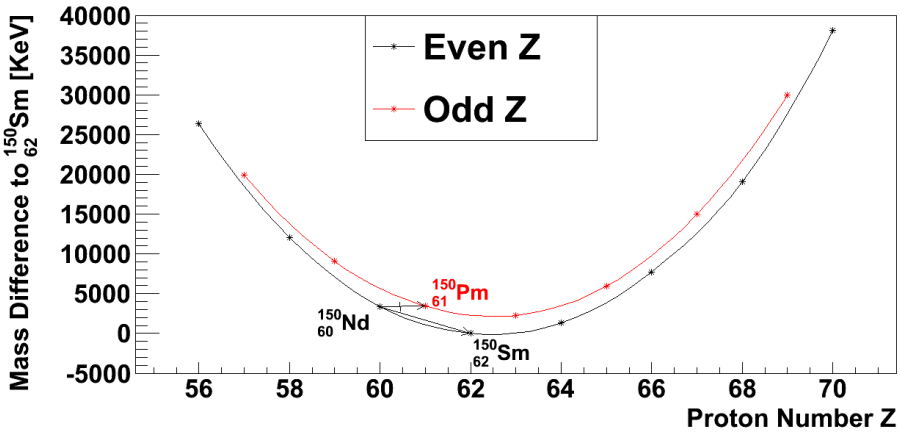

Figure 1.1: Mass plotted against proton number (Z) for A=150 nuclei. The disallowed beta decay and allowed double beta decays of ^{150}Nd are shown.

As postulated by W. Furry in 1939[32] if neutrinos are massive Majorana particles a modified form of double beta decay can occur where no neutrinos are

emitted. In neutrinoless double beta decay, $2\beta0\nu$, the neutrino is a virtual particle that is emitted by one nucleon and absorbed by the other. This can only occur if the neutrino is a Majorana particle, and thus there is no particle/anti-particle distinction. Furthermore for the neutrino to have left-handed helicity at one vertex and right-handed at the other to couple to the standard model W bosons, the helicity must flip, this introduces a mass dependence to the cross section. The half-life ($T^{0\nu}_{1/2}$) for this decay is typically expressed as[33]:

$$(T^{0\nu}_{1/2})^{-1} = G^{0\nu}|M^{0\nu}|^2 \left(\frac{\langle m_\nu \rangle}{m_e}\right)^2 \tag{1.7}$$

$$\langle m_\nu \rangle = \left| \sum_{j=1}^{3} U^2_{ej} m_j \right| \tag{1.8}$$

Where $G^{0\nu}$ is the decay phase space factor, $M^{0\nu}$ is the nuclear matrix element, m_e the electron mass and m_j the mass of the neutrino eigenstate.

The experimental signal for neutrinoless double beta decay is a signal at the end point of the double beta spectrum. The two electrons in a neutrinoless double beta decay have the full $Q_{\beta\beta}$ energy, whereas in a double beta decay the energy is also shared with two neutrinos. The ideal experiment, with only $2\beta2\nu$ as a background, is shown in figure 1.2.

The experimental sensitivity is typically expressed in terms of the half-life and the neutrino Majorana mass. This sensitivity can be expressed by noting that the number of $2\beta0\nu$ events, N, given an isotope mass M, live time t and atomic mass unit u is:

$$N = \frac{Mt \ln 2}{150\text{u}T^{0\nu}_{1/2}} \tag{1.9}$$

Therefore in the background limited regime $N \propto \sqrt{b}$, where b is the background count, and thus

$$T^{0\nu}_{1/2} \propto \frac{Mt \ln 2}{\sqrt{b}150\text{u}} \tag{1.10}$$

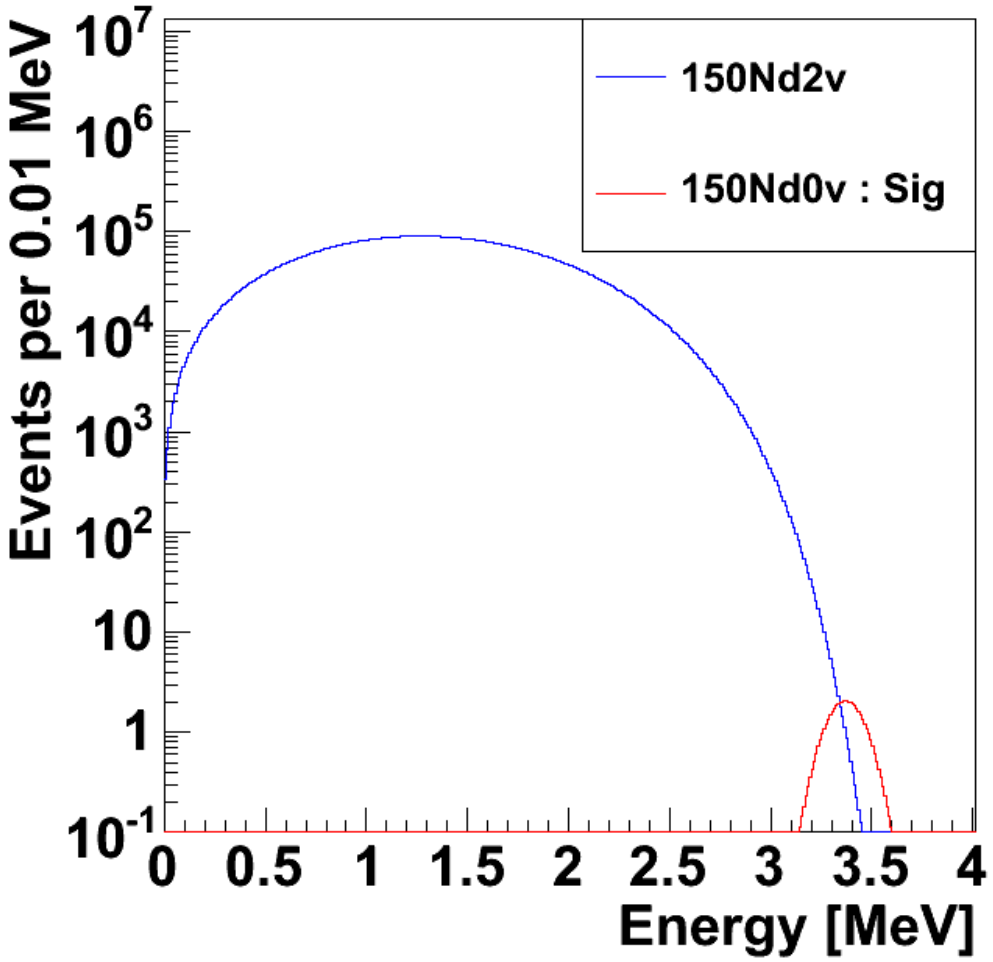

Figure 1.2: Ideal signal for neutrinoless double beta decay of ^{150}Nd.

Assuming that background count b goes as, $b = Mt\Delta E$ where ΔE is the energy resolution, gives the standard sensitivity dependence

$$T^{0\nu}_{1/2} \propto \frac{Mt \ln 2}{\sqrt{Mt\Delta E}150\text{u}} \tag{1.11}$$

$$T^{0\nu}_{1/2} \propto \sqrt{\frac{Mt}{\Delta E}} \tag{1.12}$$

$$m_{\beta\beta} \propto \sqrt[4]{\frac{\Delta E}{Mt}} \tag{1.13}$$

Framework	$M^{0\nu}$ values
Tü	3.45
IBM	2.321 - 2.888
GCM	1.71
PHFB	1.98 - 3.7

Table 1.1: $M^{0\nu}$ values as calculated in different frameworks, summarised from [34]. The Tübingen NME uses the renormalized quasiparticle random phase framework, the IBM NME uses the interacting boson model framework, the GCM NME uses the generating coordinate method and the PHFB NME uses projected-Hartree-Fock-Bogoliubov wavefunctions.

1.3.1 Theoretical Predictions

The values in equation 1.7 have theoretical predicted values. The phase space factor $G^{0\nu}$ is calculable and has much less uncertainty than the matrix element; a value for ^{150}Nd of $G^{0\nu} = 19.2 \times 10^{-14} yr^{-1}$[34] will be used in this thesis. The matrix element $M^{0\nu}$ has much greater uncertainty due to the difficulties in modelling complex nuclei well A summary of matrix element values calculated using different frameworks is shown in table 1.1. In this thesis, $M^{0\nu} = 2.321$, which is a conservative choice using the SNO+ preferred IBM framework. The IBM framework is preferred as it includes a calculation of nuclear deformations expected in ^{150}Nd.

The final unknown factor in equation 1.7 is the Majorana neutrino mass itself. This is typically expressed against the lightest neutrino mass m_{min}, the sum of the neutrino masses M and the effective beta decay mass $\langle m_\beta \rangle$, as shown in figure 1.3 from [24].

The allowed inverted and normal hierarchy regions shown in figure 1.3 are constrained by neutrino oscillation results. Further constraints from solar, cosmological, double beta and beta decay experiments rule out the phase space not shown in the plots. Finally for a Majorana mass of 320meV and using the values stated above, the expected ^{150}Nd $T^{0\nu}_{1/2} = 2.5 \times 10^{24} yr$.

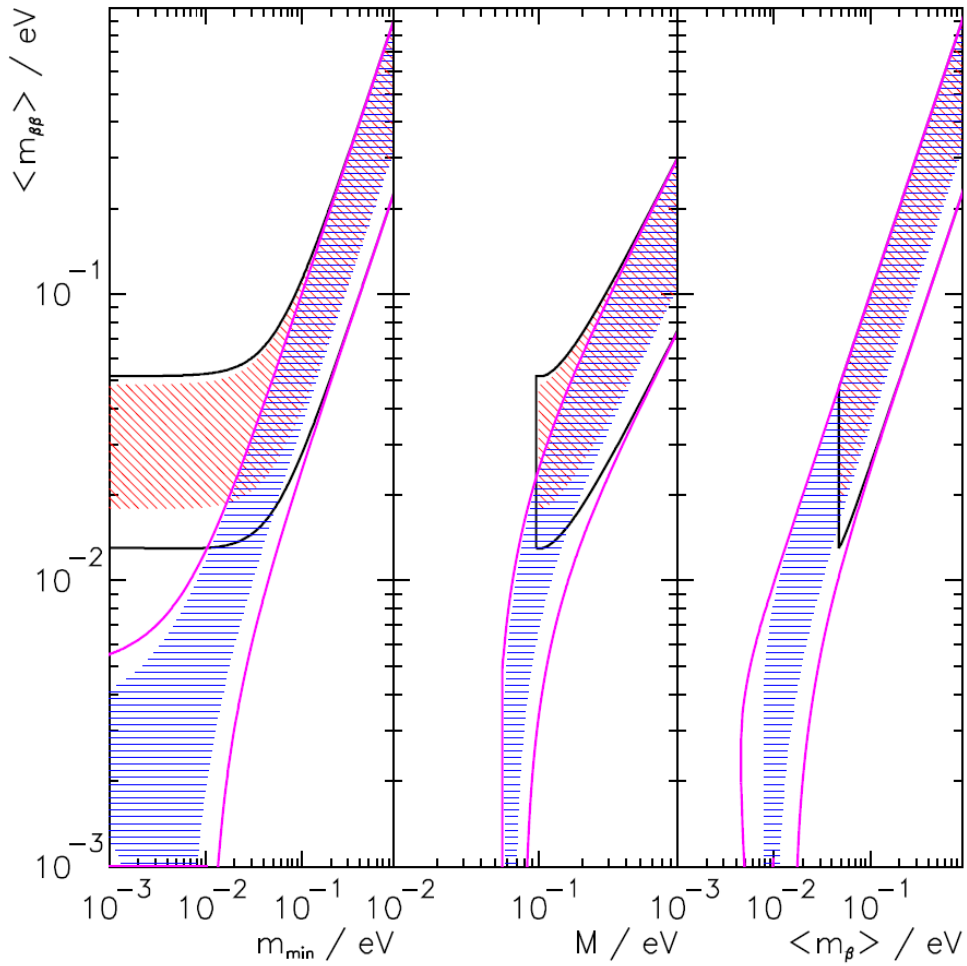

Figure 1.3: Allowed neutrino mass from [24]. Left shows $m_{\beta\beta}$ versus the absolute mass of the lightest neutrino. Middle shows $m_{\beta\beta}$ versus the sum of the neutrino masses M. Right shows $m_{\beta\beta}$ versus the effective beta decay neutrino mass. Red shows the allowed inverted hierarchy masses, blue normal hierarchy with the degenerate region being the overlap for $m_{\beta beta} > 0.1$meV. The allowed regions are determined by the current oscillation measurements, cosmological limits and previous $2\beta0\nu$ measurements.

1.4 Double Beta Decay Experiments

From equation 1.13 it is clear that double beta decay experiments will ideally minimise the energy resolution and maximise the mass of isotope. However, in reality cost and complexity constraints generally separate experiments into those with very good energy resolution and those with very large masses. Thereafter the choice is over the double beta decay isotope, with the ideal isotope having

Isotope	$G^{0\nu}\|M^{0\nu}\|^2$ $[10^{-14}a^{-1}]$	$Q_{\beta\beta}$ [MeV]	Natural Abundance [%]
^{48}Ca	35.7†	4.274	0.187
^{76}Ge	13.4	2.039	7.8
^{82}Se	39.1	2.996	9.2
^{96}Zr	36.0	3.348	2.8
^{100}Mo	60.7	3.035	9.6
^{116}Cd	35.8	2.809	7.6
^{130}Te	46.5	2.530	34.5
^{136}Xe	48.4	2.462	8.9
^{150}Nd	103.4	3.372[31]	5.6

Table 1.2: Matrix element values used are the conservative IBM values except † which is GCM, data from [34].

a large $Q_{\beta\beta}$, above natural radioactive backgrounds, large natural abundance, large predicted $G^{0\nu}|M^{0\nu}|^2$ value, and a large $T^{2\nu}_{1/2}/T^{0\nu}_{1/2}$ ratio. A few of the double beta decay isotopes are shown in table 1.2; these are the isotopes used in current experiments or proposed for experiments in development.

As is clear from table 1.2 ^{150}Nd has the largest $G^{0\nu}|M^{0\nu}|^2$, ^{48}Ca has the largest $Q_{\beta\beta}$ and ^{130}Te has the largest abundance. Of the three the ideal isotope choice, excluding financial constraints and the $T^{2\nu}_{1/2}/T^{0\nu}_{1/2}$ ratio, is ^{150}Nd, especially if enriched. This is because ^{48}Ca has a very small natural abundance, and ^{130}Te has a smaller $Q_{\beta\beta}$ value which is in the uranium chain natural radioactivity domain.

The current best limit on neutrinoless double beta decay is set by the International Germanium EXperiment (IGEX). The IGEX experiment had a fiducial mass of 8.4kg of 86% enriched germanium, or 7.2kg of ^{76}Ge arranged in six cryostat detectors located in the Carnfranc tunnel underground laboratory in Spain. The experiment took data between 1991-1993 and 1994-2000 setting a limit $T^{0\nu}_{1/2} > 1.57 \times 10^{25} yr$ at 90% CL[35]. Using the factor in table 1.2, this corresponds to a limit $m_{\beta\beta} < 352$meV at 90% CL.

The IGEX result was challenged by the Heidelberg-Moscow group[36, 37], who have set a similar limit of $T^{0\nu}_{1/2} > 1.1 \times 10^{25} yr$ at 90% CL[38]. The Heidelberg-Moscow group experiment is also an enriched germanium detector containing

10.96kg of ^{76}Ge, arranged in five detectors placed in the Gran Sasso underground laboratory. A subset of the Heidelberg-Moscow collaboration lead by Klapdor-Kleingrothaus have reanalysed the data and claimed a $2\beta0\nu$ signal with half life $T^{0\nu}_{1/2} = 2.21^{+0.44}_{-0.31} \times 10^{25} yr$ at $> 6\sigma$ sensitivity[39].

The Klapdor-Kleingrothaus claim is disputed by the scientific community. The main foci of criticism are the poor understanding of backgrounds, indeed the presence of unexplained backgrounds and the subsequent non-blind analysis used to increase the significance to $> 6\sigma$. The Klapdor-Kleingrothaus claim best value is $m_{\beta\beta} = 320$meV[1]; I will use this value to highlight the signal in all subsequent plots.

The best limit on the ^{150}Nd $2\beta0\nu$ half life is set by the Neutrino Ettore Majorana Observatory III (NEMO3) experiment. The NEMO3 detector is a tracking calorimeter located in the Fréjus Underground Laboratory, contianing 0.03655kg of ^{150}Nd. NEMO3 set a limit $T^{0\nu}_{1/2} \geq 1.8 \times 10^{22} yr$ and measured the $2\beta2\nu$ half-life as $T^{2\nu}_{1/2} = 9.11^{+0.25}_{-0.22} \times 10^{18} yr$[40].

1.4.1 Future experiments

The SNO+ experiment of which this thesis is about, uses the SNO detector filled with liquid scintillator and natural neodymium. Phase 1 of SNO+ using 44kg of natural neodymium is expected to start in 2013. The limit for two years live time is a 90% CL upper limit on the $2\beta0\nu$ half life of $T^{0\nu}_{1/2} > 3.6 \times 10^{24} yr$. This corresponds to a mass limit $m_{\beta\beta} < 260$meV using the value in table 1.2. Methods to improve this limit are discussed in this thesis.

A number of double beta decay experiments are expected to start taking data within a few years of SNO+ (2013). These experiments are EXO, CUORE, SuperNEMO, GERDA, and KamLAND-Zen.

The Enriched xenon Observatory, EXO, started operating the EXO-200 phase

[1]This uses a different matrix element value than in table 1.2.

in spring 2011. This phase consists of 200kg of $\sim$ 80% enriched liquid xenon in a time projection chamber located in the Waste Isolation Pilot Plant in the US. The experiment has already achieved the first measurement of the ^{136}Xe $2\beta2\nu$ half life, $T^{2\nu}_{1/2} = 2.11 \pm 0.04(stat.) \pm 0.21(sys.) \times 10^{21} yr$[41]. The experiment expects to set a 90% CL upper limit on the $2\beta0\nu$ half life of $T^{0\nu}_{1/2} \geq 6.4 \times 10^{25} yr$ by late 2013[42]. This corresponds to a mass limit $m_{\beta\beta} \leq 90$meV using the value in table 1.2.

The Cryogenic Underground Observatory for Rare Events, CUORE, is an experiment under construction in the Gran Sasso laboratory Italy. The experiment is a bolometric detector containing 200kg of ^{130}Te. CUORE consists of two phases CUORE-0 and CUORE; CUORE-0 is expected to start taking data in 2012 and CUORE in 2014[43]. The sensitivity curves for CUORE-0 and CUORE are shown in figure 1.4, taken from [43]. The CUORE-0 phase expects to set a 90% CL upper limit on the $2\beta0\nu$ half life of $T^{0\nu}_{1/2} \geq 0.41 \times 10^{25} yr$ by early 2014[43]. This corresponds to a mass limit $m_{\beta\beta} \leq 370$meV using the value in table 1.2.

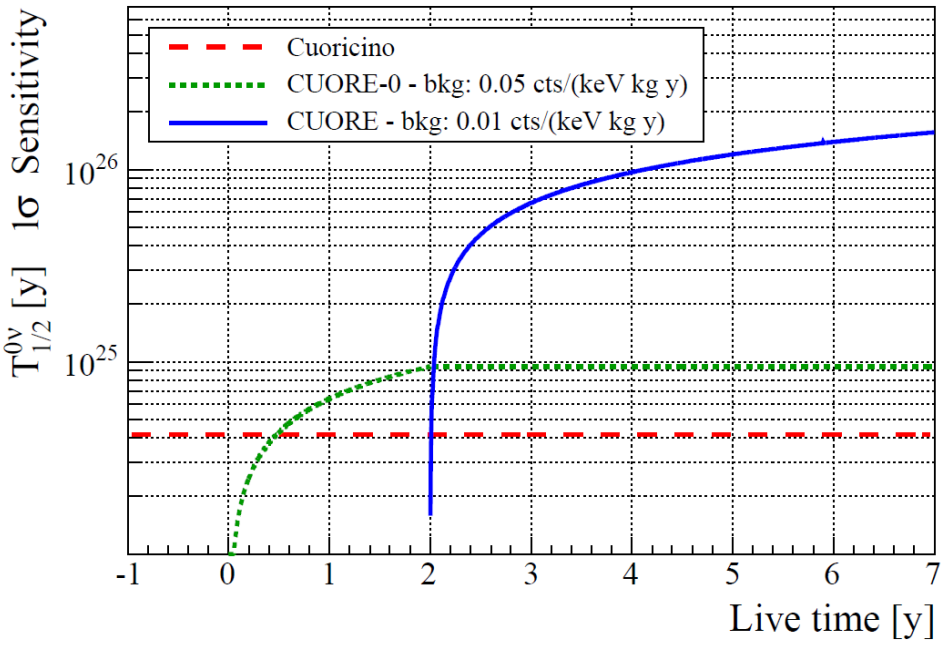

Figure 1.4: CUORE Sensitivity from [43].

The SuperNEMO experiment is a development of the NEMO experiment and is currently under construction. The SuperNEMO experiment will consist of 7kg of ^{82}Se in a demonstration module and 100kg in the full experiment[44]. The collaboration expects the demonstration module to start taking data in 2014 setting a 90% CL upper limit on the $2\beta0\nu$ half life of $T^{0\nu}_{1/2} \geq 6.6 \times 10^{24} yr$ by late 2016[44]. This corresponds to a mass limit $m_{\beta\beta} \leq 320$meV using the value in table 1.2.

The GERmanium Detector Array, GERDA, located in the Gran Sasso underground laboratory is currently taking data. The experiment currently uses 17.9kg of ^{76}Ge, from the IGEX and Heidelberg-Moscow experiments[45]. GERDA expects to set a 90% CL upper limit on the $2\beta0\nu$ half life of $T^{0\nu}_{1/2} \geq 2 \times 10^{25} yr$ by mid 2012[45]. This corresponds to a mass limit $m_{\beta\beta} \leq 310$meV using the value in table 1.2. This experiment will directly test the Klapdor-Kleingrothaus claim using the same isotope within a year of writing this thesis.

Finally the KamLAND-Zen experiment uses the KamLAND detector filled with liquid scintillator and enriched xenon. The phase 1 of the experiment using 400kg of 91% enriched ^{136}Xe will start in 2012[46]. The sensitivity curve of the KamLAND-Zen phase 1 is shown in figure 1.5, taken from [46]. Unfortunately KamLAND-Zen do not show their half life sensitivity, nor which matrix elements they use. However, taking figure 1.5 at face value, KamLAND-Zen expects to set a 90% CL upper mass limit of $m_{\beta\beta} \leq 80$meV in 2014.

In summary the current and near future experiments will easily confirm or reject the Klapdor-Kleingrothaus claim by 2014. Thereafter, there are a number of experiments which will have probed the degenerate hierarchy region and will be capable of setting limits less than 100meV.

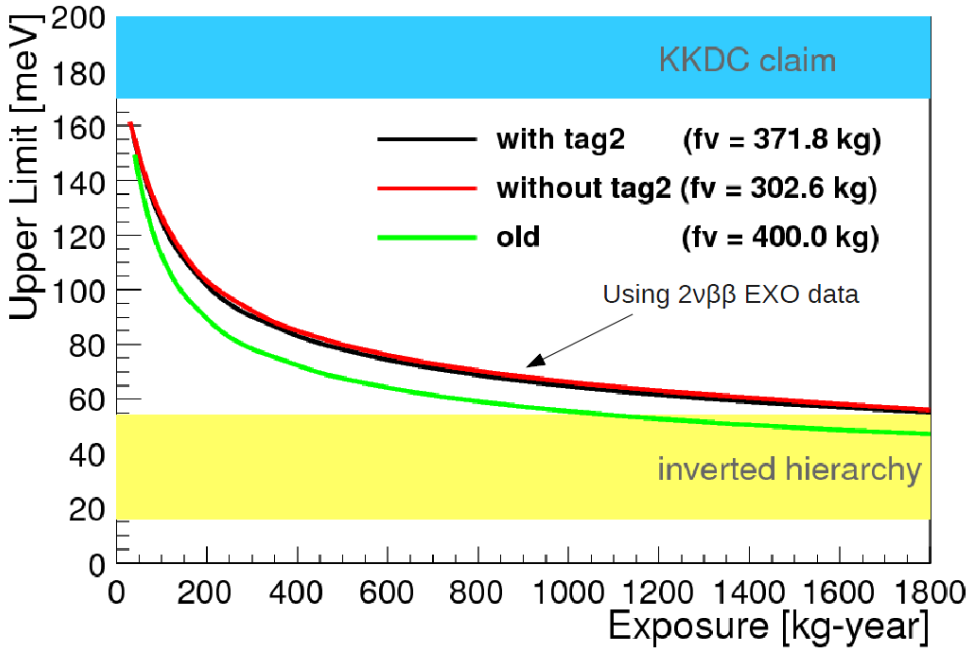

Figure 1.5: KamLAND-Zen sensitivity from [46], under differing background removal tagging schemes.

Chapter 2

SNO+

2.1 The Sudbury Neutrino Observatory

The Sudbury Neutrino Observatory (SNO) was built between 1990 and 1999 in a bespoke cavern 2km under the Sudbury basin in Ontario, Canada. The SNO experiment then took data between 1999 and 2006, before passing the detector over to the SNO+ experiment. Upgrade work required for SNO+ started in 2011 and is expected to finish in 2012 allowing the detector to be turned back on in late 2012 or 2013.

The SNO+ detector, a schematic of which is shown in figure 2.1, is a graded-shield type detector; the centre of the detector inside the Acrylic Vessel (AV) has the least background, with rates increasing as the distance outwards increases. Furthermore, 6000 mwe (meters of water equivalent) overburden decreases the cosmic background rate in the detector.

The SNO+ detector is located in a cavern around 22m wide and 34m high. The cavern walls are lined with concrete and 8mm of Urylon to decrease the radon ingress into the detector[47]. The cavern will be filled with ultra-pure water to the deck level to shield the inner detector. The 17.8m diameter PMT SUPport Structure, PSUP, which holds the 9,529 R1408 Hamamatsu PMTs that provide

the observable data for the SNO+ experiment, is itself supported by 10 synthetic ropes from the deck. Within the PSUP is the 12m inner diameter Acrylic Vessel which will contain the active scintillator material. The AV is formed from 122 ultraviolet ($>$ 300nm) transmitting panels, each 56mm thick, glued together to form a sphere maximising the volume to surface ratio. The AV was supported during the SNO operation by 10, hold-up, rope loops from the deck. The hold-up ropes will be amalgamated with a hold-down rope net for SNO+ operation. The hold-up ropes will be made from 19.5mm thick Tensylon, and the hold-down 38.1mm thick Tensylon. A 1.5m inner diameter, 6.8m high chimney made of ultraviolet absorbing acrylic allows access to the inner AV from the deck to introduce calibration sources and fill and recirculate the AV contents.

The upgrades to the SNO detector required for SNO+ consist of relining the cavity floor, adding the hold-down rope net, sanding the inner surface of the AV, adding calibration fibres, replacing incompatible materials and remapping PMTs. During SNO operation the cavity floor lining split, requiring the relining, which has now been completed. The hold-down rope net is required as the chosen scintillator Linear Alkyl Benzene (LAB) is less dense than the surrounding water. The inner AV surface is contaminated with decay daughters of ^{222}Rn, which are implanted into the surface by recoil following alpha decay. This background would be significant and will be removed by sanding the surface before the SNO+ experiment starts. The calibration fibres allow photons to be injected into the SNO+ detector from set positions on the PSUP. The choice of fibres over embedded LEDs in the detector follows experience from SNO, as the embedded LEDs became waterlogged and failed. LAB is the chosen scintillator due to its compatibility with the AV. However it is incompatible with other plastics including the pipes in the AV, requiring replacement pipes. Finally PMTs and DAQ channels have failed during SNO operation; some of the PMTs can be fixed and replaced, and working DAQ channels remapped to working PMTs.

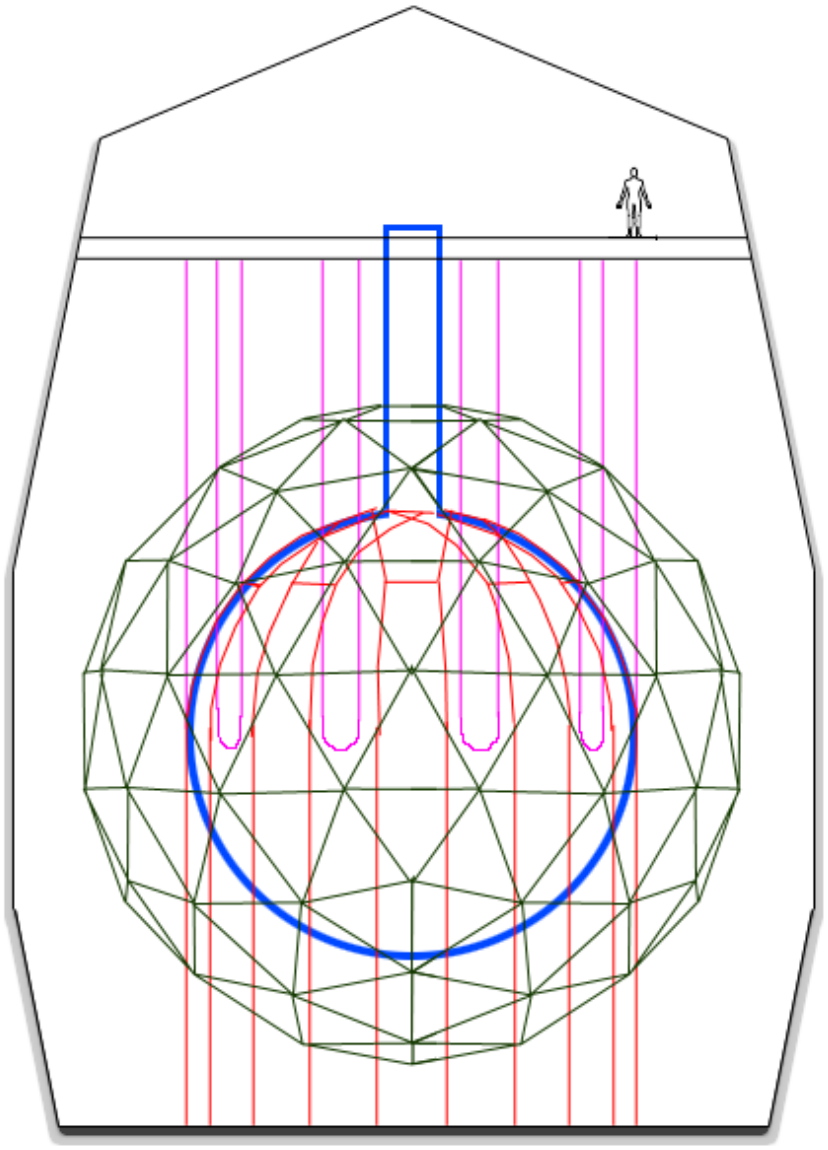

Figure 2.1: Stylised schematic of the SNO+ detector, roughly to scale. The Geodesic PSUP is shown in dark green, only the stainless steel struts are shown with PMTs removed for visibility. The hold-up and down ropes are shown in pink and red respectively. The AV is shown in bold blue. The thickness of all lines does not represent anything. The cavity, deck (with person) are shown in black.

2.1.1 Coordinate system

The global SNO+ coordinate system is a right-handed Cartesian system centred on the centre of the PSUP (detector centre). The z axis points from the detector centre directly upwards. The x axis points from the detector centre towards detector north, identified as the side of the AV where the pipes are located. As the coordinate system is always relative to the PSUP in SNO+, the AV must be positioned in this system. Work to understand the position of the AV after filling is ongoing at the moment.

2.1.2 DAQ overview

The observable data in SNO+ consists of PMT charge and timing information given a true or noise PMT hit. This data consists of 3 charge values: high gain short integration (QHS), high gain long integration (QHL) and low gain long integration (QLL) combined with one time value (TAC).

An analogue pulse from a PMT travels 35m along a coaxial cable to a PMT Interface Card (PMTIC). This card handles 32 channels, with each channel potentially connected to a single PMT. Each PMTIC is connected to a Front End Card (FEC), which calculates the QHS, QHL, QLL and TAC values. If the hit passes the channel discriminator threshold, a signal is sent to the master trigger. The master trigger then conducts an analogue sum of hits within 100, which if above threshold will trigger an eventns [1].

2.1.3 Calibration

The SNO experiment was calibrated with radioactive and laser sources deployed into the inner AV volume suspended and controlled via an umbilical and positioned via calibration side ropes. These calibration side ropes moved the source in x

[1] Other trigger configurations are available.

and y with z movement controlled by lowering the umbilical. This system will be continued in SNO+ with the calibration ropes being replaced with 0.5mm Tensylon[48] and the umbilical rebuilt out of Tygothane. A schematic of the calibration source system is shown in figure 2.2.

The internal sources will be independently positioned (without the use of the PMTs) by placing a flashing LED above the source on the umbilical. The photons from this LED will be detected by 6 cameras placed on the PSUP for SNO+. The camera system aims for a resolution less than 10cm when reconstructing the source position. It will also allow visual inspections of the detector during SNO+ running.

Many different sources will be available during the SNO+ experiment, and for this thesis the N16 and laserball sources will be discussed. The N16 source introduces the isotope ^{16}N into an enclosed vessel in the detector. A ^{16}N beta decay also releases gammas with a principle gamma at 6.13MeV. The gammas escape the enclosed source whereas the beta electron excites scintillator within the source. This scintillator is optically coupled to a small PMT which then sends a signal back up the umbilical that can be triggered upon[49]. The 6.13MeV and other gammas can be used to calibrate the position and energy response of the detector.

The Laserball is a light diffusing sphere coupled to a nitrogen/dye laser that produces an approximately isotropic source at set wavelengths[50]. The Laserball calibrates the PMT response and PMT timing Calibration Analysis (PCA).

Further to the addition of cameras, an Embedded LED Light Injection Entity (ELLIE) will also be added for SNO+. The ELLIE system consists of the Timing TELLIE, the Scattering Monitoring SMELLIE and the Absorption Monitoring AMELLIE subsystems.

The TELLIE system has 91 injection points allowing coverage of every PMT that points inwards (9,438 PMTs). This allows the PCA calibration to take place

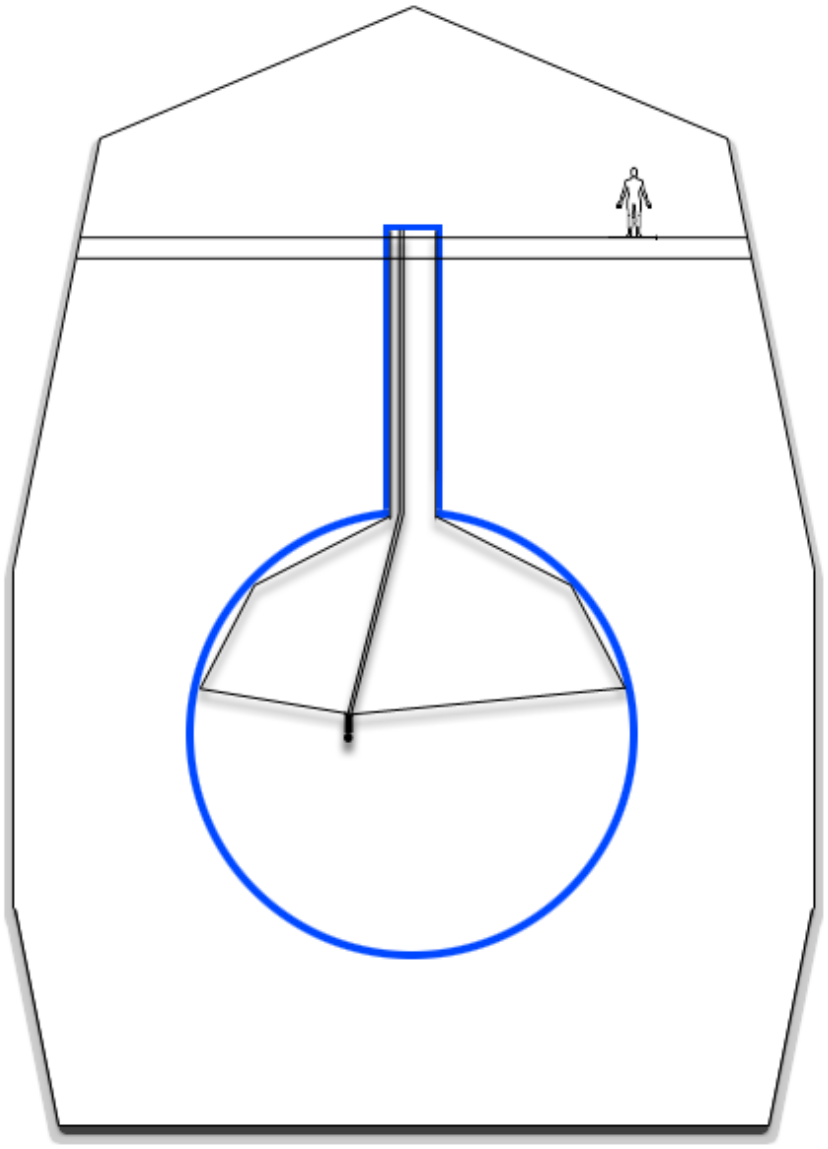

Figure 2.2: Stylised schematic of the SNO+ calibration source system, roughly to scale. Note the calibration ropes follow the curvature of the AV. Movement in and out of the page is achieved in an equivalent manner.

without introducing a source into the inner AV, reducing the possibility of introducing radioactive contaminants into the scintillator. The PCA measures the PMT timing offset and walk per channel (PMT).

The SMELLIE system has 4 injection points with each injection point having three differently orientated fibres. This allows the angular and wavelength dependent scattering of the scintillator to be measured *in situ*. The wavelength dependent measurement is achieved by switching the wavelength injected into the fibre at the deck, by switching the laser.

The AMELLIE system has 4 injection points with each injection point having two differently orientated fibres. This allows the wavelength dependent absorption of the scintillator to be monitored *in situ*. The absorption of the scintillator is a good indicator of scintillator optical degradation, which may occur if it is contaminated.

2.2 Scintillator

The SNO+ experiment will use Linear Alkyl Benzene (LAB) doped with 2g/L 2,5-diphenyloxazole (PPO) fluor. PPO is added as a fluor to shift the emission wavelength spectrum towards lower LAB absorption, by increasing the emission wavelength. With 2g/L PPO added 70% of the LAB excitation is non-radiatively transferred to PPO, and emitted in the lower LAB absorption regime[51]. Thus increasing the fraction of photons that traverse the scintillator without absorption.

The LAB + 2g/L PPO mixture has a light yield of 1×10^4 photons per MeV [52][2]. The emission spectrum for LAB + 2g/L PPO peaks at 365nm, with the LAB absorption sharply decreasing above 300nm [53].

The LAB quenching follows Birks' law with a Birks' constant of 77.4 μm/MeV[54]. In this thesis an alpha quenching factor of 10 will be used, which is the measured

[2]An easy to remember value is 11,111.

value at 6MeV.

2.3 Monte Carlo

The SNO+ experiment will use the Reactor Analysis Tools (RAT) Monte Carlo. The RAT Monte Carlo was originally developed for the Braidwood Collaboration utilising software developed for a generic KamLAND like detector, called Generic Liquid Scintillator Anit-Neutrino Detector, LAND, (GL). It was branched and developed into the specialist SNO+ version, starting in 2006/2007.

The SNO experiment used the SNO Monte carlo ANalysis (SNOMAN) Monte Carlo. This was developed specifically for SNO over the course of the SNO experiment. SNOMAN has been shown to reproduce the SNO calibration data, and hence comparisons between RAT and SNOMAN will be made in this thesis.

RAT was chosen over the well-developed and bespoke SNOMAN Monte Carlo as SNOMAN became outdated during the 2000s. In particular SNOMAN is written in FORTRAN, whereas the particle physics community has moved to c++. Indeed a c++ extension to SNOMAN was required to utilise the latest ROOT versions. RAT however, is written in c++ and utilises the Geant4 and ROOT libraries which are being continually upgraded by CERN. These libraries are predominantly used to simulate physical processes and manage files respectively.

In this thesis I will refer to different versions of the RAT Monte Carlo. The RAT-Initial version refers to RAT before the updates outlined in chapters 3 and 4. The RAT-SNOMAN version refers to RAT running code and using parameters designed to mimic SNOMAN. References to RAT should be read as r615M, a locally modified copy of the latest RAT version at the time of writing.

2.4 Viewer (SNOGoggles)

The SNO+ event viewer allows the event data from the detector to be visualised in real time[3], in a human-friendly format. I lead the development of the viewer with K Clark and O Walsalski during 2011. An example screen shot from the viewer is shown in figure 2.3, showing an electron event.

The SNO+ event viewer includes 3d, icosahedral, elliptical, and Lambert Azimuthal projections of the PSUP with colour-coded hits. This coding is based on the hit time or optionally hit charge of the PMT. The hit times are also displayed in a histogram format, along with charge. Finally a crate projection is also included to allow DAQ monitoring.

2.5 SNO+ Analytic Monte Carlo (SNO+py)

SNO+py or SNO+ simulation in python is a standalone Monte Carlo simulation of the SNO+ experiment developed by myself. This software omits the detail present in RAT to produce plots and limits quickly under differing assumptions. The equivalent plots and limit setting in RAT would take at least an order of magnitude longer to achieve.

This software uses analytic expressions for the energy spectra (histogram of events binned in energy). For $2\beta2\nu$ decays the Primakov-Rosen approximation for the summed spectrum has the analytic form[55]:

$$\frac{dN}{dK} \sim K(Q-K)^5 \left(1 + 2K + \frac{4K^2}{3} + \frac{K^3}{3} + \frac{K^4}{30}\right), \tag{2.1}$$

where the summed kinetic electron energy K and end point Q are in units of electron mass, $K = (E_1 + E_2)/m_e$. For beta decay the summed spectrum has the

[3]Subject to cuts given the 1kHz event rate.

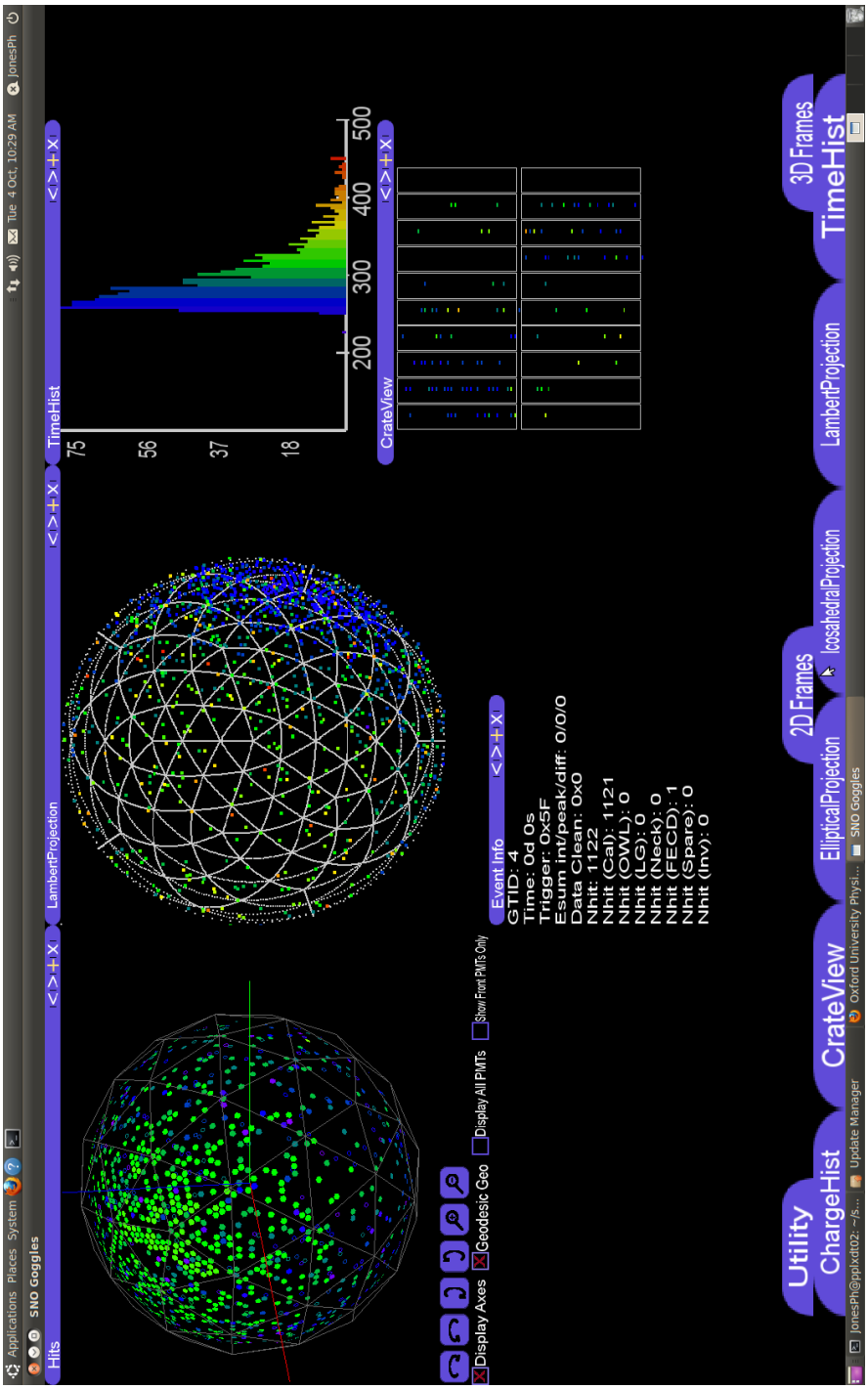

Figure 2.3: Screen shot of the SNO+ viewer, SNOGoggles. The 3d and Lambert Azimuthal PSUP projections are shown alongside the time histogram, crate projection and basic event info.

analytic form[56]:

$$\frac{dN}{dE} \propto \sqrt{E^2 + 2E \cdot m_e}(Q - E)^2(E + m_e), \tag{2.2}$$

where the electron kinetic energy E and neutrino mass m_e are in units of MeV. For alpha decay and $2\beta0\nu$ decay the spectrum is a delta function, alpha decays have an assumed quenching factor of 10[54]. For gamma decay the spectrum is also a delta function, this assumes that the gamma does not escape the scintillator after scattering etc. This assumption breaks down for events near the AV edge, however the details required to simulate this effect are neglected as this region is not used in the analysis.

The analytic spectra can then be convoluted with a Gaussian energy resolution, as assumed for SNO+. As the energy is reconstructed using the number of hits (Nhit) in the event, the primary energy resolution is Gaussian with $\sigma = \sqrt{\text{Nhit}}$. A Nhit per MeV value of 400 is assumed for 0.1% Nd loading. Alternatively the resolution as reconstructed by the energyLookup algorithm, see section 6.7.1, can be used. Finally energy-dependent event rejection can be included for both single and pileup events (with differing factors).

The SNO+py software thus allows the expected spectra to be plotted under differing energy resolution, Nd loading, rejection and live time[4] assumptions. It also allows the half-life/mass limits to be calculated under these differing assumptions.

[4]Live time is the time when the DAQ is active i.e. the detector is running.

Chapter 3

Modelling the PMT, Concentrator and PMT Support Geometry

The PMT geometry used in RAT is shown in comparison to the SNOMAN and the initial RAT geometry with justification given for the modelling. Measurements of the geometric shapes are presented.

The SNO+ experiment uses 9,438 inward-facing R1408 Hamamatsu photomultiplier tubes (PMTs) to detect photons from within the Acrylic Vessel, AV, and a further 91 outward facing[1] R1408 PMTs to detect photons in the cavity region. The inward-facing PMTs are combined with a concentrator[2] to increase the effective coverage of the detector. The concentrator-PMT combinations are placed into hexagon support cells[3], which are tiled to produce panels. The panels are aligned to point at the centre of the PSUP. The outward facing PMTs are left bare and point directly away from the centre of the PSUP. The outward facing PMTs are supported by a transparent acrylic support and positioned on the outside of the

[1] Or Outward Looking i.e. OWL.
[2] Also called a reflector.
[3] Also called a bucket.

PSUP.

The PMTs must be well understood and modelled for the Monte Carlo to be correct and match data. This requires the Monte Carlo to accurately track a photon to and within the PMT geometry. It also requires the Monte Carlo to accurately simulate backgrounds present in the PMT, concentrator and PSUP.

The geometry used in RAT-Initial had not been checked and verified as correct but is derived from the modelling used in the SNO Monte Carlo SNOMAN. However, SNOMAN never managed to correctly simulate observed PMT response changes via a concentrator ageing model, instead the changes were modelled in the PMT response. As the concentrators are known to be ageing, RAT will simulate the changing response via a concentrator ageing model. The SNOMAN difficulty in simulating the ageing in SNOMAN may have been due to an incorrect geometric model, motivating the detailed geometric checks, measurement and RAT modelling outlined in this chapter.

3.1 PMT Geometry

The eight-inch hemispherical Hamamatsu R1408 PMT used in SNO+ consists of a deformed oblate spheroid glass bulb with a further glass cylinder radially extruding from the bulb on a minor axis. The minor axis and the axis of the cylinder form the primary PMT axis, and the plane defined by the maximal radii defines the PMT equator. A cross section of the R1408 PMT is shown in figure 3.1. The base of the neck is called the bottom of the PMT and the top of the PMT is the front face. The inside surface of the glass is coated with a photocathode above the equator and with a mirror surface below, with a small region of overlap. The evacuated glass contains a dynode stack, the stack starts at the base of the neck and finishes below the equator.

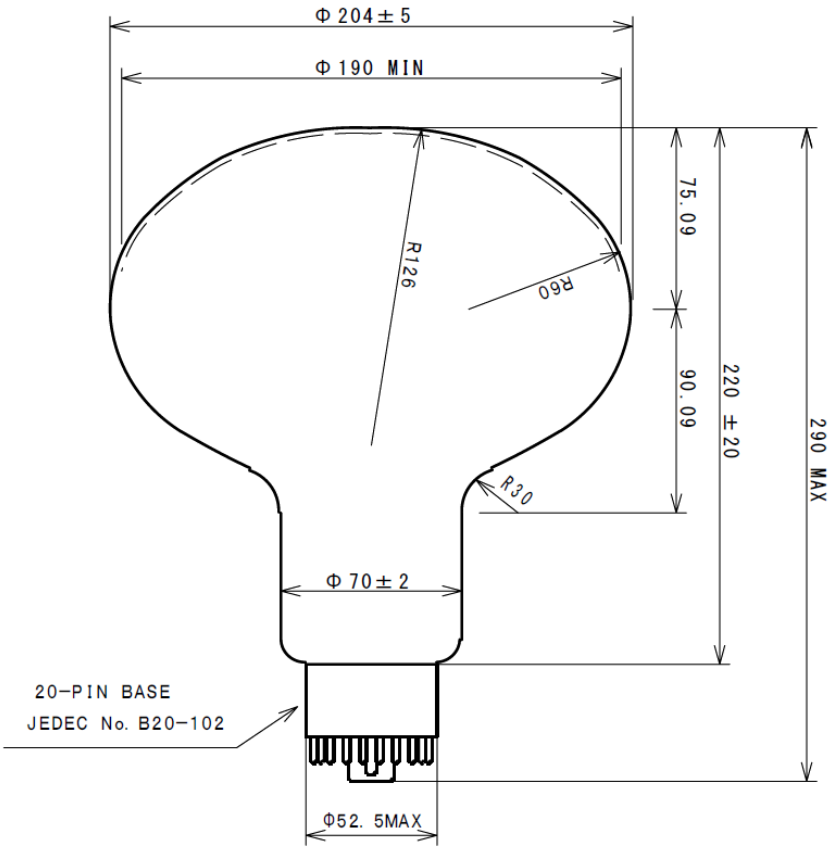

Figure 3.1: The dimensional outline of the R1408 PMT, courtesy of Hamamatsu [57].

3.1.1 Previous Modelling of the PMT Glass

In the SNO expriment the R1408 PMT was modelled as a combination of a truncated spherical cone and a torus[58]. As the PMT is symmetric about the PMT axis, the geometry can be fully described by a 2d cross section as shown in figure 3.2. The sphere has radius 125.3mm and is centred on the PMT axis 50.9mm below the equator, and the torus has a = b = 59.2mm and d = 42mm. The sphere is then truncated by the equator and where it meets the torus to form a conic section. A sphere equivalently truncated, centred on the PMT axis 50.9mm above the equator forms the lower part of the PMT. This design is based on PMT measurements taken by R J Boardman (figure 7.1)[59].

The SNO modelling of the R1408 geometry does not detail the curvature

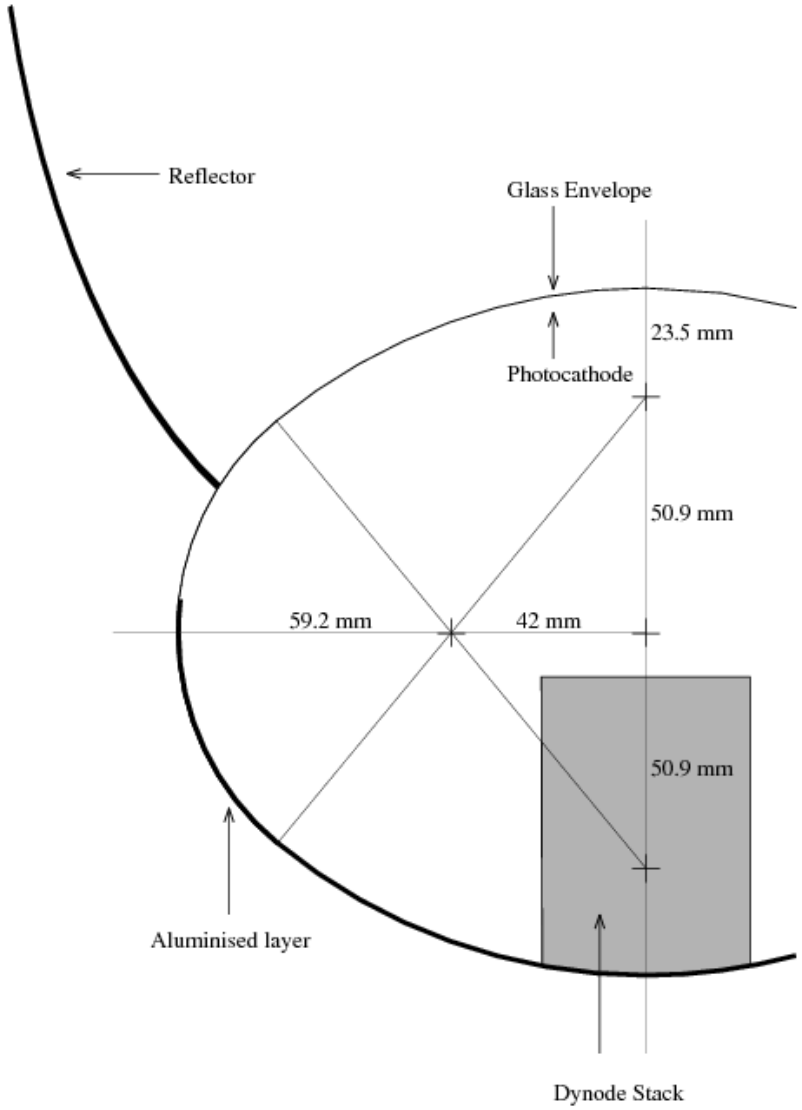

Figure 3.2: The model of the PMT cross section used in SNO, taken from [58].

between the neck and bulb or the lower dynode stack, which are omitted for simplicity[58]. Furthermore it is not clear whether a pre-production version of the PMT or the production version was used to obtain the dimensions.

The modelling used in RAT-Initial is based on the Hamamatsu R5912 PMT, which is an updated version of the R1408. The modelling consists of a stack of torii via a dedicated geometric type (GLG4TorusStack) added to the Generic LAND Geant4 extension. Unfortunately the R5912 PMT has a different shape to the R1408[57], hence the modelling required replacing.

3.1.2 Measurement of the Glass Outline

To ensure that the actual outline of the PMTs in SNO+ matches the specification shown in figure 3.1, two PMTs have been measured by a coordinate measurement machine (CMM), to a 5μm tolerance. The shape of the PMT can be split into three regions, the front face (which is expected to have a curvature of ≈126mm), the side (which is expected to have a curvature of ≈60mm) and the lower PMT. The data taken from the CMM allows fitting of the first two regions but not the lower PMT, as the lower PMT is inaccessible to the CMM. Therefore the lower PMT is assumed to be as specified by Hamamatsu in figure 3.1.

According to the specification the front face should have curvature of 126mm at an origin of (r=0, z=-50.91)mm [4]. The front face should then extend to (80.2, 46.2)mm which is the point of intersection with a circle centred at (42, 0)mm with radius 60mm. The 60mm curvature should then extend to (80.2, -46.2)mm followed by curvature of 126mm at an origin of (0, 50.91)mm till (58.1, -60.9)mm. The neck bulb intersection curvature of 30mm at (65, -90.09)mm then extends to (35, -90.09)mm followed by a constant line at (35, z) till (35, -145)mm.

To confirm the specification, I carried out a fit to the data, using TMinuit2. Excluding the parameters describing the data origin and rotation (about the base) the fit was:

$$r = \sqrt{P_1^2 - (z - P_2)^2} \quad z > P_5 \tag{3.1}$$

$$r = P_3 + \sqrt{P_4^2 - z^2} \quad z[P_5, -P_5) \tag{3.2}$$

$$r = \sqrt{P_1^2 - (z + P_2)^2} \quad z <= -P_5 \tag{3.3}$$

With the parameter definitions shown in figure 3.3.

This gave the following best fit values (combined from 4 of the data sets),

[4]The PMT axis equator intersection define the coordinate origin. The PMT axis then defines the z axis.

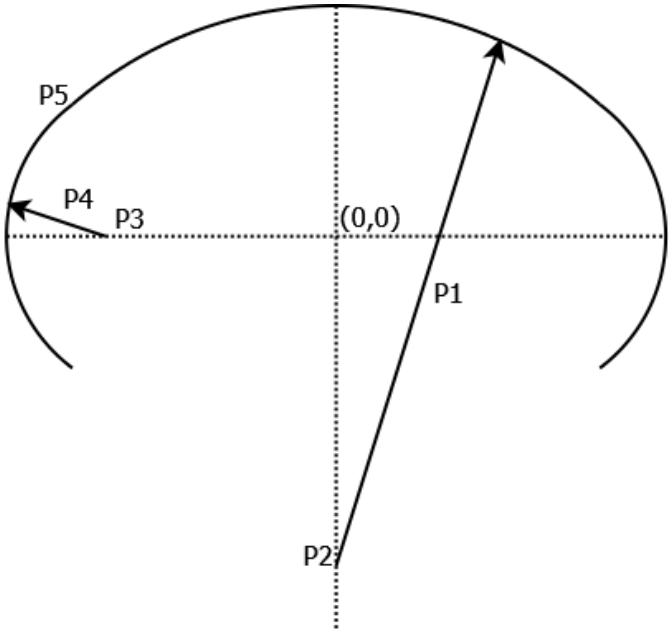

Figure 3.3: Schematic of the top section of the R1408 PMT shown with fit parameters. P_1 Front face curvature radius. Front face curvature position (assumed on axis for symmetry). Side face curvature position (defines PMT equator, thus z=0). Side face curvature radius. Front face to side face transition point, z coordinate.

typical $\chi^2/ndf = 16.7561/38 = 0.440949$:

$$P_1 = 121.6 \pm 1.2\text{mm} \tag{3.4}$$

$$P_2 = -46.2 \pm 0.7\text{mm} \tag{3.5}$$

$$P_3 = 41.4 \pm 0.7\text{mm} \tag{3.6}$$

$$P_4 = 59.5 \pm 0.6\text{mm} \tag{3.7}$$

$$P_5 = 45.8 \pm 0.1\text{mm} \tag{3.8}$$

The front face was also found to have a non constant curvature between $\pm P_5$. However, the constant curvature model gives a good fit to the data, and is therefore used.

ρ_1	z_1	ρ_2	z_2	z origin
[mm]				
0	74.9	74.5	49.4	-46.6
74.5	49.4	74.5	-49.4	0
74.5	-49.4	100.5	0	0
100.5	0	54.5	-62	46.6
54.5	-62	35	-90.09	-90.09
35	-90.09	35	145.1	-145.1

Table 3.1: The arcs chosen to define the shape of the R1408 PMT.

3.1.3 SNO+ Modelling of the Glass

Following the example of the previous R5912 PMT in RAT I will model the R1408 PMT as a torus stack using the GLG4Torus stack code. This has the advantage of being a specific single piece of geometry whereas the other choices are an union of multiple geometry types, e.g. sphere, cylinder. A single piece of geometry is prefered for code execution performance reasons.

The GLG4Torus stack code defines the tori in 2d by a series of circular arcs that are revolved two pi about an axis. This axis then forms the PMT axis, i.e. the axis of symmetry. The arcs are defined by the start coordinates, the end coordinates and the position of the centre of the arc. Only the coordinate along the axis symmetry is required to define the centre of the arc given the start and end coordinates.

I have chosen the best fit values and the specification (for the lower PMT region) to define the PMT shape. This leads to the arcs given in table 3.1 as input to the GLG4TorusStack code. An overlay of this shape to a measured data set is shown in figure 3.4.

The glass is 3mm thick throughout[58].

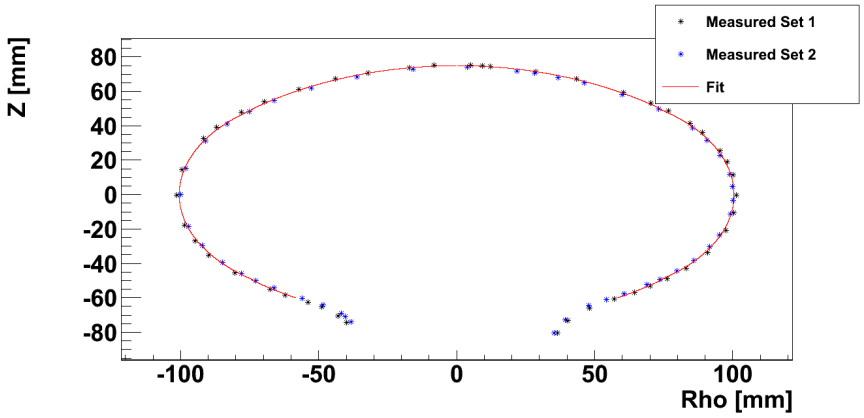

Figure 3.4: Fitted PMT shape (red) against two measurement sets. The measured coordinates have been translated and rotated by values determined in the fit.

3.1.4 Modelling of the inner PMT

The evacuated glass volume of the R1408 contains the dynode stack. The inner surface of the glass is coated with photocathode above the equator, aluminium below and a small region of overlap on the equator. The region of overlap extends from -25.0mm to 5.0mm, and is glass then aluminium then photocathode from the outside[58]. The dynode stack is cylindrical with radius 27.5mm and starts at the base of the PMT and extends to -5.9mm [58]. The dynode stack is assumed to have no inner structure and to be made of aluminium. I have simulated different stack reflectivities, varying by 50%, with no affect on the PMT response. This indicates that the dynode stack simulation has a small affect on the net PMT response.

The inner part of the R1408 is modelled by three vacuum volumes (inner1,2,3) and one dynode stack volume. The upper vacuum volume, inner1, follows the shape of the glass volume between 5.0mm and the top of the PMT, and has a photocathode surface. The middle vacuum volume, inner2, follows the shape of the glass volume between 5.0mm and -25.0mm, and has a photocathode overlapping aluminium surface. Finally the lower vacuum volume, inner3, follows the shape of the glass volume between -25.0mm and the PMT bottom, has an aluminium

surface and fully encloses the dynode stack volume. The dynode stack volume is modelled as an aluminium cylinder.

3.2 Concentrator Geometry

The concentrator is a truncated Winston cone broken into 18 identical reflective petals. The truncated concentrator forms an enclosed octadecagonal cross sectioned cone with open ends. The petals are supported by a plastic support structure. The profile of the petal and the number of petals fully describes the concentrator shape.

The reflective petals consist of dielectric coated aluminium (DCA) also called omega in SNO. The 0.3mm thick DCA which is coated, by evaporation, firstly by SiO_2 as a chemical barrier, then Al as the primary optical surface, MgF_2 to provide a low refractive index layer and finally a mixture of TiO_2 and Pr_2O_3 to provide a water seal[58].

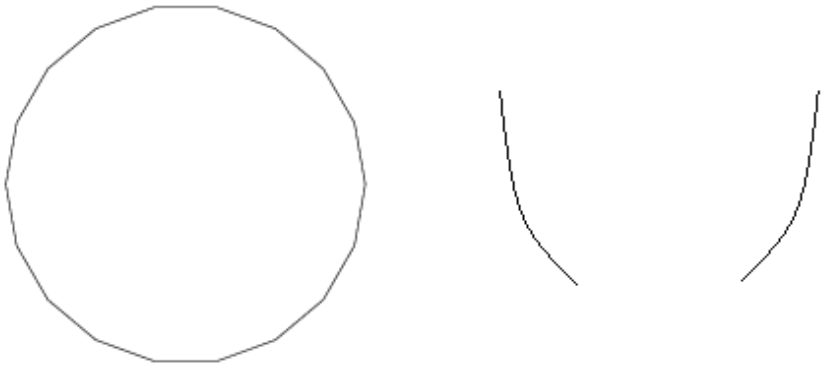

Figure 3.5: Sketch horizontal (left) and vertical (right) cross sections, not to scale.

The correct definition of the profile is important and may have lead to errors in the previous modelling. Throughout I refer to the profile in (r, z) coordinates for the locus along the centre of the petal, with r and z as defined in 3.6. This definition of the profile is the most well defined as it is the distance between any two loci on opposite and thus parallel petals. Occasionally where explicitly stated

I will use a different definition which is predominantly used previously in SNO and is the locus along the edge of the petal.

3.2.1 Previous Modelling of the Concentrator Petals

In the SNO experiment the truncated Winston cone profile was modelled as an ellipse, as the Winston cone has no traceable analytic form[58]. The ellipse profile was parametrised by the minor axis (a), major axis (b), offset in r (d or q) and upper and lower radii as shown in figure 3.6. The parameters were slightly refined for SNOMAN such that a = 52.6mm, b = 168mm, d = 88mm, upper radius = 136.56mm and lower radius = 98.25mm. This elliptical fit was carried out by M D Lay[58] and uses the definition of the profile being the locus along the edge of the petal.

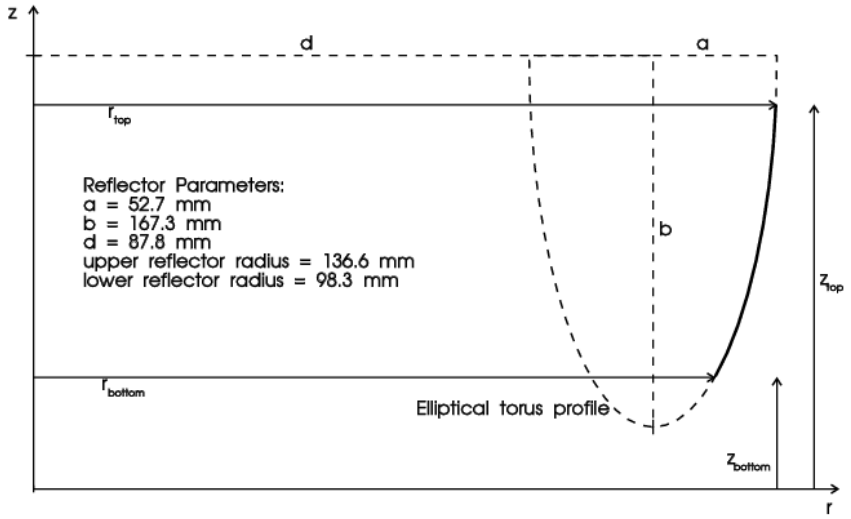

Figure 3.6: The profile of the concentrator used in SNO, taken from [58].

The modelling used in RAT-Initial uses the M D Lay elliptical fit. However the profile was split into 20 equally spaced segments along z, with linear interpolation in between. This allows the Geant4 G4Polyhedra geometry to be used, which in turn allows a single geometric object for the entire concentrator. As M D Lay's fit uses the edge locus definition and the G4Polyhedra implicitly uses the centre

locus definition the previous RAT-Initial modelling of importing the SNOMAN values directly into RAT is incorrect.

3.2.2 Measurement of the Concentrator Profile

Two concentrators each with two measurement sets, i.e. four profiles were measured by a coordinate measurement machine, CMM, to a 5μm tolerance. Each measurement consisted of the distance (height) from the top of the petal and the distance between two petals. As two opposite petals are parallel this gives an absolute measure of the profile. A profile of the support plastic was also taken by removing two opposite petals.

I produced a combined fit by assuming a linear interpolation between the measured points and averaging the sets thereafter. The combined fit and measured data points are shown in figure 3.7.

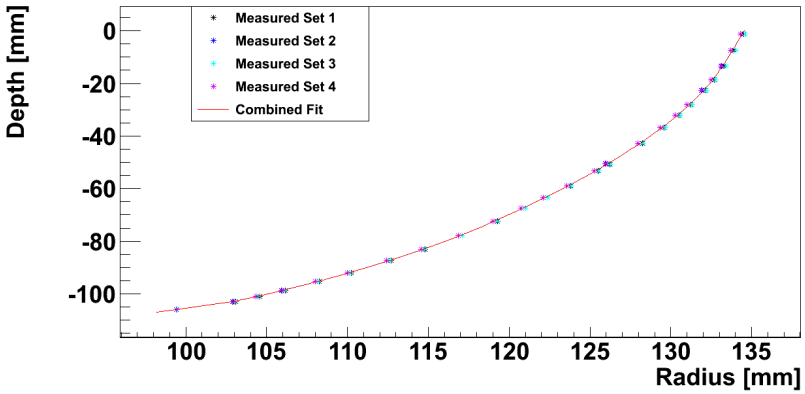

Figure 3.7: Fitted concentrator profile (red) against four measurement sets. The z coordinate is distance from the top of the petal, the r coordinate is from the centre of the concentrator. The error on each measured point is 5μm.

A measured profile for the concentrator before fabrication was carried out by M E Moorhead[60]. The combined fit profile is found to differ from the M E Moorhead (figure 6.15)[60] and M D Lay [58] profiles. These profiles and deviation from the combined fit are shown in figure 3.8. It is clear that all three profiles

differ, and it is likely the profile changed significantly between M E Moorhead's measurement and fabrication. The fitted profile given by M D Lay is also incorrect as it foreshortens the height by 7mm rather than the 2mm expected by Lay[58].

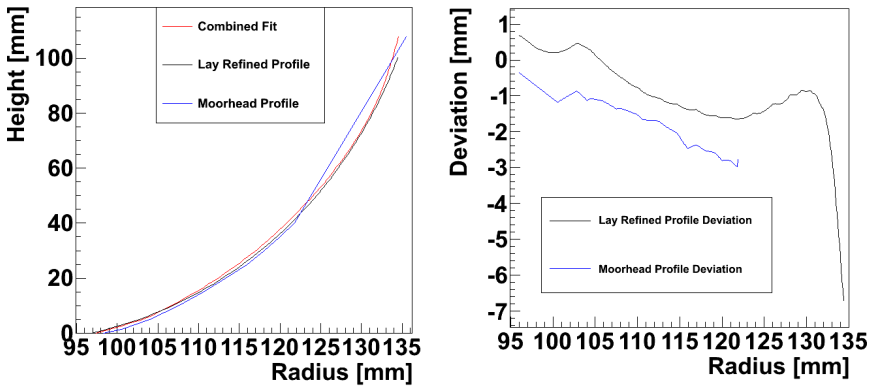

Figure 3.8: The combined fit, M D Lay refined profile and M E Moorhead profile are shown. Alongside the deviation of each profile from the combined fit. The M D Lay refined profile is the SNOMAN fit profile corrected by $cos(\pi/18)$ to convert the profile from an edge locus to a centre locus.

The bottom radius of the concentrator defines the offset of the concentrator from the PMT equator, as the base of the concentrator touches the PMT glass. Unfortunately the early SNOMAN code contained a bug which placed the concentrator too close to the PMT equator; this bug migrated to the previous RAT code. This came about as the lower radius defined in M D Lay's fit was used to find the PMT intersection. This fit radius is larger than the inner radius of the concentrator as the inner radius of the concentrator is always the base point of the centre locus rather than the edge locus, hence the inner radius is smaller by $cos(\pi/18) = 0.98$. This causes significant errors in the PMT response, see section 5.4.1, and was corrected in the versions of SNOMAN used in the SNO analyses.

Using the combined fit lower radius of 97.4 and the fitted PMT shape gives the concentrator offset as 21.5mm.

3.2.3 SNO+ Modelling of the Concentrator Petals

Following the example of the previous concentrator in RAT, I will model the concentrator as a G4Polyhedra object. This has the advantage of being a single piece of geometry as with the GLG4TorusStack used for the PMT.

The G4Polyhedra code defines a profile in (r, z) a number of faces and angular limits defining the revolution around the z axis. The z axis is parallel to the PMT axis and the whole concentrator is placed relative to the PMT equator. The surface between the (r, z) points is interpolated linearly, which causes small deviations from the actual curved surface. These small deviations can be reduced by using a larger number and thus more finely spaced set of points. By simulating the response with 100 points rather than 21, I have found these small deviations do not affect the PMT response.

I have chosen the combined fit values to define the concentrator shape and offset. This leads to the profile points given in table 3.2 and an offset of 21.5mm as input to the G4Polyhedra code.

I have further chosen the petals to be 0.28mm thick; this is the average value I measured from three petals. The measurements also showed no variation above 0.01mm over the length of the petal.

3.2.4 SNO+ Modelling of the Concentrator Plastic

The plastic support for the petals has an inner surface shaped with a similar profile to that of the petal. The outer surface however has a circular cross section with flanges to meet the bucket. Further plastic lips hold and support the petals.

Optically the plastic volume combined with the bucket prevents photons reaching the PMT via any path that is not through the concentrator. This means that no photons are expected to interact with the outer plastic surface, any that do are absorbed. I have therefore decided to model the plastic geometry as the petals

r	z
[mm]	
0	97.4
5.4	103.4
10.8	107.1
16.2	110.3
21.5	113.1
26.9	115.7
32.3	117.9
37.7	112.0
43.1	121.8
48.5	123.6
53.9	125.2
59.2	126.7
64.6	128.0
70.0	129.2
75.4	130.4
80.8	131.3
86.2	132.2
91.5	132.9
96.9	133.5
102.3	134.0
107.7	134.5

Table 3.2: Points lying on the centreline locus of the inside face of the concentrator petals.

but at a large radius, with an added lip towards the top[5]. This simplification is justified as it fulfils the optical properties, whilst incorporating the material required for background simulation.

3.3 Bucket PSUP and PMTBase Geometry

3.3.1 Bucket Geometry

The inward-facing PMTs and concentrators are supported by a bucket, also called the panel sub-structure or hex cell. There was no previous model of the bucket in RAT[6]. The bucket is a hexagonal prism that surrounds the PMT and concentrator and then curves to meet the PMT base below the PMT neck (figure 7)[47].

Optically the bucket prevents photons reaching the PMT from any path other than through the concentrator, and absorbs all incident photons[7]. Therefore I have chosen to model the above PMT equator parts of the bucket as they exist, whilst below the equator the modelling tapers to the PMT base. This simplification is justified as it fulfils the optical properties, whilst incorporating the material required for background simulation.

3.3.2 PSUP

The PSUP or PMT support structure in SNO+ is a light tight geodesic structure. In the Monte Carlo the details of the PSUP are omitted, instead an opaque black shell is added to correctly simulate the light tight aspect.

[5]To prevent photon paths between the plastic and the bucket

[6]However a logical volume did surround the PMT and concentrator for CPU performance reasons.

[7]The actual bucket is slightly reflective

3.3.3 PMT Base

The PMT Base has no effect on the optical photons, as they can never reach it. However the PMT Base is important for background simulation, and thus I have added a geometry loosely based on the actual PMT base (figure 7)[47]. This simplified geometry correctly models the mass of material in the PMT base.

3.4 Full Geometry

Figures 3.9(a) and 3.9(b) show the full PMT geometry as added to RAT.

3.5 Panel Geometry

The inward facing PMTs are placed into buckets which are then tessellated into panels. The panels then form a geodesic pattern on a sphere approximately 8.5m away from the SNO+ detector centre. There are five panel designs designated S7, S19, T10, T14 and T21, where the numerical part defines the number of PMTs in either a snoflake shape (S prefix) or triangular shape (T prefix). To allow the hold-up ropes through the PSUP some T10 and T14 panels are missing PMTs, I have designated these panel types T10M and T14M.

3.5.1 Previous modelling

The previous modelling in RAT had no concept of panels. Furthermore each PMT was positioned incorrectly due to differing definitions between RAT and SNOMAN. In SNOMAN a PMT is positioned with respect to the concentrator front face (with is also the bucket front face) with a direction vector pointing from this position to the base of the PMT. In RAT a PMT is positioned with respect to the PMT origin (intersection of PMT axis and equator) with a direction vector pointing from this position to the front of the PMT.

3.5.2 New Modelling

I have added the panel tessellation to RAT and corrected the PMT position and direction. The database file uses the SNOMAN position definition, as this is what can be and has been measured, which is then converted in the code. The panel designs are shown in figure 3.10.

3.6 Conclusion

A much better modelling of the geometry now exists in RAT based on recent measurements of the geometry. This modelling has many improvements on the previous modelling in both RAT and SNOMAN, all will allow for a more accurate PMT simulation. This change was accomplished by completely replacing the RAT-Initial code. The new code is written in c++ to meet the RAT standards and to integrate with Geant4.

The geometric changes along with changes to the optical physics, as discussed in chapter 4, cause differences in the PMT response as discussed in chapter 5. However, the changes are justified by the information given in this chapter alone, i.e. the measurements. Hence, any disagreement with SNOMAN must be checked against SNO+ data.

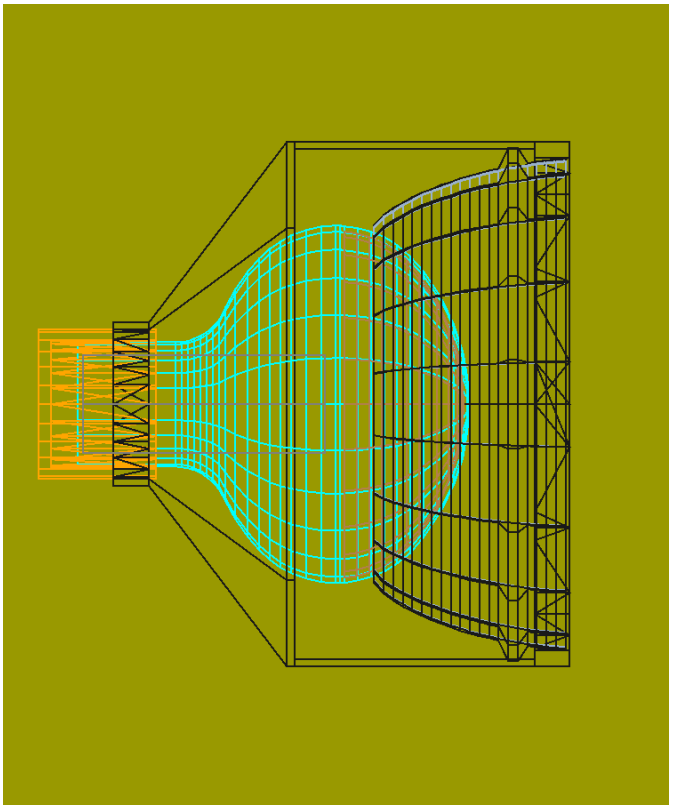

(a) Side view of the full Inward Facing PMT geometry.

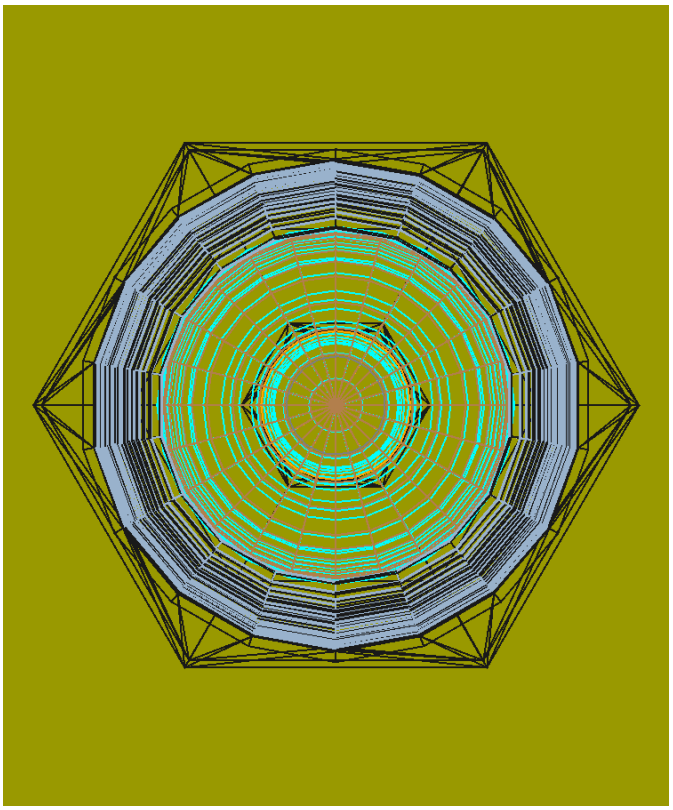

(b) Top view of the full Inward Facing PMT geometry.

Figure 3.9: Full Inward Facing PMT geometry as visualised in the HepRApp viewer. This geometry is as simulated.

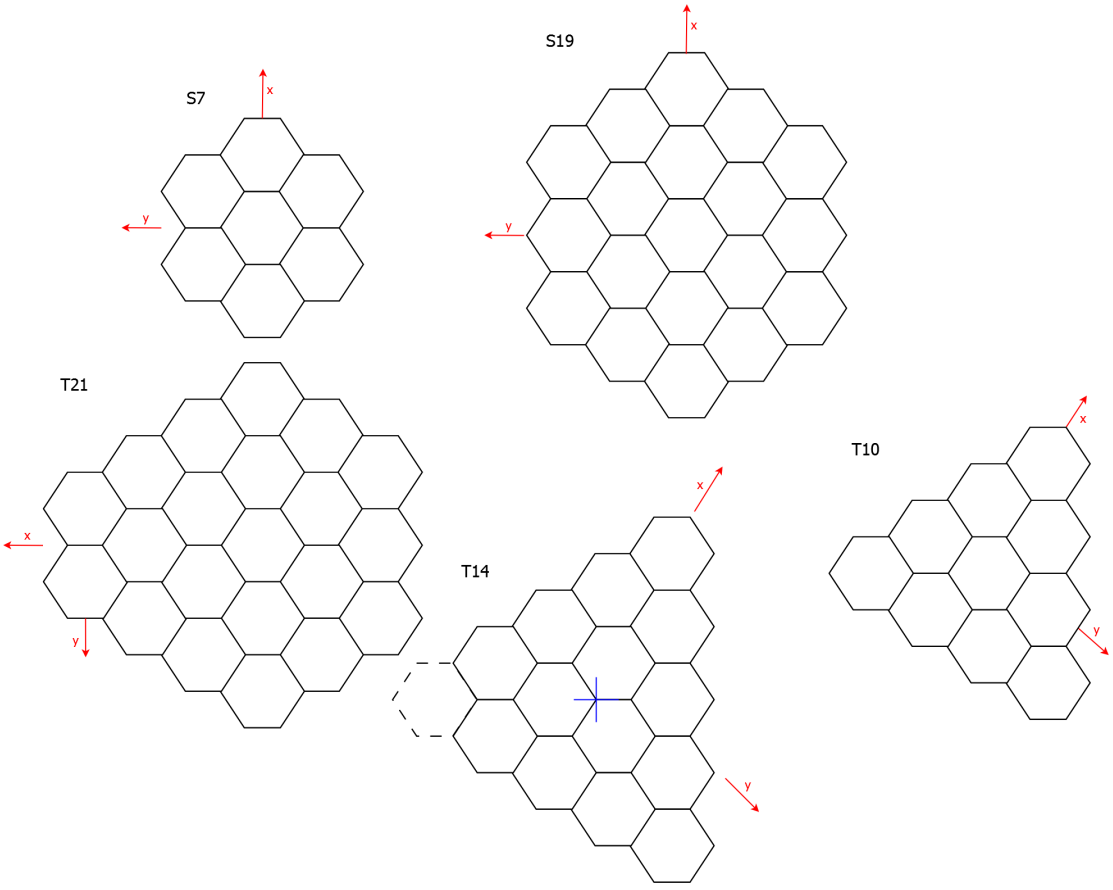

Figure 3.10: Sketches of the tessellation patterns giving rise to the SNO+ panel types: S7, S19, T21, T14, T10.

Chapter 4

Simulating the PMT and Concentrator Optics

The physics of the PMT optical simulation is presented, including the concentrator and photocathode. The previous simulations in RAT and SNOMAN are compared.

As the PMTs in SNO+ are the only source of information, the Monte Carlo must accurately determine whether a photon entering the PMT geometry causes a signal and track photons in the concentrator. Therefore correct simulation is crucial to accurately simulating the response of the detector. RAT includes a detailed physical simulation of photons interacting with the PMT and concentrator geometries, with the further geometries described in section 3 simulated as perfect absorbers. This chapter details the known physics of the PMTs and concentrators alongside their simulation in RAT.

4.1 Concentrator Optics

The concentrator contains optically reflective petals shaped to increase the light collection from the SNO+ fiducial volume. These petals are coated with a multi-layered surface designed to increase the reflectivity.

The simulation of the concentrator consists entirely of simulating the tracking to the petal and/or plastic volume surfaces followed by simulating the reflection or absorption at the surface boundary. The simulation of photons within the concentrator is controlled by a fast simulation model, instead of Geant4. This is necessary due to the unique reflectivity of the concentrator, especially when ageing is considered. A fast simulation model instructs Geant to allow the tracking and physical simulation in a defined geometric region to be simulated by a bespoke piece of code. I have written the bespoke code for the concentrator simulation in c++.

The fast simulation model tracks photons in a geometric region around the concentrator, which consists of the plastic and petal volumes plus a skin region of water. The tracking uses the Geant4 geometry definitions as described in chapter 3, and tracks to boundaries. Changes to the track are only simulated at boundaries, i.e. no attenuation is simulated during transit, hence requiring that the water skin depth is small.

On intersection with the plastic boundary the track will be absorbed, whereas on intersection with the petal the track may be reflected. The probability that the photon is reflected is given by the specular and diffuse reflectivity values. The petal specular reflectivity is expressed as a tabular function of wavelength, incident angle and polarisation $R_s = R_s(\lambda, \theta, p)$. This table was measured by Waltham *et al.* [61] between [20, 75]° and extended to [0,90]° by M D Lay[58]. The petal diffuse reflectivity is set as a constant $R_d = 0.02$.

The R_s value depends on the photon polarisation, which is calculated using the definitions, direction $\vec{d}$, polarisation $\vec{p}$, and surface normal $\vec{n}$.

$$s_{fraction} = \mid \vec{p} \cdot \vec{d} \times \vec{n} \mid \tag{4.1}$$

A random number r is then checked against $s_{fraction}$, if $r < s_{fraction}$ the photon is

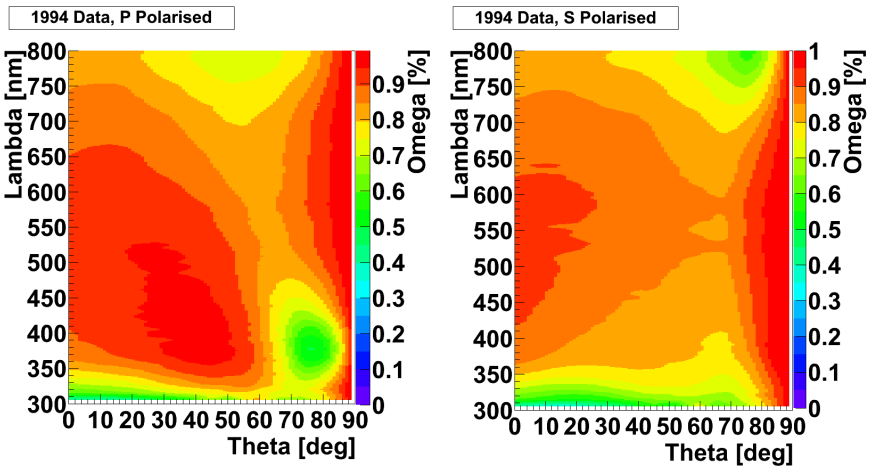

Figure 4.1: Petal (Omega) reflectivity as a function of wavelength (ordinate) and angle (abscissa) for p and s polarised photons. Data as measured by Waltham *et al.* [61] and extended by M D Lay[58].

considered s polarised otherwise it is p[1] polarised. A second random number r' is then generated, if $r' > R_s$ the photon is absorbed, if $r' > P_s - P_d$ the photon is diffuse reflected, otherwise the photon is specular reflected.

The specular reflected photon direction $\vec{d'}$ and polarisation $\vec{p'}$ are calculated assuming $\vec{n} \cdot \vec{d} < 0$ with initial, direction $\vec{d}$, polarisation $\vec{p}$, and surface normal $\vec{n}$, via:

$$\vec{d'} = \vec{d} - 2(\vec{d} \cdot \vec{n})\vec{n} \tag{4.2}$$

$$\vec{p'} = \vec{p} - 2(\vec{p} \cdot \vec{n})\vec{n} \tag{4.3}$$

The diffuse reflected photon direction and polarisation are calculated by first calculating a random angle to the normal θ and a random azimuthal angle ϕ then

[1]S for senkrecht, German for perpendicular. P for parallel

calculating a vector $\vec{r}(\theta, \phi)$:

$$\sin\alpha = \sqrt{1 - \vec{n}_z^2} \tag{4.4}$$

$$\cos\beta = \frac{\vec{n}_x}{\sin\alpha} \tag{4.5}$$

$$\sin\beta = \frac{\vec{n}_y}{\sin\alpha} \tag{4.6}$$

$$\vec{r}_x = \cos\theta * \vec{n}_x + \sin\theta * (\vec{n}_z * \cos\phi * \cos\beta - \sin\phi * \sin\beta) \tag{4.7}$$

$$\vec{r}_y = \cos\theta * \vec{n}_y + \sin\theta * (\vec{n}_z * \cos\phi * \sin\beta + \sin\phi * \cos\beta) \tag{4.8}$$

$$\vec{r}_z = \cos\theta * \vec{n}_z - \sin\theta * \cos\phi * \sin\alpha \tag{4.9}$$

The diffuse reflected direction is $\vec{d'} = \vec{r}(\theta', \phi')$ where $\theta' \in [0, 0.99 * \pi/8]$ and $\phi \in [0, 2\pi]$. The diffuse reflected polarisation is $\vec{p'} = \vec{r}(\theta'', \phi'')$ where $\theta'' = \pi/2$ and $\phi \in [0, 2\pi]$. This technique was taken from the SNOMAN Monte Carlo.

4.1.1 Previous concentrator simulation

The petal reflectivity was previously simulated in RAT as a Geant4 optical surface. This surface was incorrectly given a reflectivity $R = 0.99$, and gave rise to entirely specular reflection.

In SNOMAN the specular reflectivity is expressed as in figure 4.1, and the diffuse reflectivity is $R_d = 0.02$. However, during the lifetime of the SNO experiment the petals have aged, changing the reflectivity of the petal surface. This change was simulated in SNOMAN by a combination of a petal correction factor and PMT collection efficiency correction factor (see section 4.2.2). The correction factor used was a tabular function of incident angle to the bucket and wavelength.

4.1.2 Ageing simulation

The petals have aged during the lifetime of the SNO experiment, leading to changes in the response of the PMT and concentrators. This ageing is thought to occur

when the outer layer of TiO_2 detaches from the petal and enters the light water. Aged petals can be seen in figure 4.2, note the non-uniform ageing by position and extent.

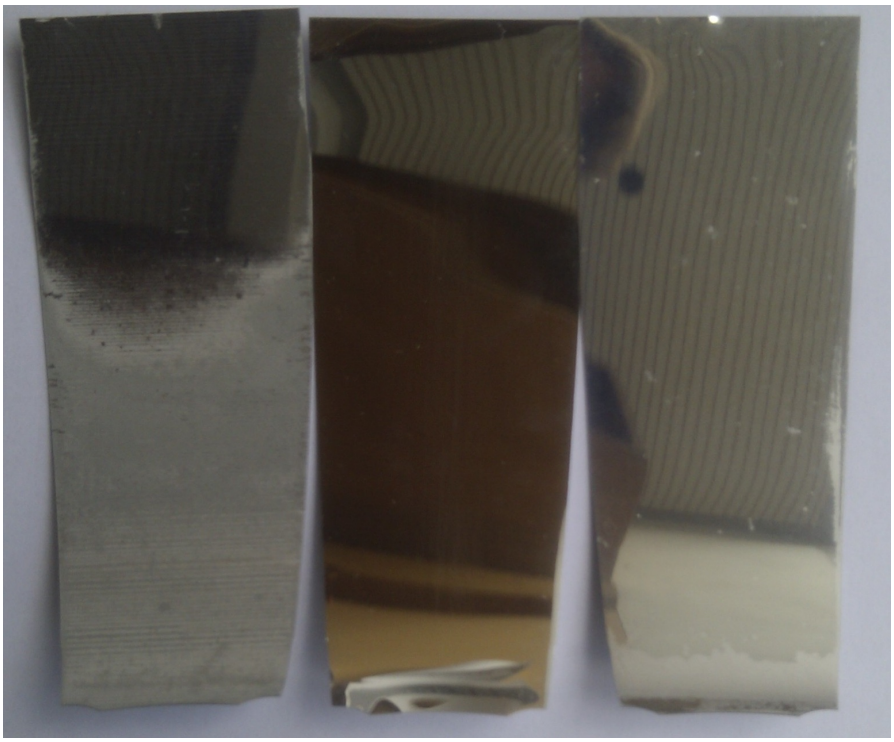

Figure 4.2: Three aged petals, the centre petal is effectively un-aged having existed in an office during the SNO experiment. The left and right petals are from the spare PMTs placed into the detector. Notice that despite equal time in the detector the effects of ageing is non-uniform, with the left petal showing ageing on over half its surface whereas the right petal shows ageing only at the base.

Most aged petals observed have ageing similar to the right most petal in figure 4.2, i.e. a small (∼10mm) band of ageing at the base. Thus a well motivated model is to age the lowest 10mm of the petal more severely than the upper 97mm. This model is currently being developed and refined, however initial trial results are shown in figure 4.3. Figure 4.3 shows the normalised angular response difference in models for 100% lower region ageing and 0% upper region, i.e. it shows the model limit. The normalised angular response is the ratio of photons causing signals to photons hitting the PMT as a function of incident angle to the PMT axis, normalised to the response at normal incidence.

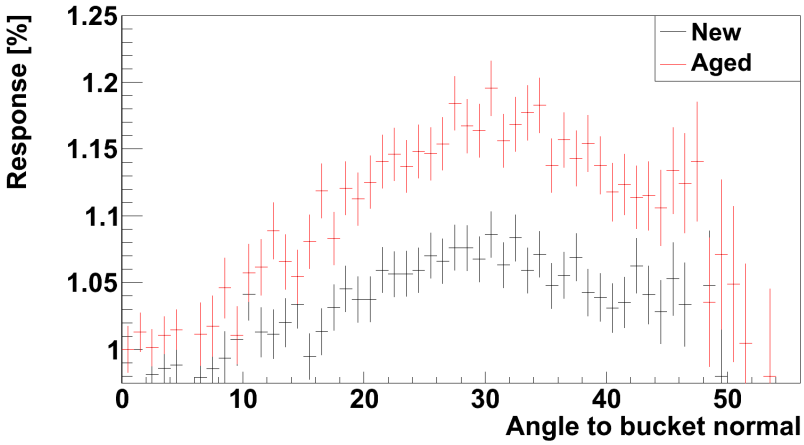

Figure 4.3: Normalised PMT angular response shown for simulated aged and new concentrators. Simulated for photons with wavelength 420nm.

The effect of the lower region ageing on the normalised angular response can be understood by considering the concentrator hit position for normal incidence photons, figure 4.4. Figure 4.4 shows the hit position distribution is strongly peaked at the base of the petal, $Z = [20, 30]$mm. This peak is less strong for photons with greater incident angles. Hence ageing this region of the petal more than the rest of the petal should raise the high angle response relative to the normal response, as in figure 4.3.

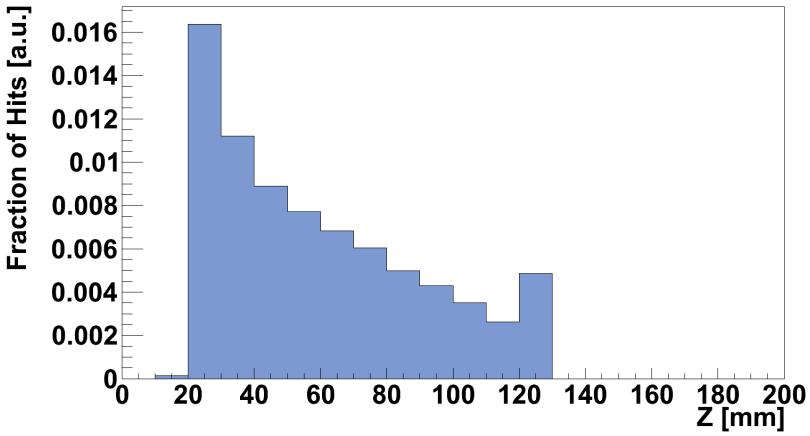

Figure 4.4: Concentrator hit Z distribution for normal incidence photons (from the AV). Note the peak at low Z values. The base of the concentrator is at 21.5mm.

This model does not however match the observed data taken during SNO,

shown in figure 4.5. Figure 4.5, shows the high angle normalised response decreasing with ageing time, contrary to the model developed. The ageing model has shown that it is possible to change the angular response of the PMT plus concentrator by just varying the concentrator ageing. Further work beyond this thesis is required to refine and produce a working model.

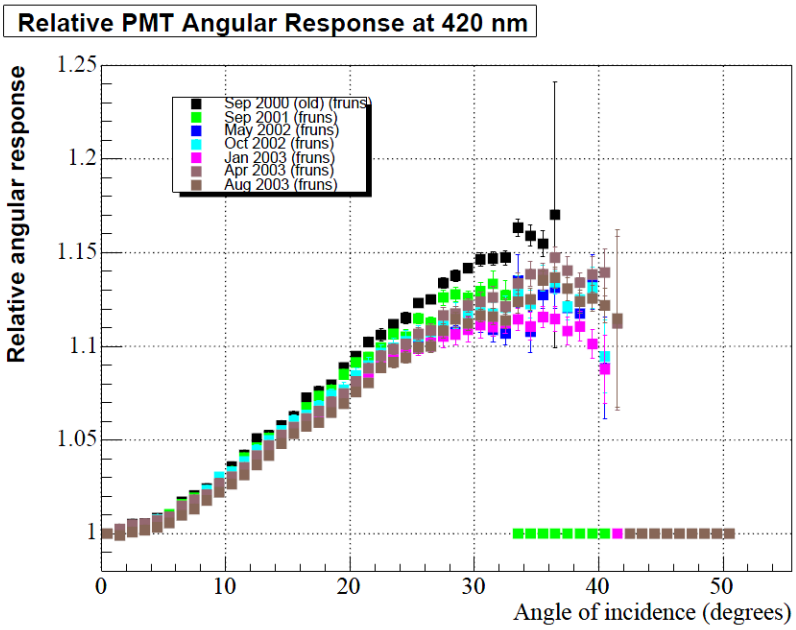

Figure 4.5: Normalised PMT Angular Response shown for different dated Laserball calibrations at 420nm. Figure from [62].

4.2 PMT Optics

PMTs are highly sensitive photon detectors, which are used in SNO+ to detect single photons. These detected photons enter the PMT glass, reach and are absorbed in the photocathode. If the photon has sufficient energy it will liberate a photoelectron from the photocathode. A strong electric field between the photocathode and the first dynode then accelerates the photoelectron to the first dynode. Upon reaching the first dynode the photoelectron will have gained enough energy to liberate more electrons. A strong electric field to the next dynode ensures that the

From↓ To→	Outer	Glass	Upper	Middle	Lower	Dynode
Outer	-	Geant4‡	-	-	-	-
Glass	Fresnel	-	Thin film	Fresnel†	Fresnel†	-
Upper	-	Thin film	-	-	-	-
Middle	-	Thin film⋆	-	-	-	-
Lower	-	Fresnel†	-	-	-	Reflection
Dynode	-	-	-	-	-	-

Table 4.1: Physical processes simulated when photons cross boundaries. The inner vacuum volume of the PMT is split into three parts, the upper part has a photocathode boundary with the glass, the middle part has a photocathode overlapping aluminium boundary with the glass and the lower part a alumiunium boundary with the glass. †: Fresnel with no transmission. ⋆: Thin film with no transmission and the final media being aluminium, as opposed to glass. ‡: Simulated by Geant4, not the bespoke PMT fast simulation model.

liberated electrons then liberate more at the next dynode. This process continues down the dynode stack, until at the anode enough charge is present to detect a signal. This anode pulse is then processed in the DAQ to form the detector data.

The simulation of a PMT consists of tracking the photons through the material volume and across boundaries. Then if the photon is absorbed in the photocathode the probability of a signal is used to decide if the Monte Carlo DAQ receives a signal. If so the Monte Carlo DAQ then simulates the charge and shape of the anode pulse. The optical boundary interactions are summarised in table 4.1.

The simulation of the processes in table 4.1 and the tracking between the volumes is done by a bespoke fast simulation model, written by myself. The Geant4 geometry definitions are used to correctly track the photon through the volumes. No attenuation in the glass[2] is included in the simulation, as this is negligible given the long glass attenuation length and short paths in the glass.

[2]The vacuum volumes and photocathode are the only other traversed volumes, and they do not attenuate.

4.2.1 Photocathode simulation

The photocathode is a thin film bialkali coating of the inner glass surface. This coating is applied by evaporating beads of the bialkali material placed on the top of the dynode stack[57]. This leads to a variable thickness film as a function of position. Furthermore the film thickness is a compromise between absorbing the photons and allowing the photoelectron to escape. The escape probability for the electron is the quantum efficiency, which is characterised as a function of wavelength. The quantum efficiency is then multiplied by the collection efficiency to give the signal probability.

The optical simulation of the photocathode consists of evaluating the thin film equations as derived in (Appendix B)[58]. These equations, summarised in appendix B, give s and p polarised reflectivity and s and p polarised transmission probabilities, R_s, R_p, T_s, T_p respectively. These values are a function of the photon wavelength, incident angle, complex refractive indices of the photocathode, glass and vacuum/aluminium[3] (in order of transit) and photocathode thickness. Using equation 4.1 allows the reflection, transmission and absorption probabilities to be calculated as:

$$R = s_{fraction} * R_s + (1 - s_{fraction}) * R_p \tag{4.10}$$

$$T = s_{fraction} * T_s + (1 - s_{fraction}) * T_p \tag{4.11}$$

$$A = 1 - T - R \tag{4.12}$$

The refractive index of the glass is set to $n_{Glass} = 1.49$, vacuum $n_{Vacuum} = 1.0$ and complex refractive index of the photocathode $\tilde{n}_{PC} = n(\lambda) + ik(\lambda)$. The aluminium refractive index is discussed in the next section. The photocathode values are shown in figure 4.6, these are the values measured by Lay [63].

[3]Depending on photon position, as the aluminium overlaps the photocathode in the middle volume.

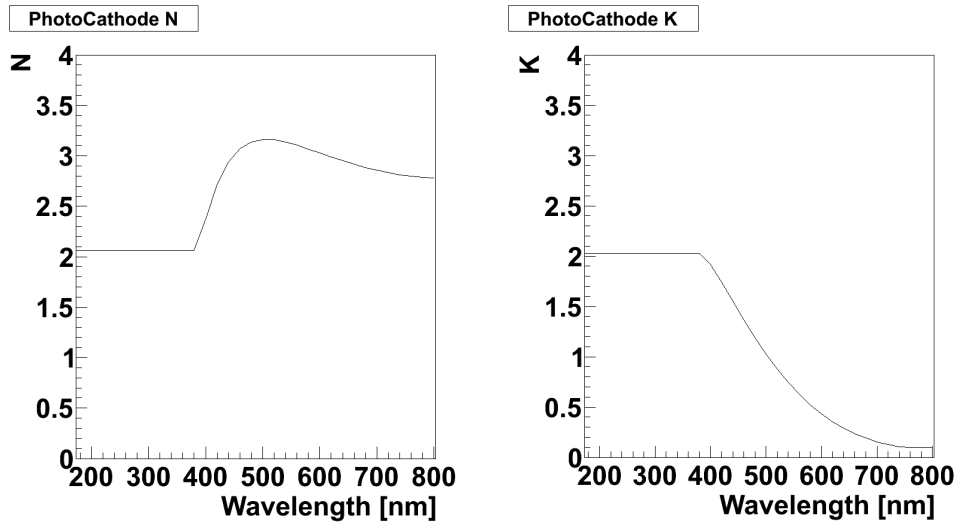

Figure 4.6: Complex refraction index of the photocathode as a function of photon wavelength as measured by Lay [63]. $\Re$eal part on left, $\Im$maginary part on right.

The thickness τ of the photocathode was also measured by Lay in two locations, on the PMT axis and at the sphere toroid transition point. On the PMT axis $\tau = 27.99$nm, it is then expected to vary as the inverse of the distance from the dynode centre squared, due to the evaporation process. Lay found the sphere toroid transition point to be consistent with this hypothesis[58]. The functional form shown in figure 4.7, is a smooth analytic approximation to this hypothesis with a maximum thickness at the centre of 27.99nm. This functional form was chosen by J Dunmore [64].

If the photon is absorbed the signal probability is then calculated as a product of the quantum efficiency and collection efficiency. The quantum times collection efficiency used as a function of wavelength is shown in figure 4.8, measured by S D Biller *et al.* [65]. The actual efficiency value will be measured by calibration.

Aluminium Simulation

The aluminium coating is not a thin film coating and thus it is not transparent; furthermore it is assumed that all reflection is specular. This allows the photon aluminium interaction to be described by the Fresnel equations with the constraint

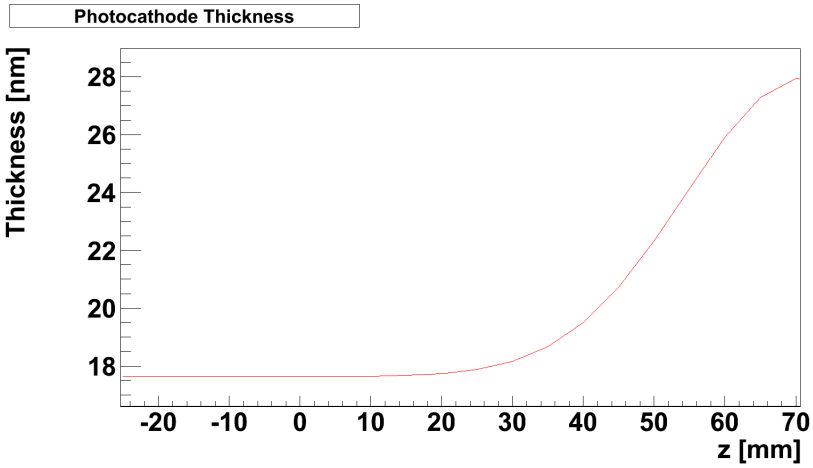

Figure 4.7: Smooth analytic form for the photocathode thickness as a function of distance above the PMT equator, Z.

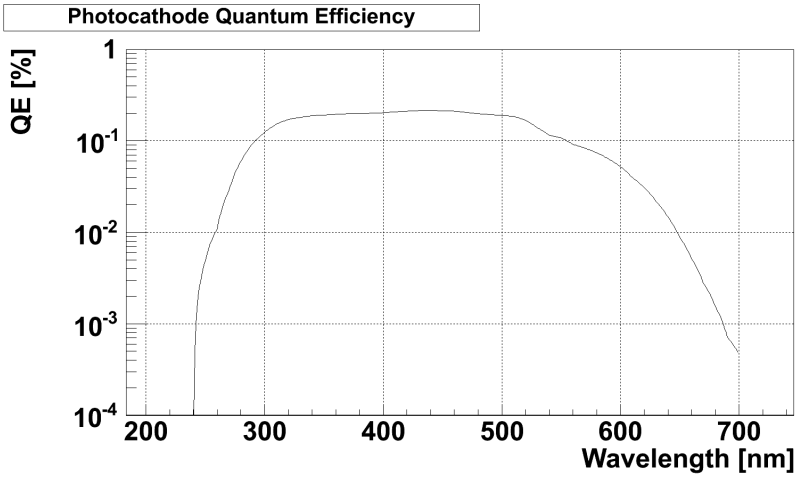

Figure 4.8: Quantum times collection efficiency as a function of wavelength, measured by S D Biller *et al.* [65].

that T=0. Hence the reflectivity is given by, using the existing definitions:

$$\cos\theta_i = \vec{d}\cdot\vec{n} \tag{4.13}$$

$$\cos\theta_t = \sqrt{1-(\frac{n_1}{n_2})^2*(1-\cos\theta_i{}^2)} \tag{4.14}$$

$$R_s = \left(\frac{n_1\cos\theta_i - n_2\cos\theta_t}{n_1\cos\theta_i + n_2\cos\theta_t}\right)^2 \tag{4.15}$$

$$R_p = \left(\frac{n_1\cos\theta_t - n_2\cos\theta_i}{n_2\cos\theta_i + n_1\cos\theta_t}\right)^2 \tag{4.16}$$

$$R = s_{fraction}*R_s + (1-s_{fraction})*R_p \tag{4.17}$$

$$A = 1-T-R \tag{4.18}$$

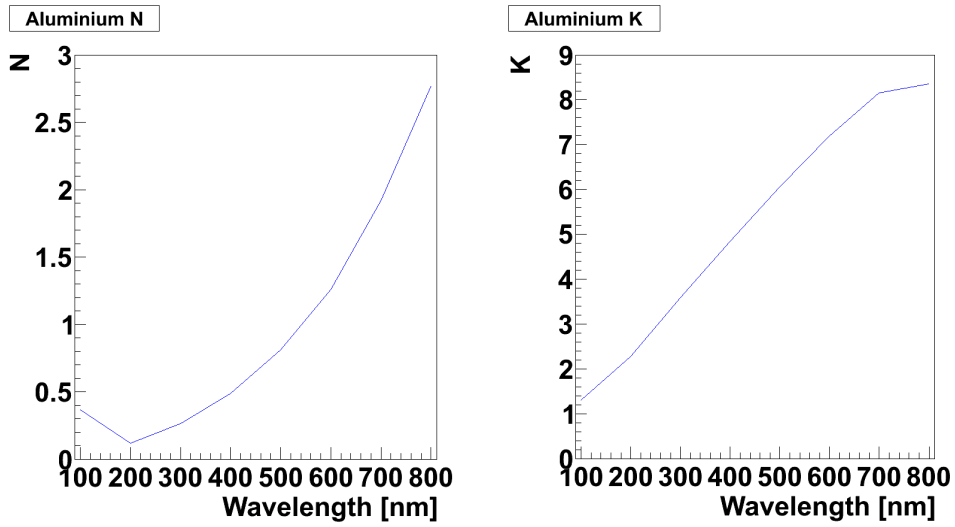

Figure 4.9: Complex refraction index of aluminium as a function of photon wavelength from [66]. $\Re$eal part on left, $\Im$maginary part on right.

The complex refractive index values for the aluminium shown in figure 4.9, are taken from [66].

The dynode stack is simulated as a homogeneous object with reflectivity $R = 0.4$[64].

4.2.2 Previous PMT simulation

The PMT was simulated in RAT-Initial using the GLG4 PMT optical model. This model split the PMT simulation, with the upper half simulated by a bespoke fast simulation model and the lower by Geant4. This neglected the photocathode aluminium overlap region in the middle PMT volume, which I have subsequently introduced. Furthermore the aluminium was incorrectly given a reflectivity $R = 0.99$. However, the photocathode simulation followed the thin film equations as above.

In SNOMAN the photocathode followed the thin film equations as above, with an additional modified collection efficiency (MCE). This changed the signal probability to be the product of the quantum efficiency, collection efficiency and modified collection efficiency. The MCE was included using empirical data to model the

ageing of the concentrator. Furthermore, in SNOMAN the aluminium is simulated with a constant complex refractive index, rather than wavelength dependent as used currently.

4.2.3 Future Improvements

It is known that the collection efficiency and gain vary depending upon the photon absorption position[67]. Furthermore, it is known that the photocathode thickness also varies with position. Given the effect of the concentrator is to concentrate incoming photons onto the PMT photocathode non-uniformly these unknowns may lead to a different response than is currently simulated.

To measure the position-dependent collection efficiency and gain I have helped set up an experiment at the University of Pennsylvania. This experiment will measure the relative change in collection efficiency and gain as a function of position. This measurement should report results in early 2012. The absolute value of the collection efficiency will then be measured *in situ* via calibration.

4.3 Conclusion

Much better modelling of the optical physics now exists in RAT with improvements on the previous modelling in both RAT and SNOMAN. This will allow RAT to model the ageing in the concentrator rather than the PMT. This change was accomplished by completely replacing the RAT-Initial code. The new code is written in c++ to meet the RAT standards and to integrate with Geant4.

The optical physics changes, along with changes to the geometry, cause differences in the PMT response as discussed in chapter 5. However, these changes are justified by the information given in this chapter alone. Hence, any disagreement with SNO+ data must be incorporated into the ageing model of the concentrators.

Chapter 5

Monte Carlo Verification

The verification of RAT against SNOMAN is presented for Čerenkov data. The calibration plan for the PMTs including ageing is also presented.

The RAT Monte Carlo must be verified before it can be used to predict the SNO+ experiment and allow physical limits, etc, to be set. The verification of the Čerenkov physics has been done by myself and G Beier. The verification of the photon transport and PMT model has been done by myself. Further verification of the scintillator model, DAQ, etc, has been carried out by the SNO+ Collaboration.

5.1 Verification Process

The Čerenkov photon transport and PMT simulation can be verified against the understood SNOMAN Monte Carlo and SNO calibration data. The SNOMAN Monte Carlo is the better verification source as Monte Carlo information is easily accessible and has been verified against SNO data[1]. However as stated in previous chapters, improvements on the SNOMAN PMT model have been made. Therefore the verification will be done with the SNOMAN PMT geometry and physics

[1]Comparing two Monte Carlos allows the simulation to be well defined and equivalent in both.

running in RAT. Hence forth I will refer to RAT running the SNOMAN PMT geometry and physics as RAT-SNOMAN.

The N16 calibration source used in SNO is well understood and modelled in SNOMAN. Furthermore it produces a continuous wavelength spectrum over which the PMT response can be analysed. Therefore I have decided to compare RAT-SNOMAN and SNOMAN primarily using the principle N16 gamma, in the salt phase of SNO. The salt phase of SNO is chosen as I have access to a calibrated N16 run's data.

The primary comparison will be made between the summed PMT hit times and the number of hits per event (Nhit) histograms. The PMT hit time histogram has a number of features shown in figure 5.1 that are expected to exist and align between RAT and SNOMAN. Furthermore the relative heights of these features should agree. The Nhit histogram mean and sigma are expected to agree between RAT and SNOMAN.

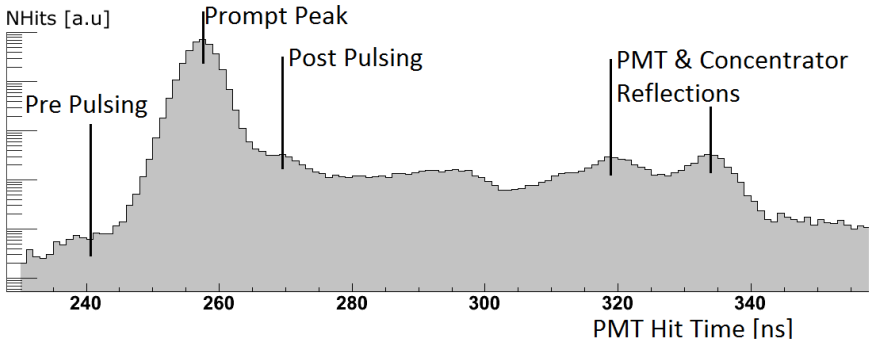

Figure 5.1: Features of the PMT hit timing spectrum.

The initial comparison of RAT-Initial to SNOMAN is shown in figure 5.2. RAT-Initial does not reproduce the PMT and concentrator reflection features, particularly the later concentrator reflection peak is much higher than the PMT reflection peak. RAT-Initial also has far too many PMT hits per event than SNOMAN.

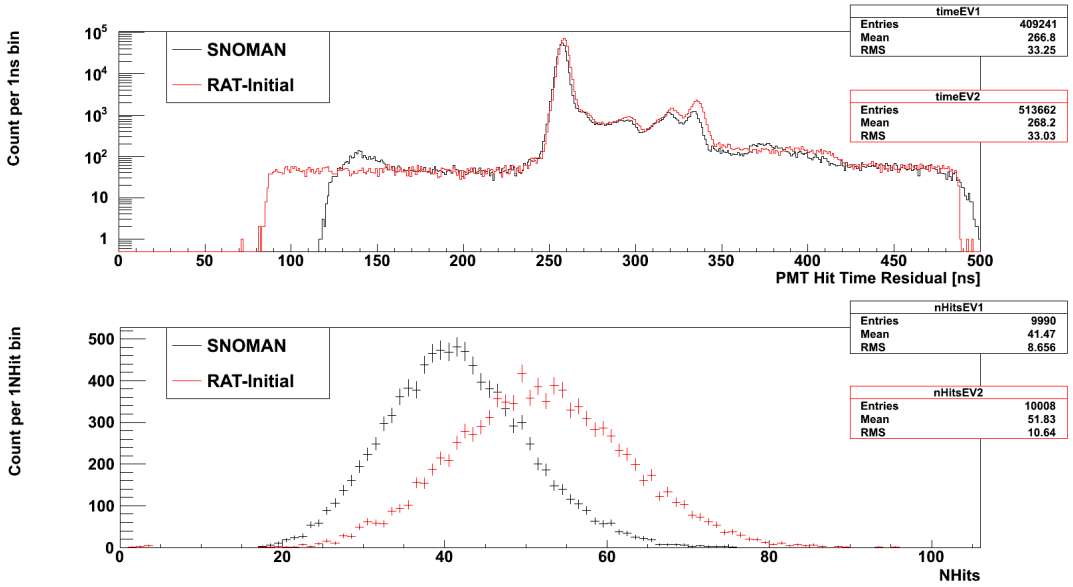

Figure 5.2: Timing and Nhit comparison between SNOMAN and RAT-Initial. Discussion in main text.

5.2 Čerenkov Simulation

A charged particle polarises its surrounding medium, which causes an electromagnetic wave to propagate when the particle moves. If the particle moves faster than the speed of light in the medium then constructive interference occurs emitting coherent photons. This process is called Čerenkov radiation as first explained by P Čerenkov [68].

The photons are emitted at an angle θ to the particle momentum such that:

$$\cos\theta = \frac{1}{n(\epsilon)\beta} \tag{5.1}$$

Where $n(\epsilon)$ is the refractive index for photons of energy ϵ and β is the ratio of the charged particle speed to the speed of light. This introduces a limit on the values of β which can produce Čerenkov light such that:

$$\beta n(\epsilon) > 1 \tag{5.2}$$

For electrons a value $n = 1.34$ (in D_2O) gives $E_{electron} \geq 0.768$MeV whilst for a value (in scintillator) $n = 1.48$ gives $E_{electron} \geq 0.693$MeV. The number of photons emitted dN per path length dx per photon energy $d\epsilon$ is given by[24]:

$$\frac{dN}{dx} = \frac{\alpha z^2}{\hbar c} I(\epsilon_{min}, \epsilon_{max}) \tag{5.3}$$

$$I(\epsilon_{min}, \epsilon_{max}) = \int_{\epsilon_{min}}^{\epsilon_{max}} \left(1 - \frac{1}{n^2\beta^2}\right) d\epsilon \tag{5.4}$$

Hence the $\frac{dN}{dx}$ value is calculated as the integral over the allowed photon energies. The allowed photon energies correspond to the transparency of the medium and the values that satisfy equation 5.2.

For D_2O the limits are 220nm to 710nm as these values are safely beyond the PMT sensitivity range, see section 4.2.1. This reduced range saves unnecessary computing effort in tracking photons that can never be detected. In scintillator however, photons are absorbed and re-emitted implying the need to extend these limits. Fortunately for the smaller wavelength extension, photons are absorbed and effectively re-emitted instantly[69]. Thus this effect can be incorporated into the overall light yield. Whereas for the large wavelength extension, the photons are not absorbed and re-emitted (absorption stops at 400nm)[69], hence as with D_2O these photons can be ignored. Therefore the scintillator limits are conservatively set as 200nm to 800nm.

The energy distribution of the emitted photons is sampled from the density function

$$\left(1 - \frac{1}{n^2\beta^2}\right) \tag{5.5}$$

5.2.1 Čerenkov Comparison of RAT-Initial to SNOMAN

Using a simulation of 6.13MeV gammas at a set position in D_2O within the AV in both RAT-Initial and SNOMAN indicated a discrepancy between RAT-Initial and SNOMAN. RAT-Initial produced too many photons relative to SNOMAN as

the photon energy limits ϵ_{min} and ϵ_{max} were set to the equivalent of 200nm and 800nm respectively. As D_2O is not a scintillating medium I changed these values to match the SNOMAN convention of 220nm and 710nm. As the extra photons in RAT-Initial are between [200,220]nm and [710,800]nm this change did not affect the detector response due to the PMT sensitivity range.

RAT calculates the integral $I(\epsilon_{min}, \epsilon_{max})$ in equation 5.4 differently to SNOMAN. SNOMAN assumes a constant value for $n(\epsilon) = 1.337 \; \forall \; \epsilon$ (for D_2O), whereas RAT evaluates the equation via the trapezium rule. This causes a discrepancy in the number and energy distribution of Čerenkov photons emitted as shown in figures 5.3 and 5.4.

In figures 5.3 and 5.4 SNOMAN is plotted against RAT-Initial with a constant refractive index V3P and a variable refractive index V3. Figure 5.3 shows that RAT will emit $\approx 1\%$ less photons than SNOMAN if RAT-Initial assumes a constant refractive index. This indicates a difference in the simulation of the energy loss physics, i.e. $\frac{dE}{dX}$, whilst figure 5.4 shows that if RAT assumes a constant refractive index it will reproduce the SNOMAN results (SNOMAN and V3P agree).

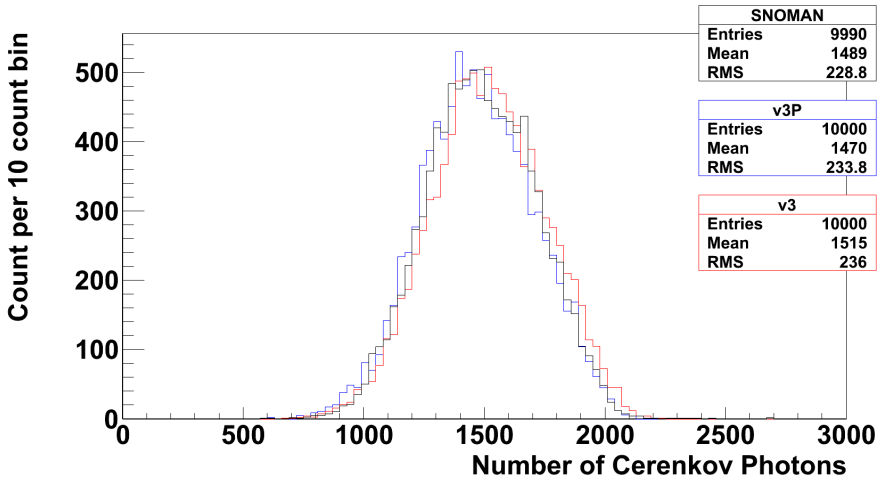

Figure 5.3: Number distributions of emitted Čerenkov photons for SNOMAN, V3P - RAT with physics list V3 and $n(\epsilon) = 1.337 \forall \epsilon$, and V3 - RAT with physics list V3 and variable $n(\epsilon)$.

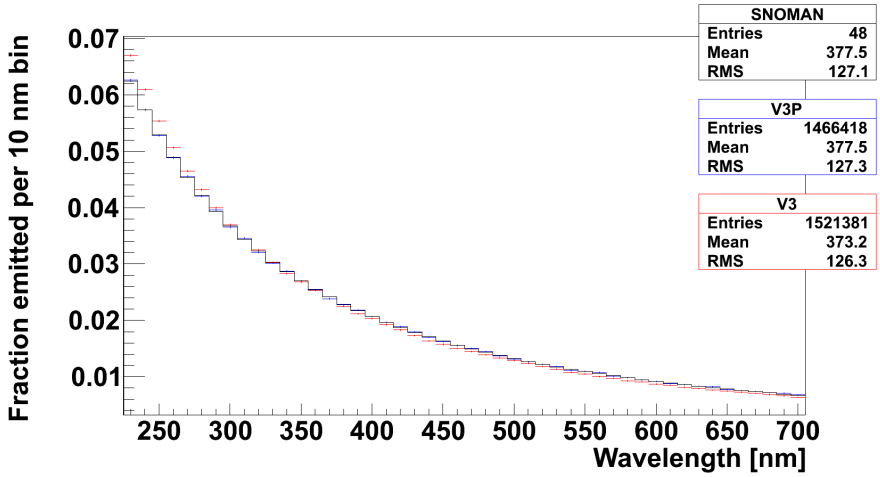

Figure 5.4: Normalised energy distributions of emitted Čerenkov photons for SNOMAN, V3P - RAT with physics list V3 and $n(\epsilon) = 1.337 \forall \epsilon$, and V3 - RAT with physics list V3 and variable $n(\epsilon)$.

The SNOMAN assumption thus alters the energy distribution and increases the number of Čerenkov photons. However, any difference between SNOMAN and data was incorporated into the overall hit correction factor. This simplifying assumption is not appropriate for SNO+ as scintillator is much more dispersive than D_2O. Therefore I have decided that RAT will not make the SNOMAN assumption. This difference was also simultaneously identified by G Beier who came to the same conclusion regarding the SNOMAN assumption.

5.2.2 Physics List Changes

The RAT Čerenkov process has been verified and found to be more accurate than SNOMAN. However Čerenkov photon production is not the dominant source of energy loss for charged particles. The electromagnetic (EM) processes in RAT are simulated by Geant4 using the Geant4 models defined in the RAT physics list. Hence the final source of discrepancy in Čerenkov photon numbers between RAT-Initial and SNOMAN are due to the choice of the Geant4 models.

The present version of Geant, 4.9.4 has four general choices of EM models; standard, low energy, Penelope and very low energy. Following the decision of G

Beier, I wrote two new physics Lists using the Penelope models. The Penelope models are designed for low energy physics, i.e. the MeV energy range in SNO+. These physics lists use the standard EM physics with the Penelope models for ionisation, bremsstrahlung, e+e- annihilation, Compton scattering, photo-electric effect and gamma conversion. The RAT-Initial physics list, termed V1 in this thesis, used the low energy EM models. The two new physics lists differ in the version of the Penelope model with version 2 (V2) using an older version that is obsoleted in Geant 4.9.4 and version 3 (V3) using the replacements.

The number of Čerenkov photons produced running RAT-Initial with each physics list for 6.13MeV gammas is shown in figure 5.5. The large change from V1 to V2 is due to the different EM model choice. From the comparison with SNOMAN, it is clear that Penelope is currently the better choice for RAT. V2 and V3 are consistent as expected and hence V3 will be used in the rest of this thesis.

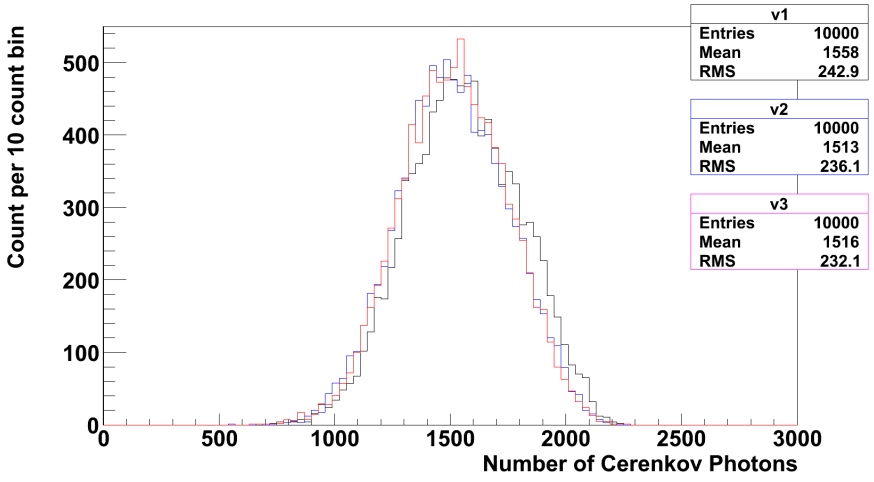

Figure 5.5: Number of Cerenkov Photons for the three Physics Lists in RAT. A large difference is seen between V1 and V2/V3 whereas V2 and V3 are consistent. This is as expected.

In conclusion there are two properties that affect the number of PMT hits due to Čerenkov photons, the number of photons and the energy distribution. Both of these properties are affected by the physics list and Čerenkov process. Overall

there is good agreement in the energy distribution of photons between RAT and SNOMAN, figure 5.4, and number of photons, figure 5.3. The final 1% difference between RAT and SNOMAN will be calibrated out during the water phase of SNO+.

5.3 Attenuation

The absorption and Rayleigh scattering processes are simulated by RAT rather than Geant4. Both processes have previously been verified against theory and SNOMAN. However the number of photons reaching the PSUP region in RAT-Initial is higher than SNOMAN.

In RAT the absorption is parameterised as a discrete set of absorption lengths $L_i(\lambda_i)$ in mm as a function of wavelength. In SNOMAN the absorption is parameterised as a discrete set of absorption coefficients $a_i(\lambda_i)$ in cm^{-1} as a function of wavelength. These are related such that $L_i(\lambda_i) = 10/a_i(\lambda_i)$.

RAT linearly interpolates between the absorption lengths whilst SNOMAN linearly interpolates between the absorption coefficients. This results in the discrepancy when the values are coarsely binned in wavelength. Consider the value between two SNOMAN absorption coefficients $a_1(\lambda_1)$, $a_2(\lambda_2)$ with $\lambda_2 > \lambda_1$, then

$$a'(\lambda') = \frac{a_2(\lambda_2) - a_1(\lambda_1)}{\lambda_2 - \lambda_1} \cdot (\lambda' - \lambda_1) + a_1(\lambda_1) \tag{5.6}$$

whilst the equivalent in RAT is

$$L'(\lambda') = \frac{L_2(\lambda_2) - L_1(\lambda_1)}{\lambda_2 - \lambda_1} \cdot (\lambda' - \lambda_1) + L_1(\lambda_1) \tag{5.7}$$

Clearly $L'(\lambda') \neq a'(\lambda')$ as equation 5.6 does not equal 5.8.

$$\frac{L'(\lambda')}{10} = \frac{1/a_2(\lambda_2) - 1/a_1(\lambda_1)}{\lambda_2 - \lambda_1} \cdot (\lambda' - \lambda_1) + 1/a_1(\lambda_1) \tag{5.8}$$

I fixed this problem by finely binning the absorption lengths in RAT derived from the SNOMAN values. The SNOMAN values are verified by the SNO group.

The RAT-Initial to SNOMAN comparison following the physics list and attenuation changes to RAT-Initial is shown in figure 5.6. These changes have improved the Nhit comparison, reducing the RAT-Initial Nhit mean. However, no improvement is seen in the PMT and concentrator reflection peaks.

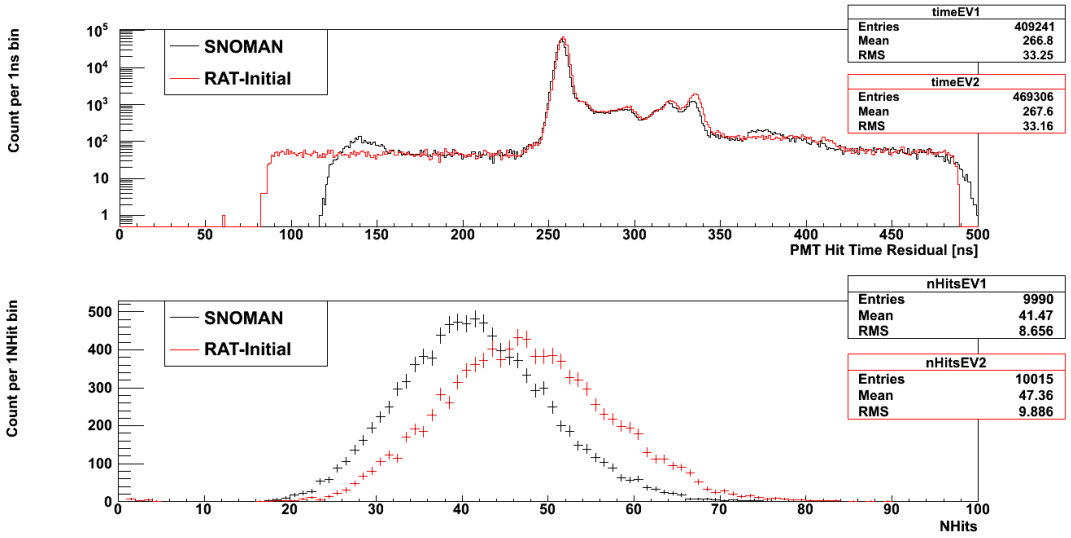

Figure 5.6: Timing and Nhit comparison between SNOMAN and RAT-Initial post the physics list and attenuation changes. Discussion in main text.

5.4 PMT Simulation

The RAT-Initial Monte Carlo uses the GLG4 PMT optical model and the RAT-Initial PMT geometric definitions. Neither of these definitions match those used in SNOMAN, and thus are likely to give the distorted PMT and concentrator reflection peaks seen in figures 5.6 and 5.2. Therefore I ported the SNOMAN PMT geometry and optical model into RAT-Initial to continue the comparison.

5.4.1 Concentrator Overlap Problem

The comparison of RAT-SNOMAN with SNOMAN reveals the PMT and concentrator reflections to have merged. This is clearly seen in figure 5.7 in the timing plot between 320ns and 340ns. This feature was also seen in plots produced with early versions of the SNOMAN Monte Carlo.

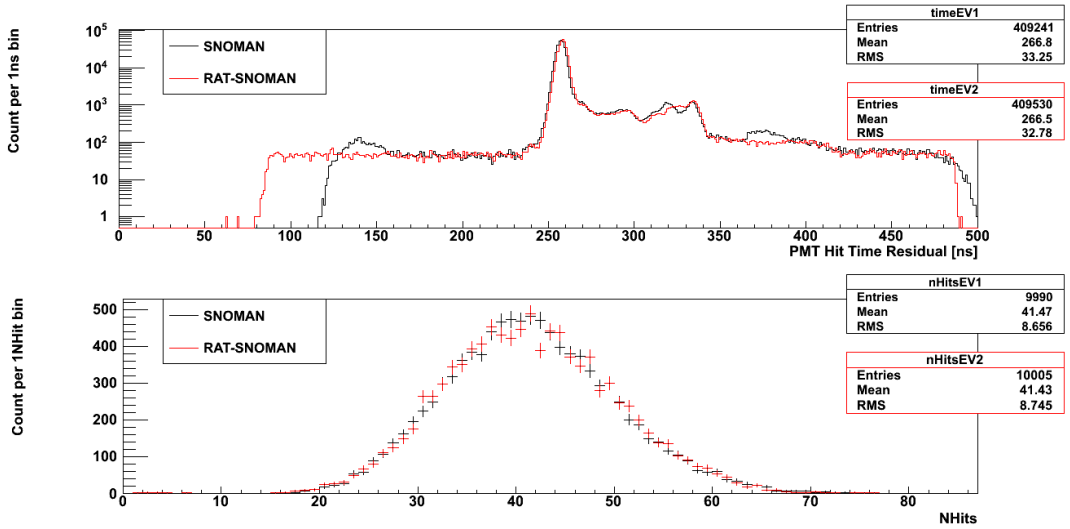

Figure 5.7: Timing and Nhit comparison between SNOMAN and RAT-SNOMAN with the concentrator overlap problem. Discussion in main text.

The merged reflection peaks occur when the concentrator geometry overlaps the PMT geometry i.e. in the Monte Carlo the two geometric definitions occupy the same physical space. The concentrator geometry will overlap the PMT geometry if the concentrator is not placed far enough away from the PMT surface. This offset is defined by the inner radius of the base of the concentrator and the PMT surface. Hence if a larger inner radius is used by mistake, the concentrator will have a smaller offset and thus overlap. A larger radius will be calculated if the SNO concentrator locus definition is used, see section 3.2.2.

I solved this tracking problem by ignoring the concentrator geometry which overlaps the PMT geometry. This is the solution adopted by the latter versions of SNOMAN against which all comparisons are made.

5.4.2 PMT angular response comparison

To ensure the PMT geometry and model in RAT-SNOMAN reproduce SNOMAN, I have extracted the PMT angular response. The PMT angular response is the ratio of photons causing signals to photons hitting the PMT as a function of incident angle to the PMT axis. This comparison is shown in figure 5.8.

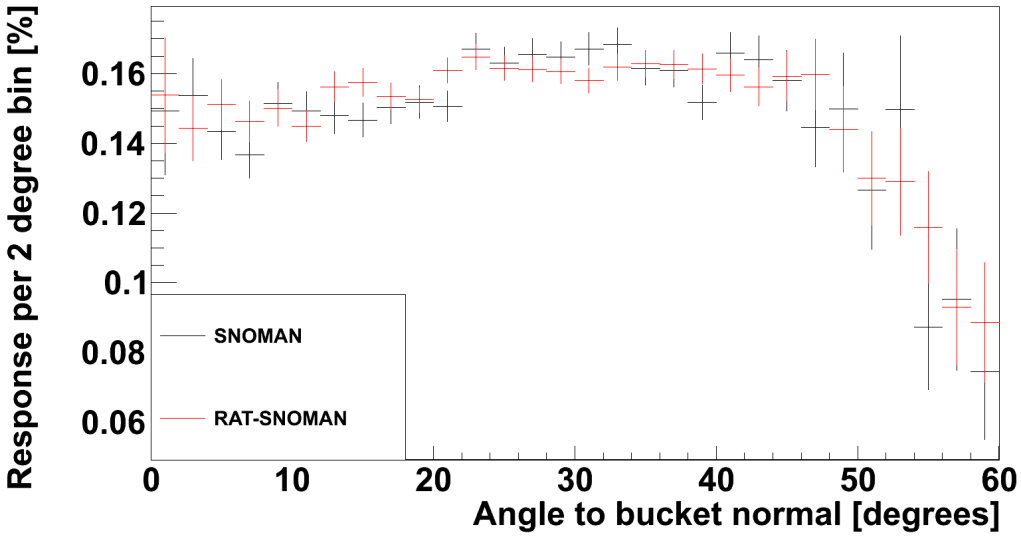

Figure 5.8: Comparison of the PMT angular response illuminated by 420nm incident photons between SNOMAN and RAT-SNOMAN. The ROOT Chi2Test given p value is 0.77, $\chi^2/ndf = 23.225309/29$.

The agreement between RAT-SNOMAN and SNOMAN seen in figure 5.8 is good considering the problems in extracting the response. These problems are a result of the inherent differences between RAT and SNOMAN and are in general very small effects. For example, the water within the concentrator attenuates in RAT but not in SNOMAN, this may cause a small difference in the response.

In summary the RAT-SNOMAN PMT model and geometry can now be considered to reproduce SNOMAN. This removes the PMT model and geometry from the aspects of the Monte Carlo that are unverified.

5.5 RAT-SNOMAN to SNOMAN comparison

The comparison of RAT-SNOMAN including the concentrator overlap fix with SNOMAN is shown in figure 5.9. A good agreement is seen in the PMT hit time comparison, especially the peak relative size and time. However, RAT-SNOMAN is consistently late relative to SNOMAN by $\approx$ 1ns. This disagreement cannot be explained at this stage. Further good agreement is seen in the Nhit comparison.

The features seen in the SNOMAN PMT hit time plot at 140ns and 375ns are believed to be due to bugs in SNOMAN. At 140ns the only registered hits should be PMT noise which should be flat as in RAT-SNOMAN.

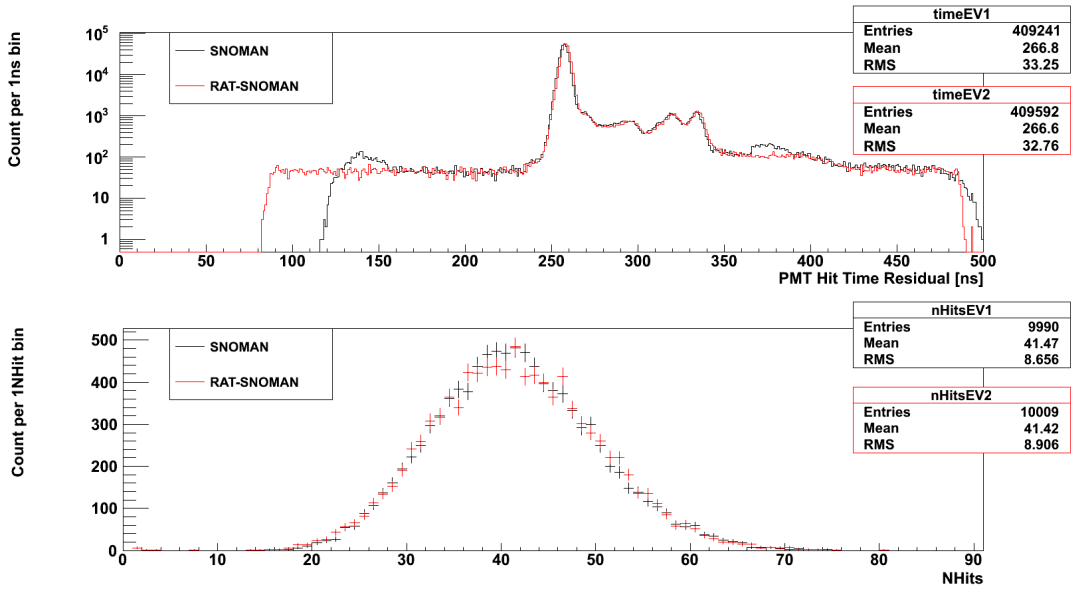

Figure 5.9: Timing and Nhit comparison between SNOMAN and RAT-SNOMAN. Discussion in main text.

5.6 New PMT Simulation

As detailed in the previous two chapters, I have changed many small aspects of the PMT model and geometry. These changes are not expected to cause large difference in the PMT hit time or Nhit comparison. The comparison between RAT and SNOMAN is shown in figure 5.10, and does not show any large differences.

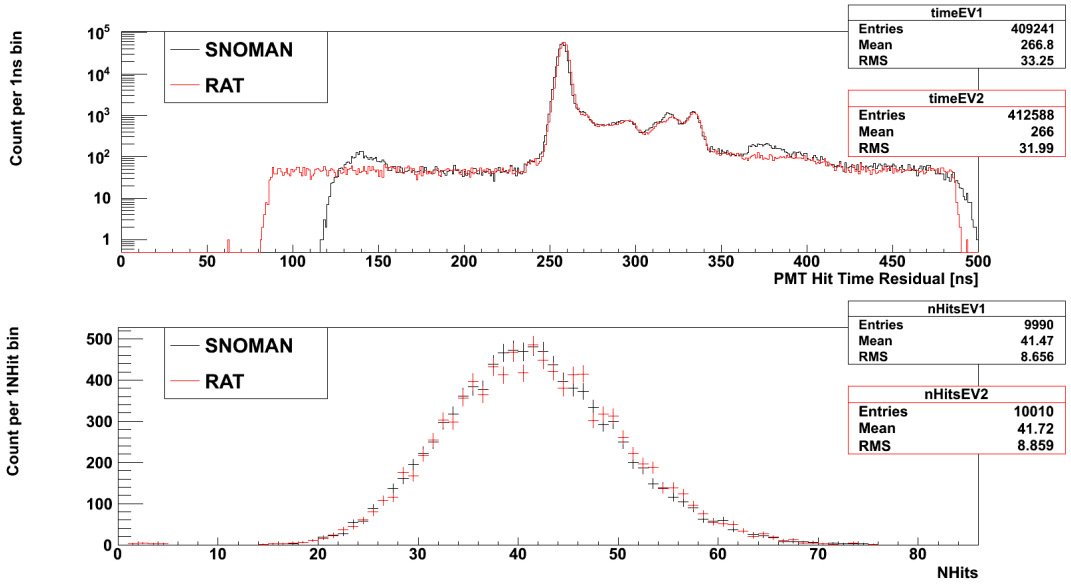

Figure 5.10: Timing and Nhit comparison between SNOMAN and RAT. Discussion in main text.

5.7 *In-situ* Verification

The ultimate verification of RAT will be against SNO+ data, especially SNO+ scintillator data. Tools and experience from the SNO experiment exist and enable the photon transport properties to be determined. These tools will be complimented with the SMELLIE analysis, allowing the scattering to be determined. This allows the response of the PMT plus concentrator to be deconvolved from the photon transport and source, leaving the pure PMT plus concentrator response. This is an important measurement, as due to concentrator ageing it will change with time.

5.7.1 Ageing

The concentrator ageing will be an important quantity to model during SNO+, as it was during SNO. This ageing is known to change the angular response of the PMT plus concentrator and the overall Nhit. However, previously in SNO it was not possible to tell if the ageing was a PMT or concentrator effect.

For SNO+ I have proposed replacing some of the existing concentrators with black concentrators. These black concentrators will ideally be the same shape but have very low reflectivity. This can be achieved by removing the petals from existing concentrators thus leaving the black plastic surface. The PMT plus black concentrator angular response will thus be a function of the PMT alone, and hence any changes with time will suggest PMT ageing. Furthermore if the PMT does not age, the angular response of the PMT plus concentrator can be normalised against the PMT plus black concentrator response, thus showing only the concentrator response.

I have also proposed adding some new, not aged in the detector, concentrators. This is required as the *ex-situ* model has never reproduced the measured angular response in the detector. I believe this is due to ageing between installation and the first angular response measurement. Hence, the addition of new concentrators and an early angular response measurement will help reconcile this problem. Furthermore, it will allow the rate of ageing in SNO+ to be compared to SNO.

These additional concentrator changes are now part of the SNO+ detector work schedule, and will hopefully allow the ageing to be fully understood and modelled in SNO+.

5.8 Conclusion

The changes outlined in this chapter have shown that the SNO+ Monte Carlo reproduces the observable results of SNOMAN and therefore SNO. This verifies the large aspects of the Monte Carlo, including my work on the PMTs, Čerenkov physics and photon transportation. With the further aspects of RAT verified by the SNO+ Collaboration, RAT can now be used to simulate the SNO+ detector and experimental backgrounds.

Chapter 6

Event Reconstruction

The Reconstruction code structure is presented and compared with the previous structure. Position reconstruction algorithms are discussed, and used to improve the energy reconstruction algorithm, which is also described.

The sensitivity of the SNO+ experiment to double beta decay is dependent on the energy resolution, with better energy resolution giving a better limit. Furthermore, the ability to identify events as potential backgrounds based on the event position will improve the sensitivity by reducing backgrounds. Therefore it is clear that the event position and energy must be reconstructed very well.

The expected vertex position resolution can be approximated by assuming that the reconstruction algorithm is trying to fit the peak of a Gaussian. The error in this evaluation will then be $\delta t = \sigma/\sqrt{N}$. For the scintillator $\sigma \approx 40[ns]/(2\sqrt{2\log 2}) \approx 16.9$ns, with the FWHM value of 40ns taken from figure 6.3. At 3MeV $N \approx 1200$ thus $\delta t \approx 0.5$. This translates to a distance of $\delta t \cdot c/1.5 \approx 100$mm.

The expected energy resolution can be approximated by noting that there are approximately 400 hits, N_{MeV}, per MeV event energy. Hence, assuming a Gaussian resolution distribution given the large number of Poisson distributed photons, the resolution in hits should ideally be equal to $\sqrt{N}$. Therefore the resolution in

energy, σ, at 3.5MeV should be

$$\sigma = \frac{\sqrt{400\text{MeV}^{-1} \cdot 3.5\text{MeV}}}{400\text{MeV}^{-1}} = 0.094\text{MeV} \tag{6.1}$$

Furthermore $\frac{\sigma}{\sqrt{E}}$ should ideally be independent of energy.

6.1 Events in SNO+

Events in SNO+ are defined by the trigger system, with a single event for every crossing of the analogue trigger threshold. The trigger threshold will vary depending on the experimental phase, and for the scintillator phase the threshold is likely to be 100 PMT hits within 100ns. These PMT hits are caused by scintillation or Čerenkov photons from within the PSUP volume, which themselves are produced by charged particle interactions, or noise.

A typical chronological sequence for a SNO+ signal event starts with a decay within the acrylic vessel in the scintillator. The resultant charged particle from the decay will interact with the scintillator which in turn emits scintillation photons. These photons then traverse the detector to the PMTs, finally being absorbed and detected at the PMT. These PMT hit signals are summed and activate the trigger (the trigger latches). All PMT hits 180ns before the trigger latches and 220ns after the trigger latches are then saved for analysis.

The trigger system will latch given enough PMT hits regardless of the type of interaction and number of charge particles. Hence an event in SNO+ is not necessarily a single interaction or single decay, i.e. events do not define the underlying process. Therefore events are equivalently defined for signal and background underlying processes. The event reconstruction algorithms discussed assume a single decay causes the event. For events caused by multiple decays or crossings see the pileup chapter 8. Events can also be caused by charged particles, muons, crossing

the detector; these are not reconstructed by the algorithms presented[1].

6.1.1 Event Timing

The timing system for PMT hits within an event is also defined by the trigger. Hence there are two timing systems: in the pre-trigger timing system PMT hit times are absolute times; in the post-trigger timing system PMT hit times are relative to the trigger. The post-trigger timing system is the timing system of the detector output and thus is used in the reconstruction algorithms. The relationship between the two systems is best described by considering the trigger chronology given a special event such as in figure 6.1. This chapter refers to timing in the post-trigger system only.

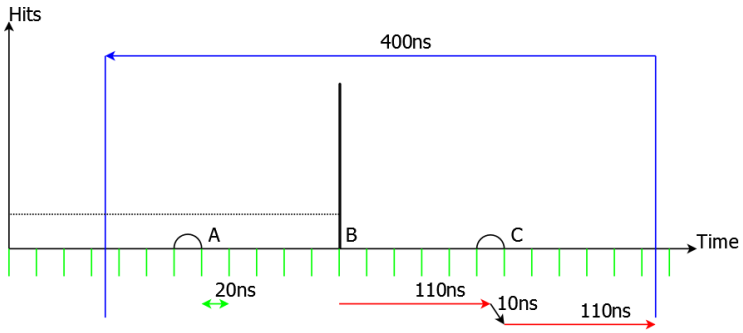

Figure 6.1: Pre trigger event timing for contrived hit pattern. Trigger signal delay times shown in red (from PMT to trigger system then back), 50MHz clock shown in green (20ns between ticks), trigger threshold height is shown by the dotted black line, event window shown in blue. Chronology discussed in main text.

Consider enough PMT hits occurring at time B in figure 6.1 such that the number of hits is above the trigger threshold dotted line. As the PMT crosses its local threshold the PMT time to analogue converter (TAC) starts to ramp (count) whilst simultaneously sending a signal to the trigger system. This trigger signal takes 110ns to reach the trigger system, as shown by the first red line. If enough hit signals are present in the trigger system the trigger will latch to the

[1]These are very small rate backgrounds that are easily identifiable. See the backgrounds chapter 7.

next 50MHz clock, clock ticks shown in green. Hence the trigger system waits 10ns before latching in this example otherwise a maximum 20ns delay may occur. A trigger latched signal will then return to the PMTICs, front end electronics, this again takes 110ns (second red line) hence a minimum 220ns must pass following the PMT hit. The trigger latched signal is received at the PMT resulting in all TAC values from the previous 400ns to be saved into the event data.

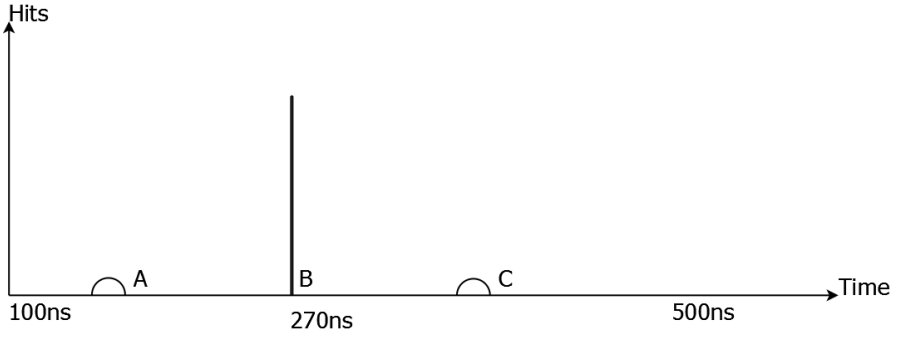

Figure 6.2: Post Trigger event timing for the contrived hit pattern given in figure 6.1. Note the full trigger window is between 100ns and 500ns in this system.

The raw TAC values for each PMT hit must now be converted to the post trigger timing system. Each TAC value corresponds to the length of time between the hit and the arrival of the trigger latching signal at the PMT, e.g. C will have TAC values of 120ns ± 10ns. The hit time in the post trigger system is then 500ns [2] minus the TAC time, hence C is at 380ns ± 10ns as shown in figure 6.2. Note the trigger window is limited to 400ns in length, i.e. TAC values above this are ignored/reset.

The true decay time B in figure 6.1 is independent of the 50MHz clock system. Therefore if the decay occurred 10ns later or earlier the trigger would latch instantly and B would be positioned 10ns later in figure 6.2. Whereas if the decay occurred 5ns earlier B would be positioned 5ns earlier in figure 6.2. This [0, 20)ns trigger latching delay differs from event to event, and is unknown. However the PMT hit times are known relative to the latched time, and thus the SNO+ timing

[2] 500ns is chosen to be sufficiently large number to ensure all times are positive.

system.

6.1.2 Single Interaction Event Properties

The reconstruction algorithms described reconstruct events dominated by either scintillation or Čerenkov, i.e. work only in the scintillator or water SNO+ experimental phases. For example decays in the scintillator will be dominated by scintillation as there are approximately two orders of magnitude more scintillation photons than Čerenkov photons. Furthermore a fraction of the Čerenkov photons will be absorbed and re-emitted, replacing the Čerenkov properties with scintillator properties. Whereas, decays in water cannot produce scintillation photons and are thus dominated by Čerenkov.

Decays in the water volume producing charged particles above the Čerenkov threshold will result in Čerenkov photon emission. These photons are emitted promptly at the Čerenkov angle to the particle momentum. Hence the PMT hit pattern is anisotropic and the hit times corrected for transit are strongly peaked.

Decays in the scintillator volume will produce scintillation photons and, if above the Čerenkov threshold, Čerenkov photons. These photons can then be absorbed, re-emitted or scattered in the scintillator. The emission and re-emission of the scintillator photons is isotropic and hence the PMT hit pattern is isotropic (relative to the event position). Furthermore the scintillator emission and re-emission has a distinct time profile, which is specific to the scintillator and particle type[3].

The scintillator emission time profile is characterised by a sum of decaying exponentials[70]:

$$P(t) = \sum_{i}^{N} \frac{a_i}{\tau_i} \exp \frac{-t}{\tau_i} \tag{6.2}$$

The probability, P(t), of a photon emission at time t (relative to an origin at $t = 0$)

[3]The time profile is dependent on the dE/dx value, which varies with particle type.

Component, i	a_i [%]	τ_i [ns]
1	71	4.6
2	22	18
3	7	156

Table 6.1: Scintillator timing components for deoxygenated LAB + 2g/L PPO excited by electrons[70]

is given by the sum of N decaying exponentials with decay constant τ_i and fraction (of the sum) a_i. These decay constants and fractions have been measured for the LAB + 2g/L PPO mixture to be used, and are listed in table 6.1.

The light yield for the LAB + 2g/L PPO mixture has also been measured and found to be 1×10^4 photons per MeV [52]. This yield is approximately linear with energy in the SNO+ energy domain.

6.1.3 Decays in the Scintillator within 600mm of the AV

The scintillator volume has a refractive index comparable to the AV and much higher than the water volume. This leads to a critical angle of total internal reflection for photons traversing from the scintillator through the AV to the water. Due to the spherical geometry of the SNO+ detector, total internal reflection is only possible for photons emitted within a distance x_{max} from the acrylic vessel emitted within a set angular range[4]. The distance x_{max} is given by equation 6.4 as derived in [71], for 400nm photons $x_{max} = 623$mm from the AV.

$$x_{max} = r_{av} * \left(1 - \frac{n_{lightwater}(\lambda)}{n_{scintillator}(\lambda)}\right) \quad (6.3)$$

$$= 6005.4\text{mm} * (1 - \frac{1.34423}{1.50}) \quad (6.4)$$

$$= 623\text{mm} \quad (6.5)$$

[4]The angular range is relative to the event axis, vector from detector centre to event.

This total internal reflection region, the near AV region, constitutes 28% of the total volume of the scintillator.

The angular region of total internal reflection, TIR, increases as the distance to the AV decreases, this is shown in figure 5 of [71]. Hence a spherical section of the PSUP will be devoid of prompt hits, although scattered and re-emitted light may still cause hits in this region. The hit times are related to the hit positions by the group velocity and decay position; hence this spatial TIR region corresponds to a timing region with less hits. This region devoid of hits is present in the raw hit times before transit correction.

6.2 Fitter code improvements

RAT-Initial had four independent position reconstruction fitters and two independent energy reconstruction fitters. These fitters had a great deal of shared code and assumptions about the event. However none of these fitters could work together; for example the energy reconstruction fitters were tied to a certain position reconstruction fitter. Furthermore the fitters assumed the fixed parameters for LAB PPO scintillator with no easy way of changing these parameters based on the SNO+ experimental phase. This is not a satisfactory solution for SNO+ as more flexibility will be required, e.g. allowing different experimental phases.

Two independent solutions were proposed by S Biller and A Mastbaum, both of which standardise the fitter output and split the fitter into constituent parts. I then developed these solutions with input from S Biller *et al.*, into the solution given below which I added to RAT to be used in SNO+.

Firstly the fitter code is improved by standardising the output, as this allows one fitter to seed another and allows analysis scripts to be fitter independent. A single interaction event in SNO+ can be characterised and reconstructed as a vertex, hence the fitter code outputs a collection of these vertices. Furthermore

Property	Data type	Comment
Position	TVector3	Position of the vertex [mm]
Position Error	TVector3	Errors on the reconstructed position [mm]
Direction	TVector3	Direction of the particle [a.u.]
Direction Error	TVector3	Errors on the reconstructed direction [mm]
Time	Double	Time of the decay [ns]
Time Error	Double	Error on the reconstructed time [ns]
Energy	Double	Energy of the particle [MeV]
Energy Error	Double	Error on the reconstructed energy [MeV]
Particle Type	Int	Particle type id [PDG Monte Carlo ID]

Table 6.2: List and details of the standardised SNO+ fitter output.

each vertex is characterised by the position, time, direction, energy and particle type, which form the output for each vetex. However not all fitters reconstruct all of these properties, therefore the code will not return data for unreconstructed properties[5]. This output structure is used by all SNO+ fitters as detailed in table 6.2.

Secondly the fitter code is improved by splitting the fitters into the following sub-components:

- Method. A method is the fitter algorithm and defines what properties of the vertex are reconstructed.
- Optimiser. An optimiser calls the method many times whilst altering a proposed vertex until a best fit is found.
- PDF. A PDF is an object that returns a probability of observing a PMT hit given a proposed vertex.
- PMT Selector. A PMT selector chooses PMTs based on some criteria e.g. a prompt timing window.

[5]This prevents fake data being analysed as the code will crash if the user insists on analysing unreconstructed properties.

- Transit time calculator. Calculates the distance and time required for photons to traverse from the vertex to the PMT.

Therefore a fitter is now a combination of a method with any or none of the extra components. These sub-components are written to be shared such that a fitter can be a combination of any components.

6.3 Near AV Fitter

The near AV fitter consists of the near AV method and no extra sub components. This fitter is designed to identify and reconstruct an event's position and time, for interactions in the near AV region. This fitter makes extensive use of the special event properties when an interaction occurs in the near AV region, see section 6.1.3. The identification algorithm is based on work by S Morgan[71] whilst I developed the position and time reconstruction algorithm.

As stated in section 6.1.3 interactions near the AV have a spatial and timing region of reduced hits. These regions are fully defined by the interaction's time and distance to the acrylic vessel. Figure 6.3 shows the summed timing of 500 electron events corrected for the trigger latching delay.

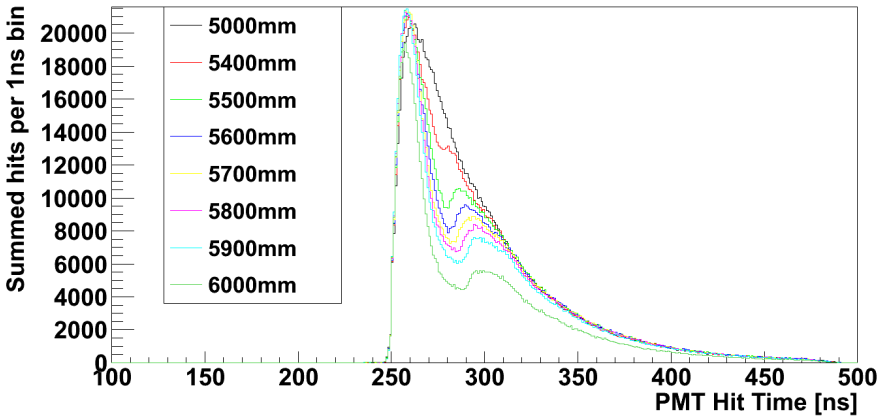

Figure 6.3: Summed raw timing spectra for 500 decay electrons at varying positions from the detector centre.

Following the work of S Morgan a ratio, r can be defined as the number of hits in a window [t_s, t_e] relative to the first hit time t_f over the total number of hits. If the r drops below a safe limit, s the event can be identified as near the AV. The ratio will decrease linearly as the distance from the detector centre increases.

The position of the decay can be split into two aspects, the distance from the detector centre and the direction to the interaction relative to the detector coordinate system. The distance from the detector centre, d is given by[6]:

$$d = 6005.4\text{mm} - m \cdot r - e \tag{6.6}$$

where r is the ratio, m is the fitted ratio gradient [mm], e is the fitted ratio intercept [mm], and 6005.4mm is the AV inner radius. The first PMTs to be hit will be those nearest to the interaction position. Hence ideally the first hit PMT (at time t_f) will have the same direction in the detector coordinate system as the interaction. However this is not necessarily the case, therefore a weighted sum of the PMT hits in the first 10ns is calculated to give the decay direction, $\vec{e}$:

$$\vec{e'} = \sum_i P_i \cdot w_i \tag{6.7}$$

$$w_i = \frac{1}{t_i - t_f} \tag{6.8}$$

$$\vec{e} = \frac{\vec{e'}}{\mid e' \mid} \tag{6.9}$$

where t_i is the PMT hit time and P_i is the PMT hit position. The reconstructed event position is $\vec{v} = \vec{e} \cdot d$.

The reconstructed event time, t_0 is then calculated by $t_0 = t_f - T(\vec{v}, PSUP)$, where $T(\vec{v}, PSUP)$ is the transit time from position $\vec{v}$ to the nearest PSUP point. This transit time calculation is detailed in section 6.4.

The numerical values for t_s, t_e, s, m, e are obtained by an automated fit coor-

[6]6005.4mm is the inner radius of the AV.

Parameter	Value	Comment
t_s	16ns	Window start, relative to first hit time.
t_e	56ns	Window end, relative to the first hit time.
m	-5531.12 mm	Position to ratio gradient.
c	7802.48 mm	Intercept.
s	0.42	Safe ratio value, 3 sigma below mean value.

Table 6.3: List and details of the standardised SNO+ fitter output.

dinator script via the following process. Electron events are simulated at 100mm intervals from 5400mm to 6000mm from the detector centre. The script then tests many possible values of t_s, t_e, choosing the values which minimise the r divided by position gradient, i.e. chooses the window with the largest difference in r at 5400mm and r at 6000mm. The gradient of r divided by position is then inverted to give m and then used to solve for e (linear fit). Finally electron events are simulated at 5000mm (away from the AV) and r is calculated for each event given t_s, t_e. A Gaussian is fitted to the histogram of r values, with s chosen to be three sigma below the mean. This should result in a less than 1% of events being falsely identified. The values derived from the Monte Carlo are given in table 6.3.

6.4 Transit calculation

The distance traversed and time taken for a photon to travel from a position within the PSUP to a PMT is a vital calculation in most reconstruction algorithms. This is not a simple calculation as SNO+ contains multiple dispersive media. However the calculation must be quick, as given the number of hits and trial positions required to reconstruct an event more than $1 * 10^6$ calls per event can be expected. The transit calculations are designed around a trade off between accuracy and execution speed. With this in mind I have developed one distance calculating algorithm and two time calculating algorithms.

6.4.1 Distance calculation

The simplest and quickest distance calculation is to assume the photon travels in a straight line through three spherical media. The media are; the AV contents, the AV itself with radii 6005.3mm and 6060.4mm respectively, and the water region containing the PMTs which surrounds the AV. Given an event position $\vec{v}$ and a PMT position $\vec{P}_i$ the transit distance $d(R_{sphere})$ in a sphere of radius R_{sphere} is given by:

$$\vec{u} = \frac{\vec{P}_i - \vec{v}}{\mid \vec{P}_i - \vec{v} \mid} \tag{6.10}$$

$$\alpha_{\pm} = -\vec{u} \cdot \vec{v} \pm \sqrt{R^2_{sphere} + (\vec{u} \cdot \vec{v})^2 - \vec{v}^2} \tag{6.11}$$

$$\tag{6.12}$$

If $R^2_{sphere} + (\vec{u} \cdot \vec{v})^2 - \vec{v}^2 < 0$ then $d(R_{sphere}) = 0$, i.e. the photon does not transit inside the sphere.

If the event position is inside the sphere i.e. $\mid \vec{v} \mid < R_{sphere}$:

$$d(R_{sphere}) = \begin{cases} \alpha_+ & \text{if } \alpha_+ > 0 \\ \alpha_- & \text{if } \alpha_- > 0 \end{cases} \tag{6.13}$$

If the event position is outside the sphere i.e. $\mid \vec{v} \mid > R_{sphere}$:

$$d(R_{sphere}) = \begin{cases} \alpha_+ - \alpha_- & \text{if } \alpha_+ > \alpha_- > 0 \\ \alpha_- - \alpha_+ & \text{if } \alpha_- > \alpha_+ > 0 \end{cases} \tag{6.14}$$

The distance in each media is then:

$$d_{scintillator} = d(R_{Scintillator}) \tag{6.15}$$

$$d_{AV} = d(R_{AV}) - d_{Scintillator} \tag{6.16}$$

$$d_{water} = \mid \vec{P_i} - \vec{v} \mid -d_{AV} - d_{scintillator} \tag{6.17}$$

The simple calculation given above ignores any effect of refraction at the media boundaries. This inaccuracy will be larger in the scintillator phase and will increase as the event position from the detector centre increases, as more events will exit the AV at higher angles leading to more refraction. A full ray-traced distance calculation including refraction effects, takes much more computation to calculate. Given the number of photon tracks that must be calculated this severely extends the reconstruction computation time, rendering it impossible to reconstruct events in less than a second. Henceforth, only the simple straight line calculation will be used.

6.4.2 Time calculation

The transit time in each media can be calculated using the known group velocity for the media. As the media are dispersive the group velocities are not constant over the wavelength domain that the PMTs respond to. Furthermore the wavelength of the photon that caused the hit cannot be deduced from the data. Hence, a representative wavelength must be chosen.

The chosen wavelength to evaluate the group velocity will thus change the transit time. Therefore I have chosen to use the wavelength that causes the most PMT hits. This value changes depending upon the SNO+ experimental phase as shown in figure 6.4, and is 370nm for the water phase and 400nm for the scintillator phase.

Whilst the group velocity transit time calculation outlined above works well for

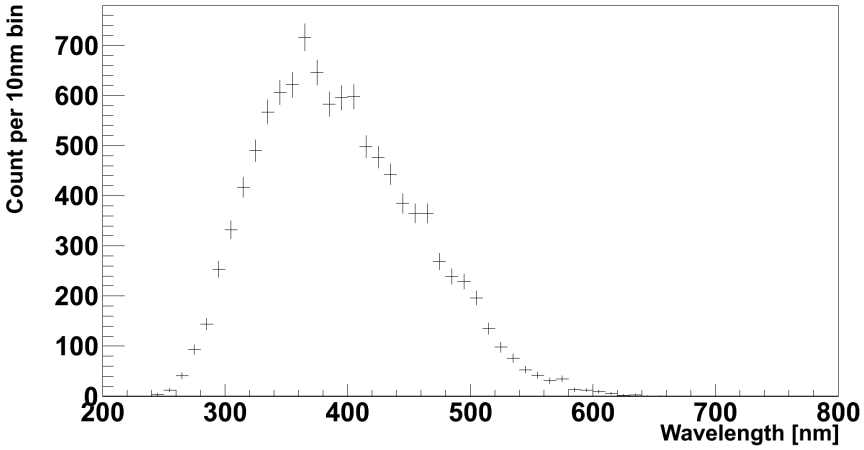

(a) Water phase hit distribution

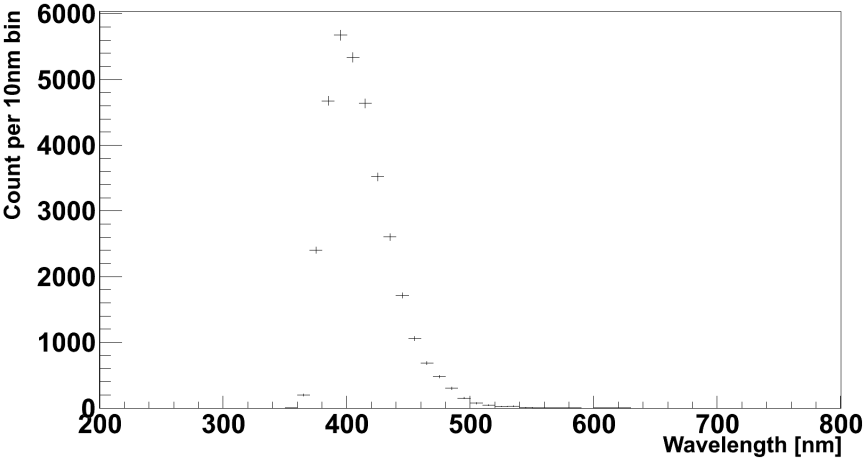

(b) Scintillator phase hit distribution

Figure 6.4: Wavelength distribution for photons causing PMT hits simulated in the water and scintillator SNO+ phases.

the water phase, it is flawed in the scintillator phase. This is because the photons are absorbed and re-emitted in the scintillator changing in wavelength and hence velocity. Therefore the transit velocity is no longer the group velocity of the most prominent hit photon wavelength. Instead an effective transit velocity must be calculated for photons in the scintillator.

I will define the effective transit velocity as the net velocity for photons emitted promptly then absorbed and re-emitted promptly. Hence the effective velocity will depend on the emission wavelength, absorption wavelength profile, the re-emission

wavelength and the PMT wavelength sensitivity. For example consider a photon emitted at wavelength w that travels a distance x_1 in t_1 before being absorbed and re-emitted at wavelength u travelling x_2 in t_2, giving an effective velocity of $v = \frac{x_1+x_2}{t_1+t_2}$.

I calculate the effective velocity by simulating electron events at set distances from the detector centre, with the scintillator emission and re-emission time profiles set to a delta peak at zero. This alteration to the time profiles removes the complication of later emission times distorting the $t_{1,2}$ values. These time profiles will later be incorporated into a probability density function (PDF). Considering only the hit PMTs within 10° of the event position allows the transit distances in each medium to be calculated accurately using the straight line path algorithm. Removing the transit time in the water and AV as calculated by the group velocity algorithm leaves the transit time in the scintillator. Plotting the transit time in the scintillator versus the transit distance in the scintillator gives figure 6.5.

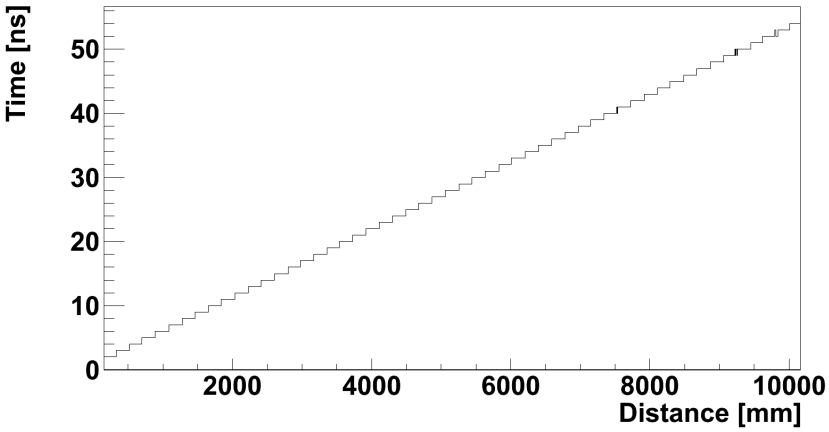

Figure 6.5: Effective transit time versus distance in scintillator. Technique described in main text.

The transit time in the scintillator is expected to have a quadratic relationship to the transit distance. This is seen in KamLAND[72] and is due to the increasing fraction of absorbed and re-emitted light as the distance increases. The polynomial fit to figure 6.5 is:

$$t = 0.32\text{ns} + 5.52530 * 10^{-3}\frac{\text{ns}}{\text{mm}}\ x - 2.47741 * 10^{-8}\frac{ns}{\text{mm}^2}\ x^2 \tag{6.18}$$

where x is in mm. As the quadratic term is so weak the effective velocity is taken as a constant 180.99mm/ns. This implies that most of the absorption and re-emission takes place over a very short distance.

6.5 Maximum Likelihood Methods

Maximum likelihood estimation is the best way to estimate the parameters of a model. It works by maximising the product of probabilities, the likelihood function (L), for a set of parameters given a model. This is particularly useful to event reconstruction as the parameters defining the decay vertex need estimating. The likelihood function is given by:

$$L = \Pi_{i=1}^{N} P(h_i, \vec{\beta}) \tag{6.19}$$

Where i runs over the observed h_i values, $\vec{\beta}$ is the parameters and $P(h_i, \vec{\beta})$ is the probability of the observed h_i given the parameters.

The likelihood function for the position and time reconstruction algorithms consist of the product of hit probabilities. The hit probability is the probability of the observed hit PMT being hit given the proposed event position and time. Hence the position and time parameters are estimated by maximum likelihood estimation.

During the maximisation the values obtained for the likelihood function will lose precision. Therefore it is more precise and convenient to define the log likelihood function ($\mathcal{L}$) and minimise the -$\mathcal{L}$ value.

$$\mathcal{L} = \sum_{i=1}^{N} \log P(h_i, \vec{\beta}) \tag{6.20}$$

The minimisation of -$\mathcal{L}$ is done by the MINUIT[73] package developed at CERN.

6.5.1 Probability density functions

A probability density function (PDF) $P(h_i, \vec{\beta})$ must be defined for the maximum likelihood estimation to work. I have developed two PDFs for the scintillator phase which can be used to reconstruct the event position and time. These PDFs return a probability for a given PMT to be hit given a proposed position and time.

The simplest PDF is to assume that the photons are emitted according to the scintillator emission time profile as defined in table 6.1. This sum of exponential decays convoluted with the PMT transit time spread (TTS) gives the PDF shown in figure 6.6(b). This PDF will be referred to as the simpleTiming PDF henceforth.

The simpleTiming PDF is a function of emission time alone, and hence the proposed position and time for a given PMT hit must be converted into an emission time. This conversion is done using the straight-line path and group velocity algorithms.

The simpleTiming PDF neglects the effect of absorption and re-emission of photons. These re-emitted photons will usually arrive at the PMTs later than the primary emitted photons. Furthermore the single primary absorbed photon may cause multiple photon re-emission. This has the effect of increasing the apparent late emission.

To take account of the re-emission I constructed a PDF as a histogram of simulated emission times for all photons as in figure 6.6(b). This is not an ideal solution as it will count the primary emission and then the re-emission of the same photon. However, as seen in the next section, it reconstructs the position and time

well, indicating that the double counting is a small effect. The conversion from a given PMT hit and proposed position and time to an emission time is calculated using the straight path and effective velocity algorithms. This PDF will be referred to as the emissionTime PDF henceforth.

The previous two PDFs work solely for the scintillator phase, although the latter can be reconfigured for any phase. For the water phase I have ported the PDF developed by M Boulay[74] shown in figure 6.6(a). The M Boulay water PDF was used for the in the SNO analysis of data.

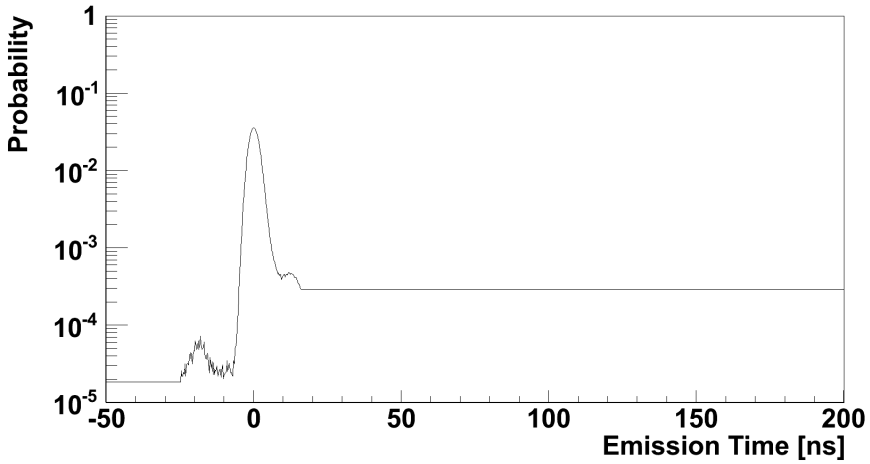

(a) Water phase PDF as developed by M Boulay[74].

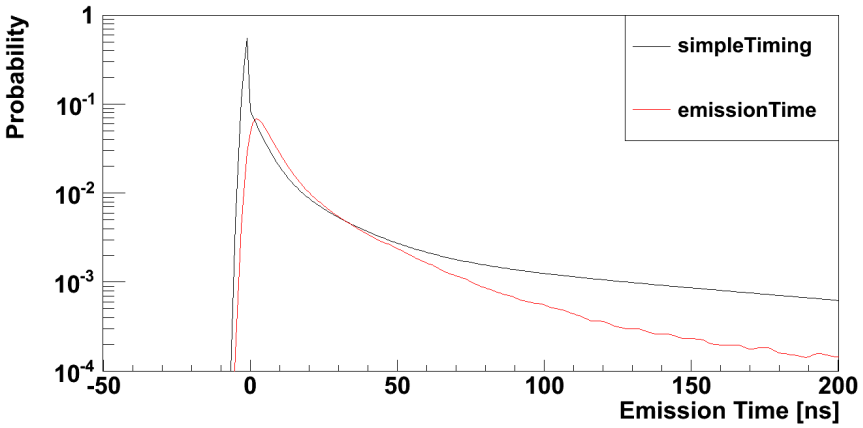

(b) Scintillator phase PDFs

Figure 6.6: Position and time reconstruction PDFs for the water and scintillator phases of SNO+.

6.6 Position Reconstruction Performance

The reconstruction algorithms are defined by their performance in reconstructing known events. This performance is characterised by the validity, bias and resolution of the fitter output. The validity is defined as the percentage number of events that are successfully reconstructed. The bias and resolution are extracted from a Gaussian fit of the fitted to known parameter output, e.g. fitted minus known radial position. From the Gaussian fit the mean is the bias and sigma the resolution.

The performance is further characterised as a function of radial position and separately as a function of energy, with the position resolution stated in terms of the detector Cartesian co-ordinate system and as a quadrature addition of the three components. The position bias, given the spherical symmetry of the SNO+ detector, is expected only to exist in the radial direction if at all. However, noting the neck breaks this symmetry, a position bias may exist along the z axis. Therefore the bias is stated in the radial and Cartesian z co-ordinates.

6.6.1 NearAV Performance

The nearAV fitter should only be valid in the near AV region i.e. it should not return fitted values for any other region. The validity is found to be less than 1% for radii less than 5400mm, and 100% for radii above 5700mm, as expected. Just inside the near AV region at 5500mm the nearAV fitter has 70% validity. The resolution and bias are shown in figures 6.7 and 6.8 respectively.

6.6.2 Likelihood Performance

The maximum likelihood method as maximised by MINUIT can be combined with the simpleTiming or emissionTime PDF. The emissionTime PDF leads to significantly improved performance over the simpleTiming PDF. Hence only a

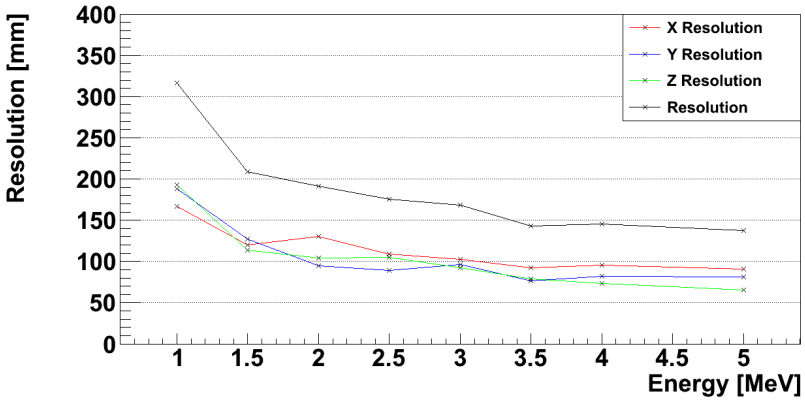

(a) Resolution versus energy. The resolution drops with energy as the number of hits increase.

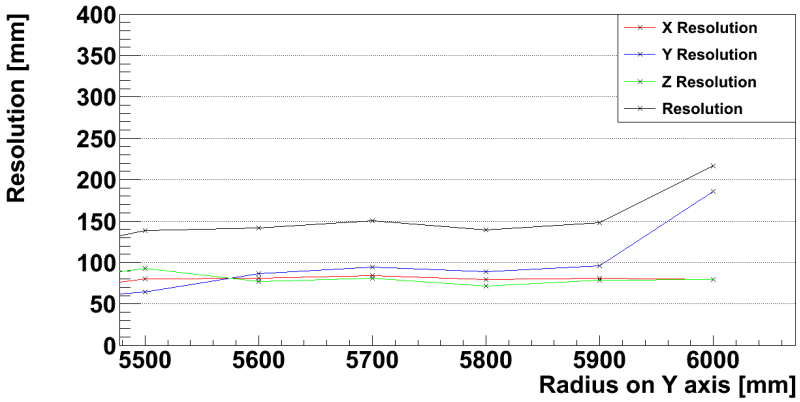

(b) Resolution versus position. The resolution is fairly constant at 150mm except at 6000mm. As the NearAV fitter ensures fitted positions are within 6060mm (AV radius) the resolution is hard to define at this position.

Figure 6.7: NearAV, resolution as a function of energy and a function of position.

summary of the simpleTiming PDF performance is given, rather than full details.

The simpleTiming PDF combination gives a resolution of ≈ 200mm at 3MeV with a validity in the mid 50%. This is a good for a first attempt position fitter however it is too poor for the SNO+ experiment. The very low validity significantly impacts the sensitivity by reducing the signal efficiency.

The emissionTime PDF combination gives much better results, with resolution of 150mm at 3MeV and a validity greater than 90%. The resolution is detailed in figure 6.9, and bias in figure 6.10.

The emissionTime PDF reconstructs the event time as well. This shows a bias

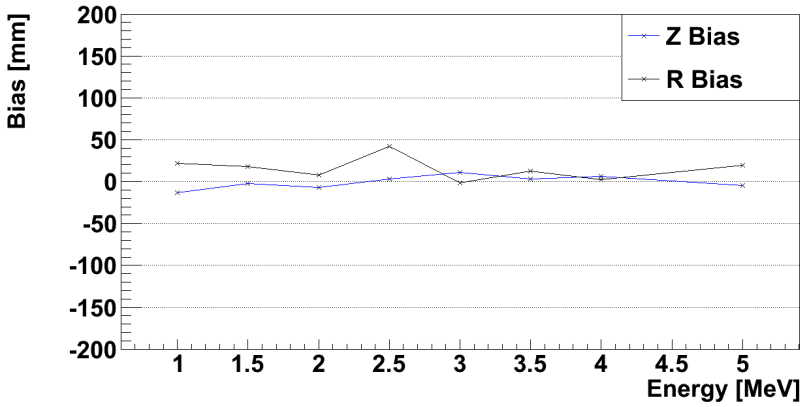

(a) Bias versus energy, fit position minus true position. The z and R bias are consistent with zero.

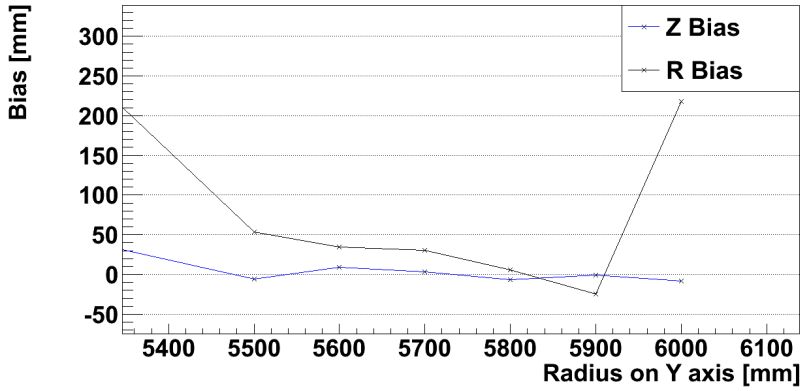

(b) Bias versus position, fit position minus true position. The bias drops with increasing radius except at 6000mm. As the NearAV fitter ensures fitted positions are within 6060mm (AV radius) the bias is hard to define at this position.

Figure 6.8: NearAV, bias as a function of energy and a function of position.

of 0.6ns and a resolution of 0.3ns.

6.7 Energy Reconstruction

The number of emitted scintillation photons is proportional to the energy deposited in the scintillator and hence the energy of the charged particle depositing the energy. As the number of detected PMT hits (Nhit) is proportional to the number of emitted photons the Nhit value is proportional to the deposited energy.

Ideally the number of detected hits would depend solely on the deposited en-

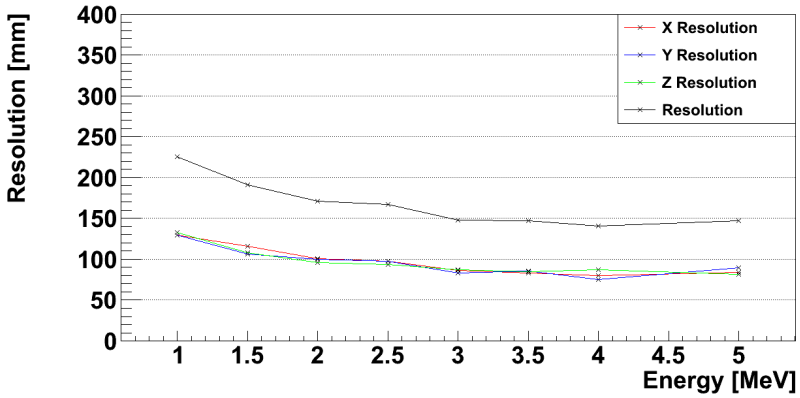

(a) Resolution versus energy. The resolution drops with energy until 3MeV and thereafter stays at 150mm. The lack of energy dependence above 3MeV is due to multiple hits on the same PMT, hence the overall number of hits does not increase with energy. The resolution is expected to improve with the square root of the number of hits.

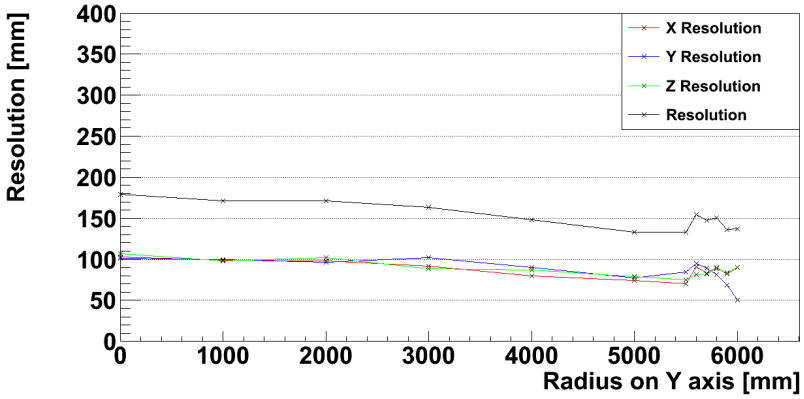

(b) Resolution versus position. The resolution drops with increasing radius until the near AV region.

Figure 6.9: Maximum likelihood emissionTime PDF combination, resolution as a function of energy and a function of position.

ergy with statistical fluctuations governed by Gaussian statistics. Hence, the Nhit per MeV (Nhit_{MeV}) of deposited energy value would be a constant for all interaction positions (within the scintillator) and particle type. This assumption gives a value of $\text{Nhit}_{\text{MeV}} = 389$, as determined by simulating 1MeV electron events at the detector centre. Furthermore, the Gaussian resolution divided by the square root of the fitted energy, $\sigma/\sqrt{E_{fit}}$, should be constant as a function of energy. I have developed an energy reconstruction algorithm where $E_{fit} = \text{Nhit}/\text{Nhit}_{\text{MeV}}$,

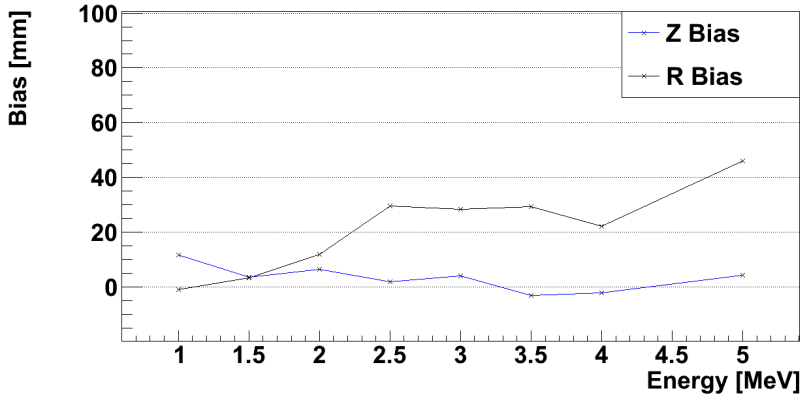

(a) Bias versus energy, fit position minus true position. The z bias is consistent with zero. However, the radial bias increases with energy, with the reconstructed vertex being pulled away from the detector center.

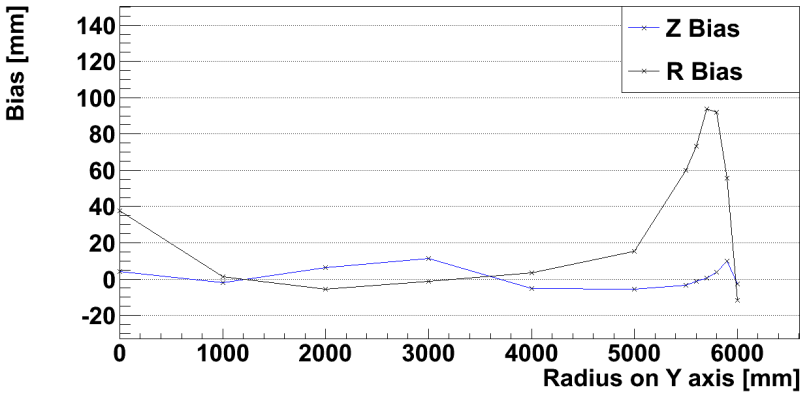

(b) Bias versus position, fit position minus true position. Only the near AV region shows strong bias and then only in the radial direction.

Figure 6.10: Maximum likelihood emissionTime PDF combination, bias as a function of energy and a function of position. The bias at 6000mm is difficult to quantify as this fitter combination forces the reconstructed position to be within the AV radius.

this will be referred to as the simpleEnergy method.

The bias of the simpleEnergy algorithm degrades with energy, becoming severely large and negative at energies above 3.5MeV. The changing bias with energy indicates that the value of $\mathrm{Nhit_{MeV}}$ is energy dependent. Furthermore, the negative bias indicates that the $\mathrm{Nhit_{MeV}}$ value decreases with higher energy. The $\frac{\sigma}{\sqrt{E_{fit}}}$ should be flat, as between 1MeV and 3MeV, however above 3MeV the resolution increases sharply with energy.

The poor performance of the simpleEnergy algorithm indicates an energy dependent value of $\mathrm{Nhit}_{\mathrm{MeV}}$, which decreases with increasing energy. This is expected as the number of multiple hits on the same PMT increases with number of photons and hence energy. A multiple hit PMT will only register a single hit, hence whilst the true hits linearly increase with energy the actual hits per energy will be less. This effect is enhanced with increasing radius as the solid angle of the near PMTs is much higher increasing the fraction of multiple hits further.

6.7.1 EnergyLookup Performance

To account for the problems in the simpleEnergy fitter I have developed a new algorithm called energyLookup. This algorithm allows the value of $\mathrm{Nhit}_{\mathrm{MeV}}$ to vary with energy and position. Hence, given a Nhit and position, as reconstructed by the previous algorithms, the energy can be ascertained from a lookup table of values. These values are extracted for electron interactions at set radial positions, and are shown in figure 6.11.

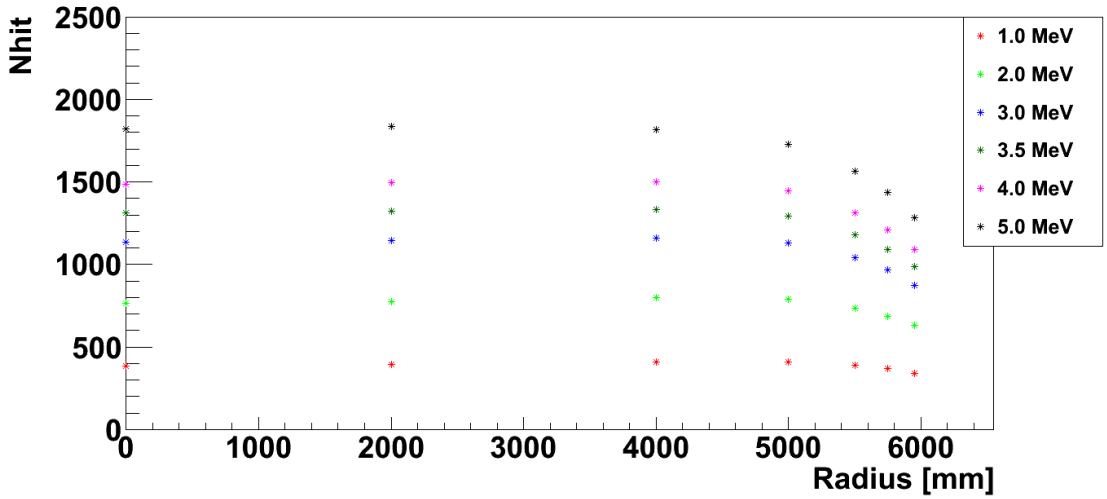

Figure 6.11: $\mathrm{Nhit}_{\mathrm{MeV}}$ values for different electron energies as a function of true event position. Note the $\mathrm{Nhit}_{\mathrm{MeV}}$ values dropping sharply with increasing radius (above 5000mm) for all energies.

The energyLookup algorithm improves on the simpleEnergy algorithm in both

bias and resolution as seen in figures 6.12(a) and 6.12(b). The figures show results with and without a fiducial volume cut, as the near AV region has special optics it also significantly changes the $\mathrm{Nhit_{MeV}}$ value, see figure 6.11. The lower values of $\mathrm{Nhit_{MeV}}$ combined with the sharply changing values with radius will serve to increase the fit sigma degrading the performance. This degradation will increase with poorer position resolution in this region. However, as a fiducial volume cut will be applied, the sigma values with this cut applied are used in this thesis.

The energyLookup bias has no energy dependence and is within 0.03MeV over the 0 to 5MeV domain. The energyLookup sigma has a square root energy dependence that was characterised as:

$$\sigma = -0.015\mathrm{MeV} + 0.071\mathrm{MeV}^{1/2} * \sqrt{E_{fit}/\mathrm{MeV}} \tag{6.21}$$

The relative energy resolution ($\frac{\sigma}{E}$) scales as $0.07/\sqrt{E/\mathrm{MeV}}$ or $7\%/\sqrt{E/\mathrm{MeV}}$, this compares favourably with KamLAND, which achieved $7\%/\sqrt{E/\mathrm{MeV}}$ scaling during the latest ^{8}B analysis[75].

6.8 Conclusion

The position and energy reconstruction algorithms developed perform well, with a energy resolution of 0.12MeV at 3.5MeV. Furthermore, a technique to identify events near the AV has been coded and developed to reconstruct positions, allowing it to be used to reject background events. These results can now be used to quantify the SNO+ sensitivity with realistic energy reconstruction and efficiencies.

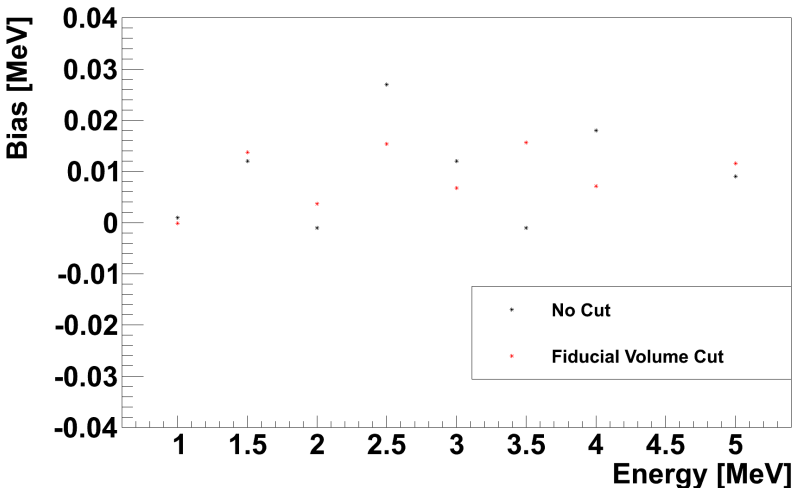

(a) Bias. Note the energy independence of the bias.

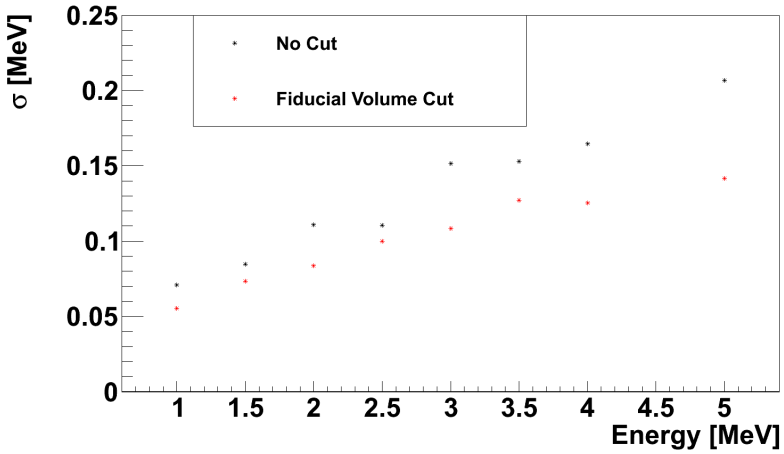

(b) Resolution. There is an expected square root dependence with energy.

Figure 6.12: Bias and Resolution of the EnergyLookup algorithm.

Chapter 7

Double Beta Phase Backgrounds

The SNO+ purification systems are summarised followed by the SNO+ double beta phase backgrounds. A full set of pileup backgrounds are also presented alongside required purity limits. I conclude that pileup rejection is required for SNO+ sensitivity to neutrinoless double beta decay.

Ideally the SNO+ experiment would be background free in the double beta signal region, and whilst this is the aim it will not be achieved. Hence these backgrounds will limit the SNO+ sensitivity to the $2\beta0\nu$ half-life and hence effective neutrino mass. Furthermore, the backgrounds in the signal region must be well understood to explain any observed signal.

The backgrounds listed in this chapter are those that give rise to events with a reconstructed energy in the signal region or could pileup resulting in new events with a reconstructed energy in the signal region. These backgrounds have been identified by the SNO+ backgrounds group, with further pileup backgrounds identified by myself.

The double beta phase signal is an ideal delta function spectrum centred at 3.37138(20)MeV [31]. The signal half-life is of order, $T^{0\nu}_{1/2} = 1.1{\times}10^{25}yr$, see section 1.3.1. For the purposes of background discussion the signal region is considered as between 3MeV to 4MeV. All decay schemes and information included in this

chapter comes from the Table Of Isotopes[76].

7.1 Backgrounds Overview

The SNO+ detector utilises the graded-shield design to ensure that the centre of the detector has minimal background activity. Therefore the backgrounds will be discussed starting from those with the most external (to the centre) origin. These backgrounds can also be classified as solar neutrinos, natural radioactivity and cosmogenic.

7.1.1 Solar Neutrinos

The ^{8}B neutrino flux which was a signal for SNO is now a SNO+ background for the double beta phase. The ^{8}B neutrinos are visible following elastic scattering in the scintillator. This flux rises as a function of energy peaking at ≈6MeV [77], the elastic scattering cross section also rises; however, the neutrino does not transfer all its energy to the electron, rather it peaks at low energies and decreases with higher energies. Thus the ^{8}B background spectrum is slightly falling in the signal region. Helpfully this background is constrained by previous SNO measurements.

7.1.2 Cosmogenic Backgrounds

Cosmogenic backgrounds come in two kinds, muons traversing the scintillator and muon-induced radioactivity. The former is reduced by the depth of the detector, whilst the latter is also a concern whilst the scintillator is above the surface (during manufacture and delivery).

As the SNO+ detector is located at an equivalent depth of 6010m in water the cosmic ray muon rate is around 70 a day[78]. Furthermore the energy of the muon is typically much above the SNO+ signal and other backgrounds[79], allowing this

Isotope	Half Life
^{16}N	7.13 seconds
^{11}C	20 minutes
^{10}C	19.3 seconds
^{11}Be	13.8 seconds
^{7}Be	53.3 days

Table 7.1: Radioactive isotopes produced by muon interactions in the scintillator[81]

background to be easily identified and rejected.

Muon interactions in the scintillator are expected to produce the radioactive isotopes in table 7.1. The radioactive isotopes ^{16}N, ^{10}C, ^{11}Be have sufficiently short half lives that only a few minutes need elapse for these decays to have occurred. This allows decays within a few minutes of a muon crossing to be identified and rejected by a detector veto[1].

The isotopes ^{11}C and ^{7}Be live too long for a detector veto approach; fortunately neither are a problematic background for the double beta phase. ^{11}C β^+ decays with an end point of 0.96MeV which when combined with the annihilation energy of 1.022MeV gives a spectrum between 1.022MeV and 1.98MeV well below the signal region. Furthermore the ^{11}C decay rate is expected to be less than $1135kt^{-1}yr^{-1}$[80], which is unlikely to cause pileup backgrounds. ^{7}Be decays by electron capture emitting a 0.477MeV gamma 10% of the time; this is also well below the signal region.

7.1.3 External Backgrounds

Decays outside of the AV may produce gammas and charged particles. These decays are caused by naturally occurring external backgrounds in the AV, water, ropes and PMTs. Charged particles produced by decays in the water, ropes and

[1]Further effort to reconstruct the muon path and veto spatial volumes is being carried out by the SNO+ group.

PMTs are likely to be severely attenuated in the water before reaching the scintillator. Therefore only gamma producing background decays are a concern for these regions.

Each PMT contains approximately 100μg of ^{238}U and 100μg of ^{232}Th. Due to the attenuation in the water only the high energy gamma decays of ^{214}Bi in the ^{238}U chain and ^{208}Tl in the ^{232}Th are a concern[81]. ^{208}Tl beta decays with coincident gammas; $Q = 5.0$MeV with predominant modes, 1.04MeV beta 3.1%, 1.292MeV beta 24.5%, 1.525MeV beta 21.8% and 1.802MeV beta 48.7% of the time[2] The principle ^{208}Tl gamma is 2.615MeV 100% of the time. ^{214}Bi beta decays with coincident gammas, $Q = 3.272$MeV with predominant modes, 3.272MeV beta 20%, 1.425MeV beta 8.3%, 1.5MeV beta 35% and 1.895MeV beta 7% of the time. ^{214}Bi emits gammas with a combined energy above 2MeV more than 2% of the time.

The ultra-pure water (UPW) surrounding the AV and PSUP is purified and chilled before pumping into the detector. This water is taken from the mine supply and dropped 6800ft to the SNOLAB complex underground leaving the water saturated with air. The purification process starts with an deaerator to remove O_2 and N_2, followed by multimedia and 10 micron filters to remove large particulates. Organic matter is then removed by a charcoal filter. A series of cation exchange resins in zeolite softeners remove divalent ions and prepare the water for reverse osmosis (RO). The water is mixed with EthyleneDiamineTetraacetic Acid (EDTA) which forms complexes with ionic species. These EDTA complexes and molecules with a weight greater than 200 u are removed by RO. Finally further organic purification is carried out by UV and ion exchange before the water is re-gassed with N_2 and chilled[47]. This purification process is shown in figure 7.1.

Following the purification process the UPW contains $< 35 \times 10^{-14}$g/g ^{238}U and 3×10^{-14}g/g ^{232}Th. As with PMT backgrounds only the high energy gammas are

[2]The total energy released is Q, the energy remaining after beta decay is released as gammas.

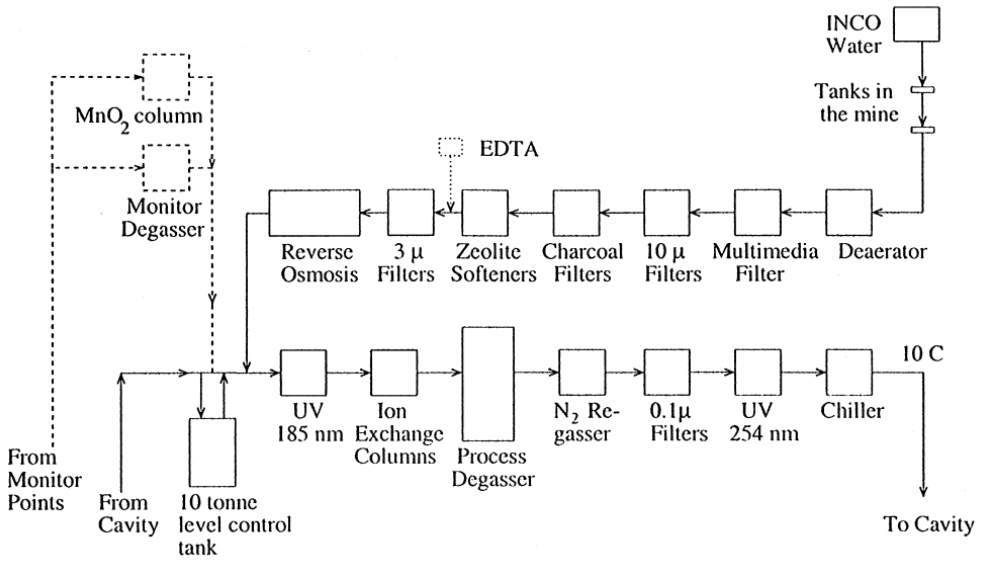

Figure 7.1: Ultra Pure water purification process, figure from [47].

a concern to the double beta phase.

The ropes in the UPW are made of Tensylon as it is low in potassium, uranium and thorium. The ropes contain 0.1 ppb ^{238}U, 0.17 ppb ^{232}Th and 250 ppb $K_{Natural}$ or $\sim 3 \times 10^{-2}$ ppb ^{40}K. ^{40}K β^- decays 89% of the time with an end point of 1.311MeV, and electron captures 10% of the time emitting a 1.46MeV gamma.

The AV acrylic has an intrinsic radioactive content of <1.1 ppt ^{238}U, ^{232}Th and < 2.3 ppb ^{40}K. However, as ^{222}Rn is electrostatically attracted to the surface a quantity of ^{210}Pb will be embedded by recoil, during the construction of SNO and SNO+. This is problematic as it is unknown how much is embedded nor is it known if it will leach into the scintillator. The construction phase of SNO+ includes effort to remove the embedded ^{210}Pb by sanding the internal AV surface.

During operation the void above the scintillator below deck will be pumped full of N_2 cover gas in a closed system. This prevents the radon contaminated mine air from interacting with the scintillator.

The external background rates will have a strong radial dependence, with the rates decaying quickly as the distance inwards from the AV increases. A previous

fiducial volume of 4.5m has been identified as sufficient to reduce the external background rate to the level of the $2\beta2\nu$ rate[82]. Therefore I will not show external backgrounds in energy spectra plots, and apply a 50% fiducial volume cut when calculating limits.

7.1.4 Internal Scintillator Backgrounds

A number of radioactive isotopes are present in the LAB scintillator and PPO fluor. As delivered PPO is too radioactive to be placed into the detector and thus a series of purification techniques will be carried out. On delivery PPO will be purified by water extraction followed by multi-stage distillation. Whilst LAB will be purified by multi stage distillation. LAB and PPO are then mixed and further purified by steam/N_2 stripping before being pumped into the detector.

The water extraction purification process requires a significant difference in the water solubility between the background contaminants and PPO/LAB. Most radioactive contaminants are ionic metals that are more soluble than LAB in water allowing them to be removed[83].

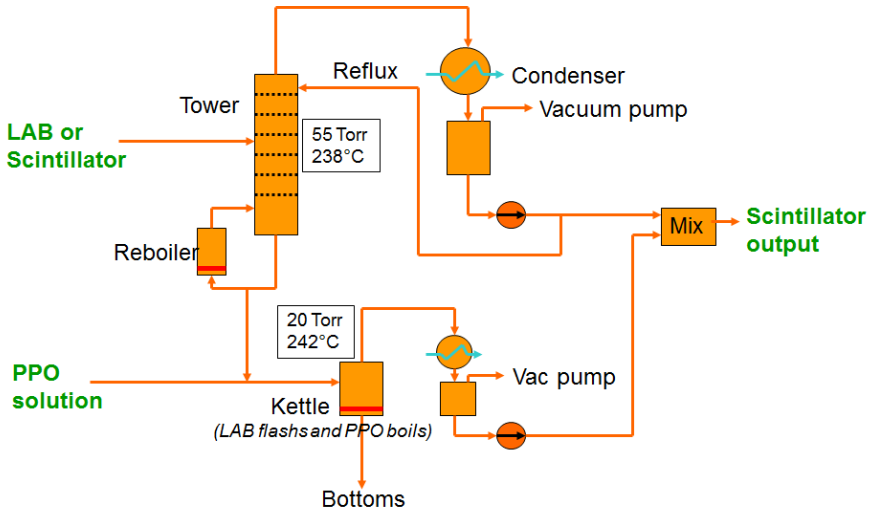

Figure 7.2: Distillation process for LAB and PPO, figure from [83].

The distillation purification process shown in figure 7.2, removes heavy met-

Isotope	Borexino Level (g/g)
^{238}U	1.60×10^{-17}
^{232}Th	6.80×10^{-18}
^{210}Pb	6.11×10^{-25}
^{210}Bi	3.78×10^{-28}
^{210}Po	4.15×10^{-24}
^{40}K	$< 1.30 \times 10^{-18}$
^{39}Ar	$< 2.75 \times 10^{-24}$
^{85}Kr	$< 2.40 \times 10^{-25}$
^{14}C	1.00×10^{-18}

Table 7.2: Radioactive isotopes present in the scintillator and known achievable levels from the Borexino experiment. Table taken from [81]

als, small particulates, and cosmogenic contaminants. These contaminants are removed due to their low volatility in comparison with LAB and PPO. During operation the scintillator will be recirculated through the purification processes, in this operation PPO will drop out of the LAB tower whereas LAB will flash through the PPO tower[83].

The mixed scintillator (LAB + PPO) is then steam stripped to remove noble gasses and de-oxygenate the scintillator. De-oxygenating improves the optical quality of the organic LAB scintillator[70]. Steam stripping is more effective for SNO+ due to difficulties in getting enough pure N_2 underground[83].

The purification system for the scintillator is expected to reduce the radioactivity in the scintillator to or below the levels seen in KamLAND and Borexino[81]. The equivalent g/g amounts of scintillator backgrounds seen in Borexino are shown in table 7.2. As the SNO+ purification systems are similar to Borexino and built by the same company I will use the Borexino values henceforth.

^{238}U is a very long-lived isotope which decays by alpha emission to ^{234}Th which also subsequently decays forming the decay chain shown in figure A.2. I will assume the ^{238}U chain is in equilibrium in the scintillator; however this may not be the case (for example if radon enters the scintillator and produces ^{210}Pb or elements in the chain plate out onto the AV). This could be a particular concern

for ^{210}Pb as it has long half-life. A large contamination of ^{210}Pb will lead to extra pileup backgrounds not considered in this chapter.

^{232}Th also forms a decay chain as shown in figure A.1. I will also assume this chain is in equilibrium in the scintillator; however this chain like the U chain can be out of equilibrium through differences in the solubility of the isotopes. The full decay schemes including all modes with a $> 1\%$ intensity will be included in the background plots.

The other principle backgrounds are, ^{39}Ar beta decays with a 0.565MeV end point, ^{85}Kr beta decays with a 0.687MeV end point, and ^{14}C beta decays with a 0.156MeV end point.

7.1.5 Nd Backgrounds

Natural neodymium (Nd) contains 5.6% ^{150}Nd, 23.8% ^{144}Nd and further 70.6% stable isotopes. As the neutrinoless double beta decay mode ($2\beta0\nu$) of ^{150}Nd is the only signal the other decay modes of ^{150}Nd and ^{144}Nd are backgrounds. ^{144}Nd decays by emission of a 1.83MeV alpha. The $2\beta2\nu$ half life used is $T^{2\nu}_{1/2} = 9.11 \times 10^{18} yr$, which the the best fit value measured in NEMO3[40].

7.1.6 Internal Nd Backgrounds

Natural neodymium (Nd) contains radioactive isotopes of neodymium and other elements. The contamination from radioactive isotopes can be reduced by enrichment and other elements by purchasing purer neodymium. However, this is more expensive and is dependent on the neodymium quality as mined. Therefore SNO+ has also developed a method to purify the neodymium allowing cheaper and mine independent neodymium to be purchased.

The Nd purification process starts with pH adjustment co-precipitation (also called self-scavenging). This consists of dissolving the Nd salt in water, adjusting

Sample	^{138}La μ g/g	^{176}Lu μ g/g	^{40}K μ g/g	^{227}Ac μ Bq/g	^{214}Bi μ Bq/g	^{208}Tl μ Bq/g
99.9995%	< 0.54	< 0.08	0.49 ± 0.30	3.1 ± 2.1	1.6 ± 0.9	11.6 ± 1.5
Purified	< 0.43	0.12 ± 0.02	25 ± 3	< 6.2	3.0 ± 1.9	1.8 ± 1.5

Table 7.3: Radioactive isotopes present in the Nd and measured levels. Table taken from [84]

the pH with concentrated NH_4OH to 6.03. After stirring for 60 mins the solution is gravitationally filtered and the water evaporated. To load the Nd into the organic scintillator the Nd is combined with trimethyl hexanoic acid (THMA). THMA is chosen as it has lower water solubility, improving the water extraction purification of the Nd-loaded LAB. The THMA itself is purified via a thin film evaporator column.

After purification the Nd still contains ^{138}La, ^{176}Lu, ^{40}K, ^{227}Ac and ^{238}U, ^{232}Th. The levels as measured are shown in table 7.3. The Nd may also contain small amounts of ^{147}Sm and ^{148}Sm.

^{138}La beta decays with a 0.255MeV end point and 0.789MeV coincident gamma 33.6% and 1.436MeV gamma decays 66.4%, of the time. ^{176}Lu beta decays with a 0.595MeV end point and 0.597MeV coincident gamma. ^{227}Ac 5.042MeV alpha decays 1% of the time, whereas the various beta decays with gammas release a maximum energy of 0.05MeV.

7.1.7 Background Rates

SNO+ will contain 774Mg[3] of LAB within the AV, loaded with either 0.1% or 0.3% natural Nd in the double beta phase. Given the proposed masses of material and the radioactivity levels given above the internal background rates expected in SNO+ are given in table 7.4.

The expected energy spectra for 0.1% Nd loaded scintillator given a single

[3]Using the AV volume of $908m^3$ and the temperature dependent density given in [85] the mass is: $908m^3 \times (0.86 - 5.88 \times 10^{-4} \times (285 - 273)[K]) = 774,473,152g$.

Background	Events per year
CNO	1×10^4[86]
PEP	8×10^3[86]
^{8}B	1×10^3[86]
^{85}Kr	8×10^4
^{40}K	8×10^4
^{14}C	4×10^9
^{39}Ar	8×10^4
^{210}Pb	4×10^4
^{210}Bi	4×10^4
^{238}U Chain	4×10^3
^{210}Po	1×10^7
^{232}Th Chain	6×10^2
0.1% Loading	
^{138}La	9×10^9
^{150}Nd 2ν	1×10^7
^{176}Lu	5×10^9
^{144}Nd	2×10^{11}
^{147}Sm	1×10^{10}
0.3% Loading	
^{138}La	2×10^{10}
^{150}Nd 2ν	5×10^7
^{176}Lu	2×10^{10}
^{144}Nd	7×10^{11}
^{147}Sm	3×10^{10}

Table 7.4: Radioactive isotopes present in the Nd loaded scintillator and the expected number of events per year.

year live time is shown in figure 7.3. Sub figure 7.3(b) shows four backgrounds in the signal region, ^{8}B, ^{232}Th chain, ^{238}U chain and $2\beta2\nu$. The ^{8}B background in dark blue is irreducible being due to solar neutrinos. The $2\beta2\nu$ background is also irreducible. However, the purification methods outlined above may reduce the ^{232}Th chain and ^{238}U chain backgrounds. However given the similar shapes for ^{238}U chain and $2\beta2\nu$, the ^{238}U chain background is less of a concern, as it is dominated by the $2\beta2\nu$ background.

7.2 Pileup Backgrounds

The background rates and spectra presented so far omit pileup between multiple backgrounds. Pileup will occur if two or more backgrounds decay within the same event trigger window. Hence the event will have an apparent energy equal to the sum of the two decay energies. As the trigger window is short (400ns) only the very high rate backgrounds are likely to pileup.

The pileup rate between two backgrounds is calculated via Poisson statistics. Given a decay of background A, the probability of a decay of background B within the next 400ns is:

$$P(k = 1, \lambda_B) = \frac{\lambda^k e^{-\lambda_B}}{k!} \tag{7.1}$$

Where λ_B is the average number of decays of B in 400ns. Hence the number of single pileup events $N_P = N_A * P(k = 1, \lambda_B)$, and double pileup for k=2 and very high rate backgrounds. Triple pileup is too rare to be a concern for SNO+, unless the background rates are much higher than predicted.

It is important to consider pileup of B with A as above but also A with B, i.e. event B first then A within 400ns. This was neglected in the previous pileup calculations for SNO+. However all numbers and plots I generate will include both time orderings.

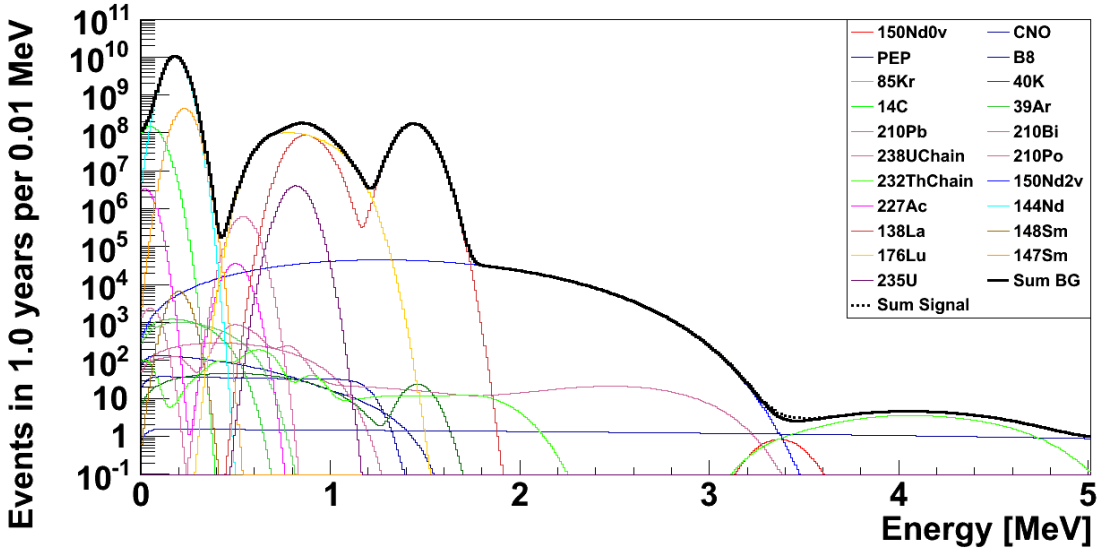

(a) Spectra over the full energy domain

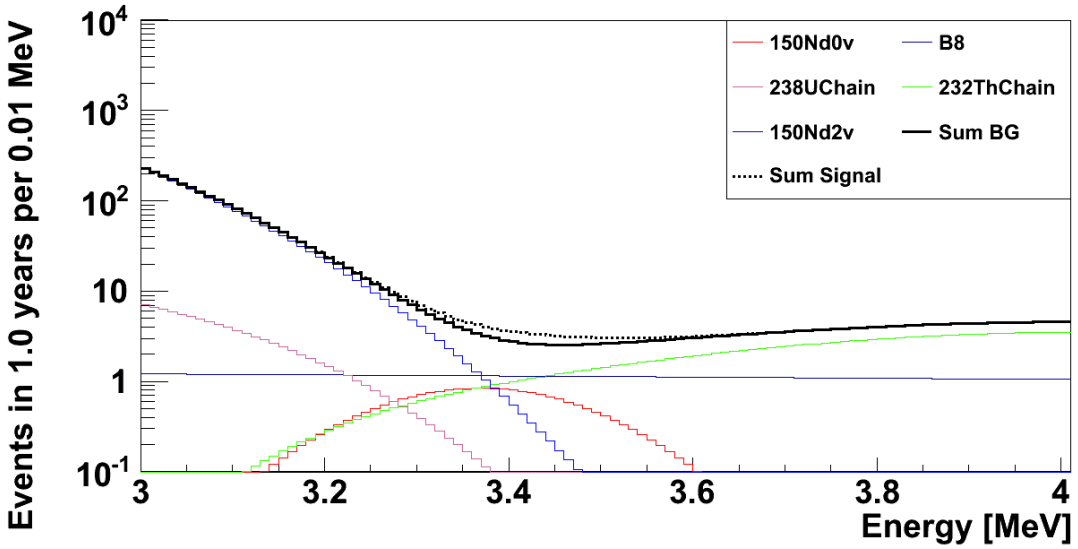

(b) Spectra in the signal region

Figure 7.3: Expected energy spectra generated by SNO+py to simulate the SNO+ detector. This corresponds to a year of running 0.1% loaded Nd scintillator with no pileup spectra calculated. Rates used are those from table 7.4. Each spectrum is convoluted with the energyLookup energy resolution given in section 6.7.1.

The pileup background will have a different energy, which will equal the sum of the individual backgrounds. Hence the pileup background spectrum may have events in the signal region. The pileup included energy spectrum using the background rates in table 7.4 is shown in figure 7.4.

Sub figure 7.4(b) shows five additional single (+ in legend) pileup backgrounds and two double (++ in legend) pileup backgrounds[4] in the signal region. The extra single pileup backgrounds are $2\beta2\nu$ with ^{138}La, $2\beta2\nu$ with ^{176}Lu, $2\beta2\nu$ with ^{144}Nd, ^{138}La with ^{138}La, ^{138}La with ^{176}Lu. The extra double pileup backgrounds are ^{138}La with ^{138}La and ^{138}La, and ^{138}La with ^{176}Lu e.g. ^{138}La + ^{138}La + ^{176}Lu. Furthermore, the pileup between $2\beta2\nu$ and ^{147}Sm (not shown) would also be a concern if the contamination of ^{147}Sm is much higher than currently expected.

7.2.1 Acceptable levels

The background levels due to pileup shown in figure 7.4 must be reduced to improve the sensitivity of the SNO+ experiment. This reduction can be done by further purification of the Nd-loaded scintillator or by identifying and rejecting the pileup backgrounds. The latter approach will be explored in chapter 8.

The pileup backgrounds are only a concern for the double beta phase if the spectrum overlaps the signal. Previous work by A Wright and E Vazquez consider the signal region to be from 3.0MeV to 3.7MeV. I will follow this definition in this section alone, to allow comparisons between the different pileup calculations.

^{8}B is an irreducible background in the signal region, therefore the pileup background activity should ideally be reduced to or below the ^{8}B activity. The ^{8}B background level results has an activity of 164 events per year in the signal region. This allows target purities of backgrounds that pileup to be calculated; these are shown in table 7.5.

The previous SNO+ levels shown in table 7.5 are the level at which 10 or less

[4]Single pileup is two interactions per event, double pileup is three.

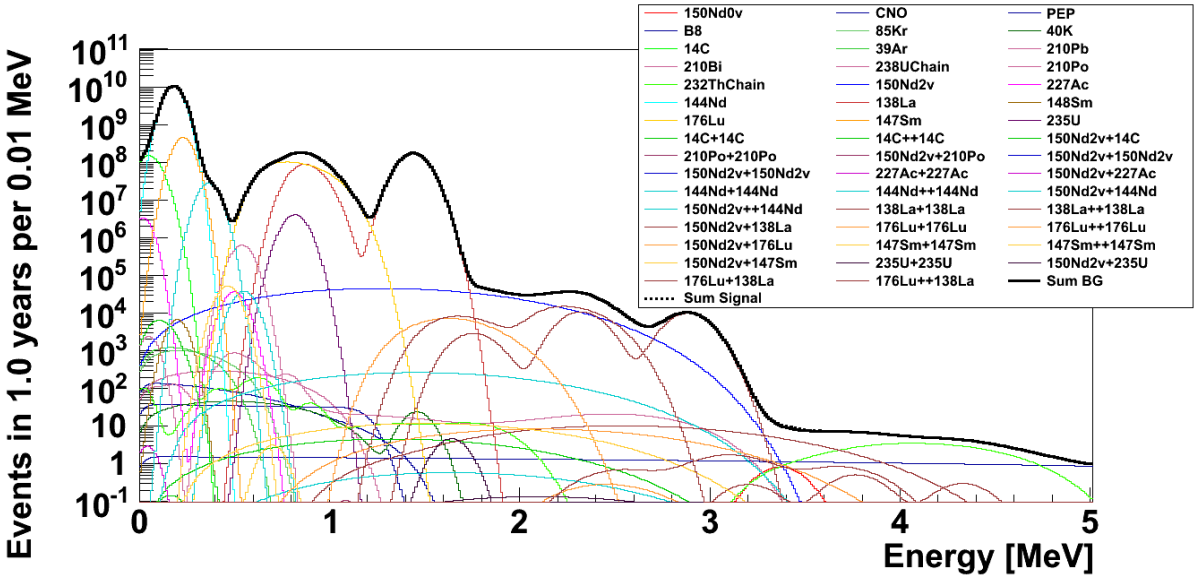

(a) Spectra over the full energy domain

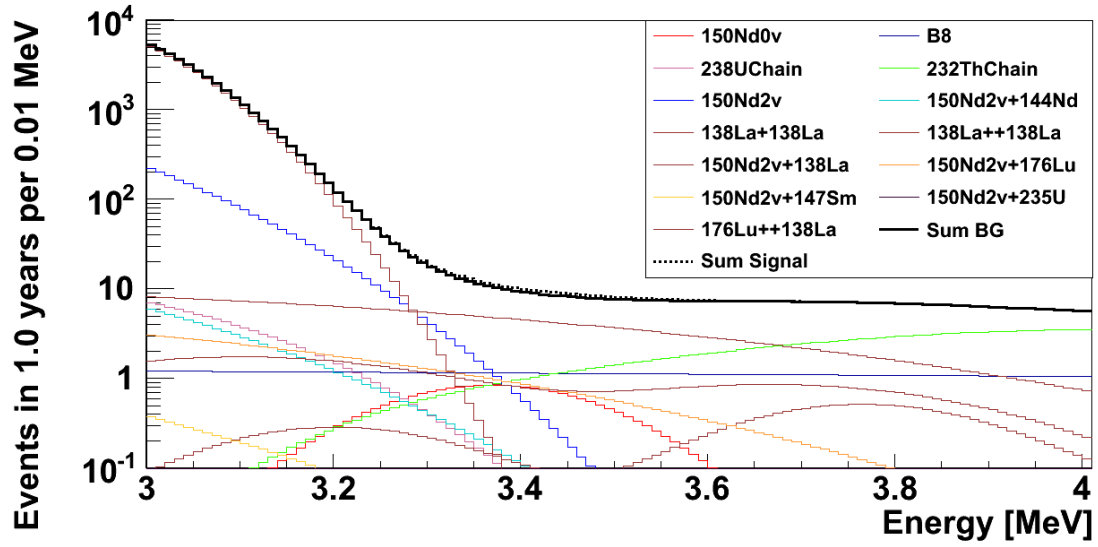

(b) Spectra in the signal region

Figure 7.4: Expected energy spectra generated by SNO+py to simulate the SNO+ detector. This corresponds to a year of running 0.1% loaded Nd scintillator with pileup spectra calculated. Rates used are those from table 7.4. Each spectrum is convoluted with the energyLookup energy resolution given in section 6.7.1.

Isotope	3.0 - 3.7MeV	Previous SNO+ Level
0.1% Nd Loading		
	g/g Nd	
^{138}La	2.5×10^{-7}	5×10^{-7}
^{176}Lu	5×10^{-7}	1×10^{-7}
^{147}Sm	5×10^{-5}	1×10^{-6}
	g/g LAB	
^{14}C	2.5×10^{-15}	1.94×10^{-18}
^{39}Ar	2.5×10^{-17}	1×10^{-21}
0.3% Nd Loading		
	g/g Nd	
^{138}La	2.5×10^{-08}	-
^{176}Lu	5.0×10^{-08}	-
^{147}Sm	5.0×10^{-06}	-
	g/g LAB	
^{14}C	5.0×10^{-16}	-
^{39}Ar	6.3×10^{-18}	-

Table 7.5: Acceptable background contamination levels such that the number of events in each energy region is equal or less than that of ^{8}B. The previous SNO+ levels are from [87]

events occur in the energy region 3.0 to 3.7MeV. Furthermore the calculation uses only pileup of $2\beta2\nu$ followed by the background isotope. Whereas, the levels I have calculated include pileup of the background followed by $2\beta2\nu$. The 0.3% loading acceptable levels are beyond the current proved purification.

7.3 Conclusion

The pileup backgrounds severely increase the background count in the signal region and thus limit the sensitivity of SNO+. Hence a method of identifying and rejecting these pileup backgrounds will be necessary for SNO+. This motivates the following chapter and study into pileup rejection.

Chapter 8

Pileup Rejection Techniques

Pileup types are defined. A series of pileup identification techniques are detailed. The efficiency of these techniques is presented and used to recalculate the SNO+ energy spectra.

The SNO+ experiment neutrinoless double beta decay phase will have backgrounds in the signal region due to pileup. Pileup is the occurrence of multiple background decays within the same trigger window. If these events cannot be identified and rejected they will be considered good events, leading to higher background levels in the signal region.

I have developed the following techniques to identify pileup events. These techniques are developed to meet a target of less than 10% false rejection of single interaction events and greater than 99% rejection of pileup events.

8.1 Definition of Pileup

A pileup event is distinct to a normal event in that it contains PMT hits within the trigger window from multiple separated interactions. One of these interactions is the cause of the trigger that then defines the event, see section 6.1. The other separate interactions then increase the Nhit count for the event and thus the apparent event energy, causing a new background as described in the previous

chapter.

The timing or pileup window in which separate interactions can increase the Nhit count in the event will depend on whether the interaction has sufficient hits to cross the trigger threshold[1]. Consider the trigger window shown in figure 8.1, which contains the interactions A, B, D, E. The 400ns blue box is the full trigger window, within which the interactions A, B, D, E cause registered hits. The dashed blue line corresponds to the trigger threshold level and exists only when events could be triggered. The red 220ns lines show the post-latched trigger window leaving a 180ns pre-latched trigger window.

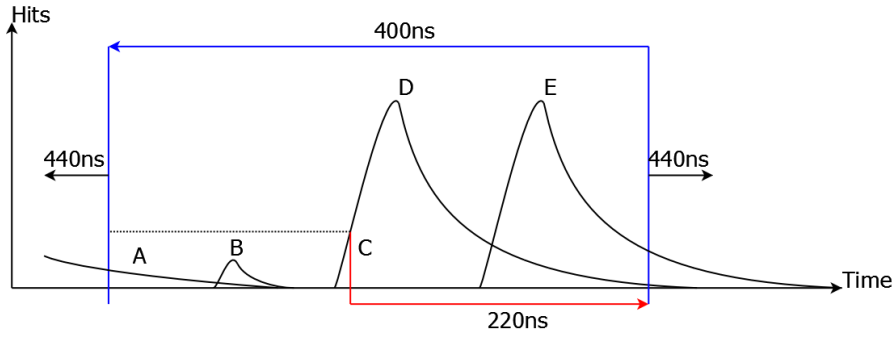

Figure 8.1: Described in main text.

If there are multiple interactions above-threshold the pileup window will decrease to 220ns, as the first (causal) interaction will trigger leaving only 220ns for further interactions e.g. D and E. If there are decays below threshold accompanied by a decay above threshold the pileup window is 400ns, e.g. D and B (or E if E was below threshold). If there is a high energy interaction that still causes hits 40ns + 220ns after its trigger followed immediately by another interaction above threshold they will pileup, e.g. A and D. In summary there are three definitions: decays above threshold and within 220ns, decays above threshold separated by more than 260ns and decays below threshold and within 400ns.

In this chapter I will refer to pileup events as Type 1, 2 or 3 based on the trigger window property. Type 1 events will consist of multiple above threshold

[1]This is expected to be equivalent to an electron interaction with a K.E of 500keV.

interactions within a pileup window of 220ns. Type 2 events will consist of a single above threshold interaction and multiple below threshold interactions within a pileup window of 400ns. Type 3 events will consist of a tail from an interaction above threshold before an above threshold interaction that defines the event, increasing the pileup window as a function of the previous event energy (larger energy gives longer tails).

Pileup events can be further characterised by a description of the interactions, and the rejection techniques will preform differently depending on this characterisation. A description of the different characterisations follows:

A Interactions occurring in different spatial locations.

B Interactions occurring at different times.

C Interactions occurring of different energies.

D Interactions occurring of different particle types.

E Interactions occurring with the decay particles having differing momentum directions.

Note that events that do not satisfy B (i.e. decays at the same time) may still record at different times within the trigger window due to transit times. Therefore all pileup events are a combination of either 1, 2 or 3 and any combination of A, B, C, D and E.

8.1.1 Definition as relevant to SNO+

For the SNO+ neutrinoless double beta decay phase only electron-like pileup events with a reconstructed energy in the signal region matter. Therefore all the rejection techniques are optimised to work in the signal region; this leads to

poorer performance at lower total energies[2].

8.2 Summary of single interaction event properties

The properties of single interaction (good) events that allow position and energy reconstruction as outlined in section 6.1.2 can also be used as pileup discriminators. In summary the isotropic nature and well-defined timing spectrum of emitted photons allow reconstruction and thus any deviations are good pileup indicators. Therefore good events away from the AV will have a single peak in the raw timing spectrum (at D in 8.1) and an exponentially decaying tail after. Furthermore, in the 400ns window there will be approximately three uniformly distributed hits due to noise.

8.3 Initial Techniques

Deviations from the well-defined timing spectrum is the easiest and potentially most rewarding indicator of pileup. However the timing spectrum is defined on emission and not in terms of the raw hit times. Therefore a reconstructed position and interaction time must be used to convert the raw hit times into emission times. The reconstructed emission time spectrum can then be used as a test for pileup.

The following techniques were tried on the reconstructed emission time spectrum. The rise time width, fall time width, mean time, location of the peak (relative to decay time) and ratio of hits in the peak to total hits. Cuts for each of these indicators were then developed based purely on good events. Unfortunately only the mean time and ratio of hits in peak to total proved useful to discriminate

[2]Pileup may also be a concern for the solar phase, where data will be taken without neodynium at lower energies. This will require a retuning of the rejection techniques.

pileup. This is because the reconstruction algorithm has already made use of the timing information to reconstruct the event. Therefore the reconstructed emission time spectrum will either be close to the expected spectrum or not exist as the reconstruction algorithm failed.

The initial techniques show that the reconstruction algorithm itself is a powerful pileup identifier, as the reconstruction algorithms are in effect attempting to fit the event to the well-defined timing spectrum. Therefore events that cannot be reconstructed can be identified as pileup and rejected.

8.4 Raw Data Techniques

The raw data for an event are the PMT hit times and charge, which includes the implicit PMT spatial hit distribution. This raw data has implicit properties for single decay events which can be checked e.g. PMT hit times should occur after the trigger.

Identifying pileup events at the raw data stage allows generic identification algorithms to be developed that need no assumptions about the reconstruction. Furthermore, event reconstruction is an execution time costly process, so quickly identifying pileup events before reconstruction is beneficial.

8.4.1 Pre Trigger Hits Technique

The pre trigger hits technique counts the number of hits occurring before the event trigger in the raw timing spectrum, e.g. hits such as those from A and B in figure 8.1. Good events will typically have a maximum of three hits due to noise. Hence a count of the hits is a strong discriminant for type 2, where the below threshold decay(s) occur before the above threshold decay and type 3 pileup events.

The sum of hits between 100ns and 250ns in the raw timing window is calculated. As the trigger occurs around 280ns $\pm$ 20ns, 250ns is chosen to allow for the

event rise time before the trigger threshold is crossed. The event rise time occurs as the event will only trigger when O(10) hits occur[3]. The number of pre trigger hits can then be cut on for pileup identification.

This technique rejects all type 2 pileup events, except those consistent with noise i.e. <4 hits. It also rejects all type 3 pileup events where the below trigger event occurs in the pre trigger technique window. This effectively reduces the type 3 pileup window to 250ns, as 400ns − (180ns − 30ns) = 250ns. However this technique has no effect on type 1 pileup events.

8.4.2 Number of Peaks Technique

The number of peaks technique counts the number of distinct peaks in the raw timing spectrum. Good events will have a single peak unless the interaction occurs near the Acrylic Vessel. These interactions occurring near the Acrylic Vessel will be identified by the near AV identification technique, section 8.4.3.

A peak is found by differentiating the raw timing spectrum histogram, binned in 5ns bins and then normalising the differential histogram by area. The differential at t_i, $D(t_i)$ is calculated such that:

$$D(t_i) = \frac{T(t_{i+1}) - T(t_{i-1})}{2} \tag{8.1}$$

where $T(t_i)$ is the histogram count for hits in the t_i bin. A peak is then defined whenever $D(t_i) > 0.05$ which allows for statistical variations; this limit has been chosen empirically such that 3.5MeV electron events have one peak. The number of peaks can then be cut on for pileup identification.

This technique is good at rejecting type 1 A and 1 B events if the ratios of interaction energies are close to unity. However, if the interaction energy ratios

[3]Exact trigger threshold is yet to be decided, but it is likely to be higher than 20 hits for the double beta phase of SNO+.

are large, the smaller energy interactions will give peaks with a similar magnitude to the high energy interaction's statistical fluctuations.

8.4.3 Near AV identification

Events reconstructed near the AV will be rejected as they are outside the fiducial volume, the fiduical volume used in this thesis is r $<$ 4500mm [4]. This is advantageous to the pileup identification as the decays near the AV will not have the same timing spectrum as events away from the AV. Furthermore decays near the AV will not give an isotropic hit pattern or the expected emission time profile. This is due to total internal reflection in the AV, as discussed in section 6.1.3. The near AV identifier in the reconstruction algorithm will be used to reject decays near the AV.

8.5 Post Reconstruction Techniques

Many pileup events will be reconstructed by the reconstruction algorithms despite being pileup. This will happen for example in type A events where the spatial separation is small. Those pileup events that pass the reconstruction can still be identified by the following techniques.

8.5.1 Early Time Technique

The early time technique checks the validity of the reconstructed vertex by counting the number of PMT hits that are not in causal contact. Hits are defined as in causal contact if the hit time minus the transit time from the reconstructed event position is after the reconstructed event time. Good events will only have noise hits out of causal contact.

[4]The actual fiducial volume will be decided based on the measured background rates.

The reconstructed vertex position and decay time (t_0) allows an emission time ($t_{i,emission}$) for every hit PMT (i) to be calculated. The equation is:

$$t_{i,emission} = t_{i,hit} - t_0 - t_{transit} \tag{8.2}$$

Where $t_{transit}$ is calculated as detailed in section 6.4. The number of out of causal contact hits can then be cut on for pileup identification.

8.5.2 Mean Time Technique

The mean time technique checks the validity of the reconstructed vertex by calculating the mean reconstructed emission time. This has shown promise in the initial techniques when used with a non-timing based reconstruction algorithm, or algorithms dominated by the peak with little sensitivity to the tail. Good events should have a well-defined mean reconstructed emission time.

The mean time is simply defined as the average emission time, with the emission times calculated by equation 8.2.

$$\bar{t}_{emission} = \sum_{i}^{N} \frac{t_{i,emission}}{N} \tag{8.3}$$

The value of $\bar{t}_{emission}$ can then be cut on for pileup identification.

8.5.3 Isotropy Technique

The isotropy technique checks the validity of the reconstructed spatial hit pattern. This technique works well for reconstruction algorithms that use timing and not spatial hit information to reconstruct the event. Good events will emit photons isotropically leading to an isotropic spatial hit pattern with respect to the interaction position.

The isotropy of an event was previously measured in SNO+ using a technique

called β_{14}. The β_{14} technique is the sum $\beta_1 + 4\beta_4$ with the definition[88]:

$$\beta_l = \frac{2}{N(N-1)} \sum_{i=1}^{N-1} \sum_{j=i+1}^{N} P_l(\cos\theta_{i,j}) \tag{8.4}$$

where i and j run over the N hit PMTs, $\theta_{i,j}$ is the angle between the two hit PMTs and $P_l(\cos\theta_{i,j})$ is the l^{th} Legendre Polynomial. Small β_{14} values then indicate isotropic events.

I have decided that this technique was inappropriate for SNO+ as SNO+ will have many more hits than SNO; signal events have 1200+ hits in SNO+ whereas SNO had < 100. This results in the computational time required for SNO+ to be O(100) times longer. However, the β_{14} technique is designed to identify more isotropic events than the signal whereas SNO+ needs to identify anisotropic events. Therefore the following technique is a better choice for SNO+.

Given the reconstructed event position each equal solid angle region of the PSUP will ideally have the same number of hits. Hence, constructing a few regions and checking the count in each against the other regions is a measure of the isotropy. This computational effort will thus scale with the number of hits and not the number of hits squared like β_{14}.

To construct the equal solid angle regions the event axis is used to define the axis between two poles of a sphere. The event axis is the vector between the reconstructed event position and the detector centre. The sphere is then split into 4 longitudinal segments with each segment then split into 4 latitudinal regions. The segments are in equal $2\pi/4 = \delta\phi$ values, with the segments then split into equal $\cos\theta$ values. This results in regions as shown in figure 8.2. The regions are then expected to have equal hits, and a χ^2 test is used with an expected value equal to Nhit divided by the number of regions. This χ^2 result is then output to be cut on for pileup identification.

The technique as outlined above makes a number of unsafe assumptions that

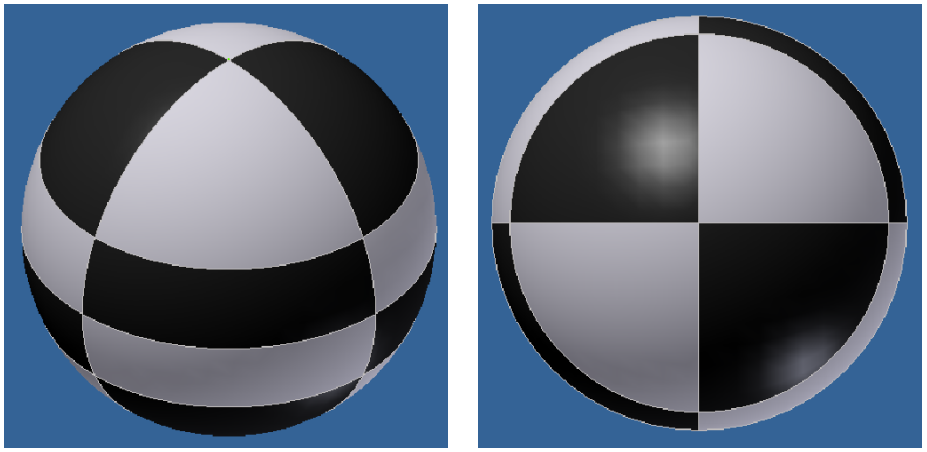

(a) Isometric view of the isotropic regions.

(b) Regions viewable when looking along the event axis. Note the 4 longitudinal regions.

Figure 8.2: Division of sphere into the regions for the isotropy technique.

can be accounted for. Firstly the SNO+ PMT coverage is not uniform, in particular the neck is directly, and via shadowing, a large gap in coverage. To account for this a segment sized such that the segment edges are 200mm larger than the neck i.e. the the segment is 2000mm wide when projected onto the neck AV bond, is defined. All hits in this segment are then ignored and the other segments are resized such that $\delta\phi = (2\pi - \phi_{neck})/4$. This directly removes the neck and neck shadowing from the technique; the shadowing is removed as the neck, event and segment centre are coplanar. Secondly attenuation reduces the number of photons reaching the PSUP further away from the interaction position relative to the near PSUP. For this reason a separate χ^2_{lat} result is also output; this is calculated for regions of equal latitude only, as regions of equal latitude will have equivalent travel distances from the interaction positions. The χ^2_{lat} results for the 4 sets of equal latitude regions are then averaged to give the final output value.

Classifier	Cut
Pre Trigger Hits	> 3
Timing Peaks	>1
NearAV	true
Fit Result	true
Early Hits	$0.03 < F_{Early} < 0.09$
Mean Time	$23.0 < \bar{t}_{emission} < 37.0$ns
Isotropy χ^2	> 60.0
Isotropy χ^2_{lat}	> 6.0

Table 8.1: Hard cut values for the pileup techniques.

8.6 Cut Values

The techniques described above produce numerical values which can be cut on to reject pileup. The cut values given in table 8.1 have been chosen to individually reject less than 10% of non pileup 3.5MeV electron events. These cut values are not optimised and have been chosen by eye.

8.7 Electron Performance

To test the performance of the pileup identification techniques and cuts a select combination of electron interactions have been simulated. These combinations tested the cuts on both pileup and non pileup electron interactions. Each event type was simulated 1000 times, with each event reconstructed using the emissionTime PDF and energyLookup, see chapter 6. The interactions were simulated to occur uniformly by volume in the scintillator, and if pileup the events were spaced uniformly over the 400ns window.

The simulated pileup events include many reconstructed events which are not pileup; for example, if the interaction separation in time is greater than 220ns for Type 1 events each interaction will reconstruct as a separate event. Furthermore, there are also events that reconstruct with an energy much less than the pileup energy, see section 8.8. In these situations the reconstructed event does not match

the SNO+ relevant definition of pileup as the event is not reconstructed in the signal region. Thus these events should not be counted in the pileup rejection efficiency.

I require an event to have a reconstructed energy within $\pm 1\sigma$ (as defined by the energyLookup fitter) of the simulated energy for it to be considered. With this definition it is clear that 68% (682) of the 1000 simulated single interaction events should reconstruct and pass the cuts in the ideal case. Whereas ideally zero pileup events will reconstruct and pass the cuts. The results shown in table 8.2, show the interactions in the events, number reconstructed and number post pileup cuts within $\pm 1\sigma$ of the summed interaction energy, and finally the percentage of the expected 682 to survive.

It is clear from table 8.2 that many fewer single interaction events survive reconstruction and pileup cuts than expected. This is because the reconstruction algorithms are not ideal and that near AV events are rejected. Given that 28% of the scintillator volume is near the AV and that the reconstruction algorithms are at least 90% efficient suggests only $0.9 \times 0.72 \times 682 = 441$ or 65% of events are expected to survive. This thus indicates that the pileup cuts have a very small effect on the single interaction events in comparison to reconstruction algorithm efficiency and near AV rejection. Furthermore the additional signal rejection at 1MeV of 70 events is much higher than the 16 events at 3.5MeV, as expected given the cuts are chosen to work at 3.5MeV, i.e. in the double beta signal region.

Table 8.2 also shows that very few pileup events survive reconstruction and fewer still survive the additional pileup cuts. Note that the reconstruction also serves as a pileup identifier. The target of greater than 99% rejection has been achieved for pileup events with with a ratio of energies falling between about 0.4 and 2.5. Pileup events with very unequal energy interactions are harder to identify as the smaller energy interaction can look like a statistical fluctuation on the larger energy interaction. Thus, the 3.5MeV pileup with 0.5MeV events are the hardest

True Energy [MeV]	Reconstructed	Post pileup Cuts	Survival %
1.0	344	274	40.2%
1.5	401	360	52.8%
2.0	531	488	71.6%
2.5	448	418	61.3%
3.0	486	459	67.3%
3.5	459	443	65.0%
4.0	451	430	63.0%
0.5 + 0.5	54	2	0.3%
1.0 + 0.5	71	3	0.4%
1.0 + 1.0	81	1	0.1%
1.0 + 1.5	61	1	0.1%
1.0 + 2.0	92	2	0.3%
1.0 + 2.5	71	4	0.6%
1.0 + 3.0	82	1	0.1%
1.5 + 0.5	82	10	1.5%
1.5 + 1.5	83	2	0.3%
1.5 + 2.0	71	3	0.4%
1.5 + 2.5	68	6	0.9%
2.0 + 0.5	82	9	1.3%
2.0 + 2.0	82	2	0.3%
2.5 + 0.5	142	24	3.5%
3.0 + 0.5	157	38	5.6%
3.5 + 0.5	186	42	6.2%

Table 8.2: Survival factors for electron single interaction and pileup events. Details in main text.

to reject, yet a greater than 90% rejection is achieved.

8.7.1 Example Detailed Events

The single pileup of 2MeV electrons with 1.5MeV electrons has a less than 1% survival fraction, after the application of the cuts given in table 8.1. The full 1000 simulated events are shown in figure 8.3, along with the technique that rejected the event. In figure 8.3, the techniques are ordered such that only the first technique to reject the event is drawn. This order is as table 8.1 and in the legend.

In figure 8.3 event rejection is dominated in the low Nhit region by the pre trigger hits technique. These events are predominantly type 3, i.e. consist of the

tail of E in figure 8.1. In the high Nhit region the event rejection is dominated by the timing peaks technique. These events are predominantly type 1 events, i..e consist of D and E in figure 8.1. The events that pass these techniques are predominantly rejected by the isotropy technique.

The isotropy technique is very useful as it is the only technique not based on timing; this allows it to reject events that pass the timing techniques. For example a type 1 A, B, C event may, combined with the geometric properties, have a very good timing spectrum and also be reconstructible, leaving only the isotropy technique able to reject these events.

8.7.2 Effect on the SNO+ Energy spectrum

Including the rejection factors in table 8.2 in the SNO+py software gives the energy spectra in figure 8.4. The end point spectra shown in figure 8.4(b) is devoid of all but the ^{138}La with ^{138}La single pileup background. This indicates that less than 1 event per year is expected for the other pileup backgrounds. This is a much better outcome than figure 7.4(b) indicating that the pileup rejection is very effective.

The additional rejection of near AV events and losses from reconstruction efficiency means the ideal case, figure 7.3(b), is not achievable.

8.8 Reconstructed Energy

The energy of an event is reconstructed using the sum of the PMT hits (Nhit) within the event window. The Nhit value is then converted into an equivalent electron energy, using the expected Nhit values for electrons see section 6.7. Hence for an accepted pileup event the energy is proportional to the sum of PMT hits from all the interactions, within the window.

Pileup events have interactions at different times within the trigger window, leading to hits being truncated, as E in figure 8.1. Thus the Nhit contribu-

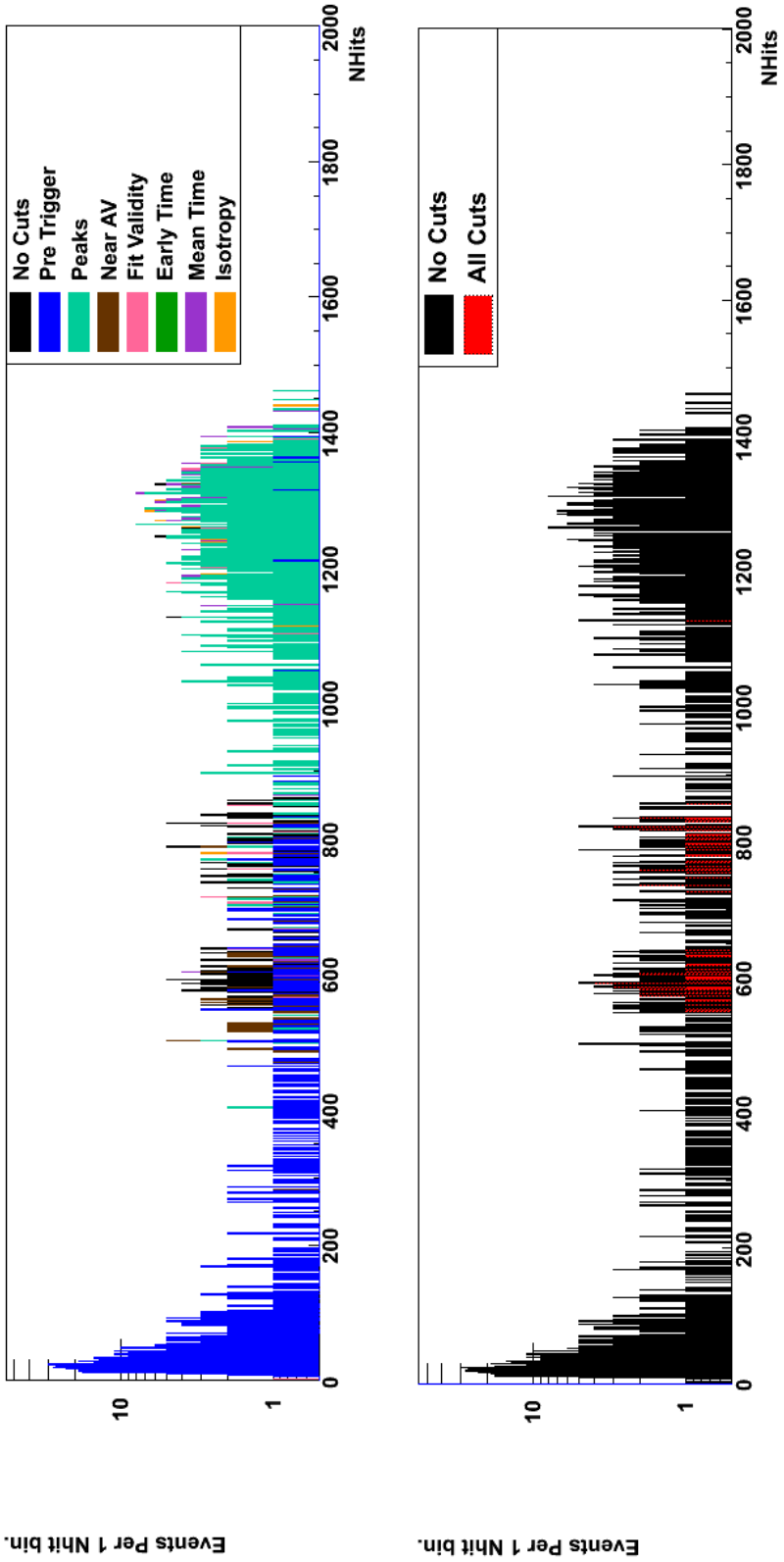

Figure 8.3: 2MeV with 1.5MeV electron pileup rejection. The upper plot shows the event count versus Nhit with shading indicating the first technique to reject the event. The technique ordering is shown in the legend. The lower plot shows the event count versus Nhit for pre rejected, black and post rejected, red, events. The lower plot shows events surviving all the cuts (red) in the 600Nhit (1.5MeV) and 800Nhit (2.0MeV) domains, and almost no events in the full energy pileup region 1300Nhit.

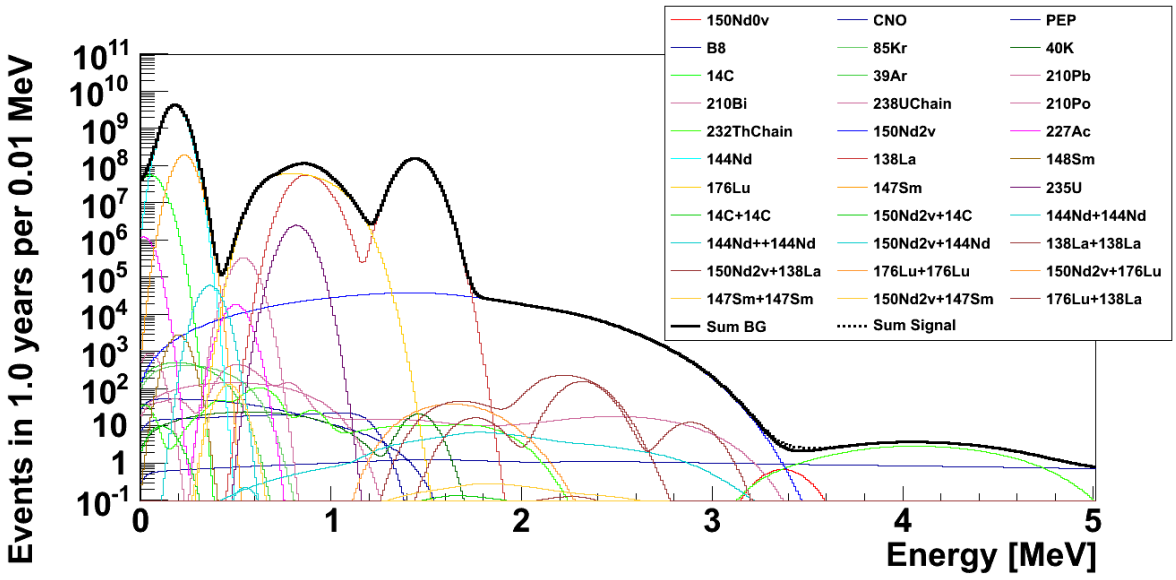

(a) Spectra over the full energy domain

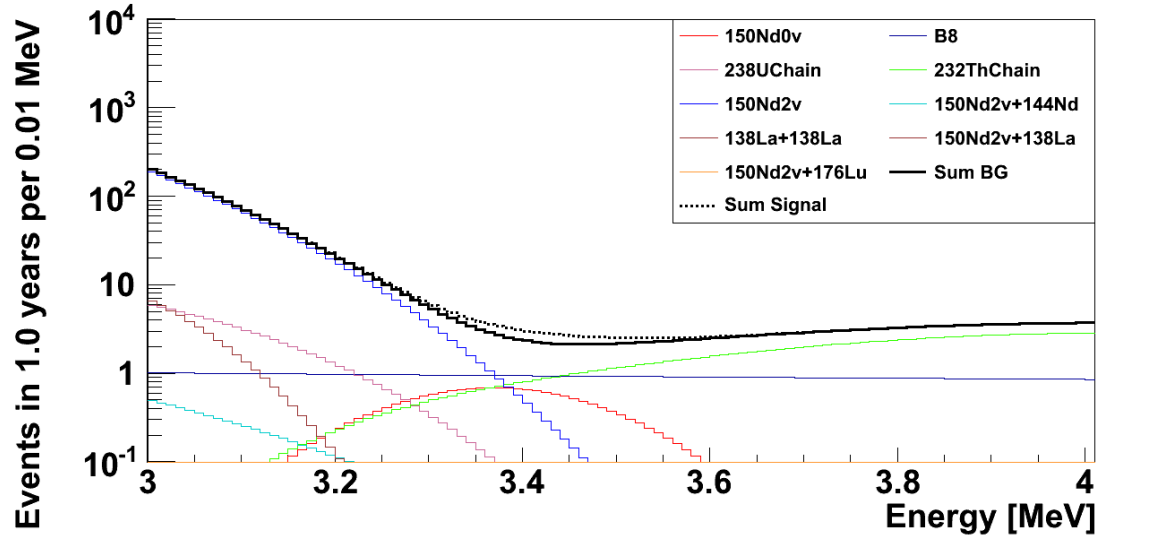

(b) Spectra in the signal region

Figure 8.4: Expected energy spectra generated by SNO+py to simulate the SNO+ detector. This corresponds to a year of running 0.1% loaded Nd scintillator with pileup spectra calculated. Rates used are those from table 7.4. Each spectrum is convoluted with the energyLookup energy resolution given in section 6.7.1. Further pileup and signal rejection is applied using the values in table 8.2.

tion from truncated interactions will be less than expected for a single event (no truncation). This lowers the effective energy of the pileup event such that $E_{Effective} \leq \sum_i E_{Interaction,i}$.

For two above trigger threshold interactions separated by 60ns, this will lead to 10% of the second interaction's hits being truncated. This rises to 10% for a 150ns separation, 25% for 190ns and 50% for 220ns. Assuming the secondary events are uniformly distributed in time, this leads to an average 10 to 20% decrease in recorded hits in the secondary event.

8.9 Monte Carlo Results

Section 7.2 identifies seven pileup backgrounds in the double beta decay signal region. The electron performance results given above suggests that these backgrounds will be almost entirely removed by the pileup rejection techniques. To confirm this I have simulated each pileup background in RAT, with the results shown below. The events are simulated with random positions weighted by volume in the scintillator. The pileup window simulated is 400ns in all cases, furthermore the Monte Carlo summed kinetic energy is constrained to lie between 3.0 and 4.0MeV, i.e. the signal region.

Firstly 1000 $2\beta0\nu$ signal events were simulated, with the reconstructed spectrum shown in figure 8.5. Of the 1000 events 701 were reconstructed with an energy between 3.0 and 4.0MeV. This is as expected, as up to 280 (28%) should be identified as near the AV and not reconstructed, and a further approximately 10% will fail reconstruction. The pileup cuts reject a further 40 events, leaving 661 events or 66.1% post pileup cuts. This is entirely consistent with the rejection for electrons, see table 8.2.

Next, 50000 single pileup of ^{138}La with $2\beta2\nu$ events were simulated, with the reconstructed spectrum shown in figure 8.6. Of the 50000 events only 6640 were reconstructed in the signal region, which shows the effectiveness of the reconstruction algorithm as a pileup indicator. The pileup cuts reject a further 4265 events, leaving 2375 events or 4.7% post pileup cuts. The large survival fractions seen

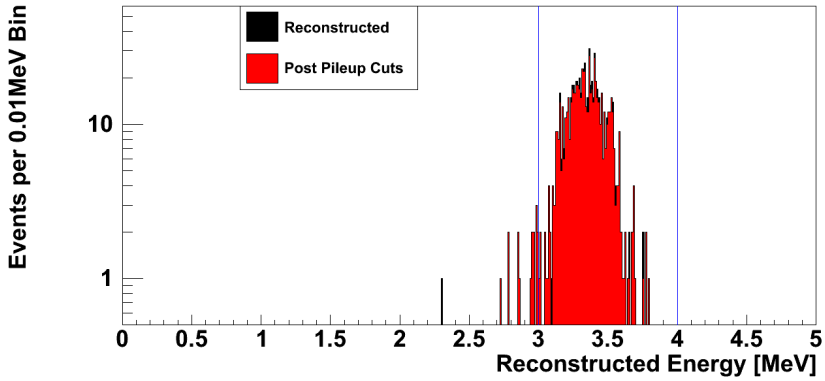

Figure 8.5: Simulated $2\beta0\nu$ spectrum, as reconstructed in black, post pileup cuts in red. The signal region is shown between the blue lines.

at 0.7MeV and 1.4MeV in figure 8.6, consist of an ^{138}La interaction and very few hits from the corresponding $2\beta2\nu$ interaction. Whereas the large survival fraction seen between 2.5MeV and 3.5MeV is the opposite situation. This will occur for events separated by over 220ns, as these are type 1 events.

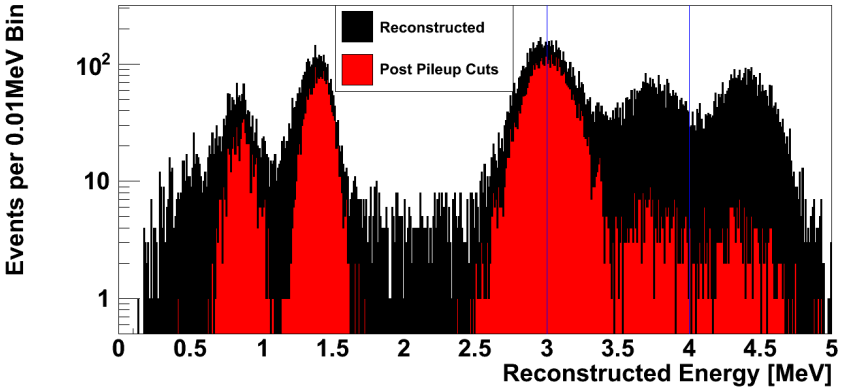

Figure 8.6: Simulated La+Nd single pileup spectrum, as reconstructed in black, post pileup cuts in red. The signal region is shown between the blue lines.

Next, 50000 single pileup of ^{176}Lu with $2\beta2\nu$ events were simulated, with the reconstructed spectrum shown in figure 8.7. Of the 50000 events only 10682 were reconstructed in the signal region. The pileup cuts reject a further 8799 events, leaving 1883 events or 3.7% post pileup cuts. The large survival fraction seen at 0.7MeV in figure 8.7, consist of an ^{176}Lu interaction and very few hits from the

corresponding $2\beta2\nu$ interaction. Whereas the large survival fraction seen between 2.5MeV and 3.5MeV is the opposite situation.

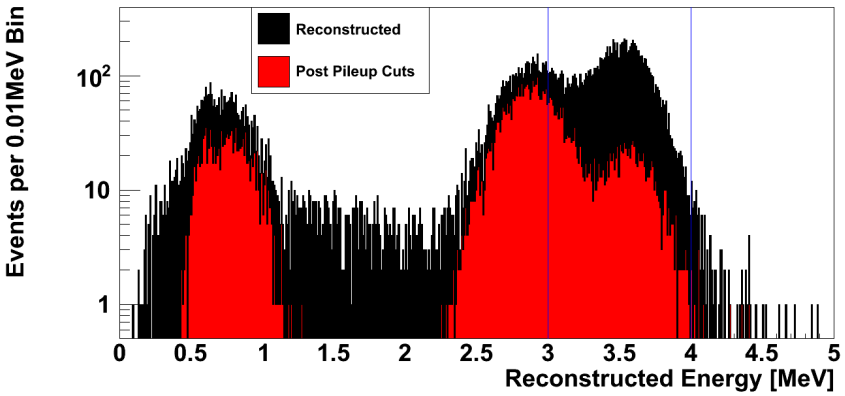

Figure 8.7: Simulated Lu+Nd single pileup spectrum, as reconstructed in black, post pileup cuts in red. The signal region is shown between the blue lines.

Next, 5000 double pileup of ^{138}La events were simulated, with the reconstructed spectrum shown in figure 8.8. Of the 5000 events only 95 were reconstructed in the signal region. The pileup cuts reject a further 95 events, leaving 0 events.

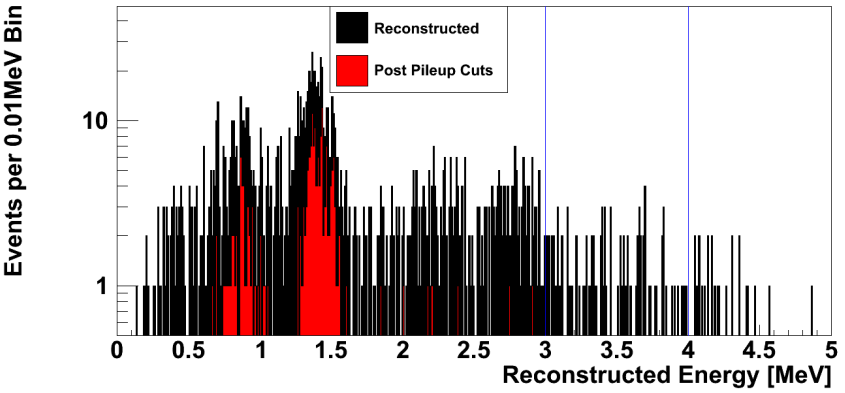

Figure 8.8: Simulated La double pileup spectrum, as reconstructed in black, post pileup cuts in red. The signal region is shown between the blue lines.

The single pileup of ^{138}La was also simulated; of 5000 simulated events there are no events in the signal region post pileup cuts.

8.10 Conclusion

Both the electron-only simulation and actual background simulation give consistent results for single pileup, summarised in table 8.2. Whereas, the actual background simulation also suggests that double pileup rejection is more efficient than single. These rejection factors are easily sufficient to negate any pileup concerns for the double beta phase, as seen in figure 8.4(b).

Chapter 9

Experimental Sensitivity

The SNO+ preferred limit setting technique is presented. The necessity and effect of pileup rejection on the limits is shown. The limits are then discussed in context of the competing experiments and improvements are suggested.

In general neutrinoless double beta decay experiments present a limit on the Majorana mass that have or can be achieved under certain assumptions. Therefore I will also show limits on both the half-life of the isotope and Majorana mass of the neutrino.

9.1 Limit Setting

The sensitivity of neutrinoless double beta decay experiments is conventionally expressed as a limit on the half-life or mass that can be excluded by the experiment in the absence of signal. The limit is set by an exclusion of the signal plus background model at a certain level via a statistical technique. For this thesis I will use the preferred SNO+ technique; the CLs technique which was developed at and for the LEP experiments, see [89].

The CLs technique quantifies the data as signal or background via the test statistic X, this statistic is the likelihood ratio of the alternative hypothesis to

null hypothesis. As the experiment expects a low number of counts, both likelihoods are given by the Poisson distribution. The test statistic X_i for an expected background b_i, observed counts d_i and proposed signal counts s_i is:

$$X_i = \frac{(s_i + b_i)^{d_i} \cdot e^{-(s_i+b_i)}}{d_i!} \Big/ \frac{(b_i)^{d_i} \cdot e^{-(b_i)}}{d_i!} \tag{9.1}$$

$$Q_i = -2 \ln X_i \tag{9.2}$$

$$Q_i = 2 \left(s_i - d_i \ln \frac{s_i + b_i}{b_i} \right) \tag{9.3}$$

The Q_i test statistic is often used for computational speed, and accuracy. The test statistic can then be extended over multiple channels, i.e. bins in the binned data, background and signal set.

$$X = \prod_i^N X_i \tag{9.4}$$

$$Q = \sum_i^N Q_i \tag{9.5}$$

This gives a significant improvement in exclusion over the simple counting statistic for a single channel.

For the proposed signal model, expected background and observed data a test statistic X_{obs} can be calculated. The confidence level, CL_{s+b} in the alternative (signal plus background) hypothesis is given by:

$$\mathrm{CL}_{s+b} = P_{s+b}(X \leq X_{obs}) = \int_{-\infty}^{X_{obs}} \frac{dP_{s+b}}{dX} dX \tag{9.6}$$

Small values of CL_{s+b} indicate a poor compatibility with the signal plus background hypothesis. The CL_{s+b} confidence level can be used to set limits on s such that $\mathrm{CL}_{s+b} = \alpha$, where $\alpha = 0.1$ for 90% confidence. However, if the observed data is less than the expected background any signal (i.e. no signal) can be excluded at a higher confidence level.

A solution to this non physical (negative) preferred signal problem is to also consider the confidence in the null hypothesis as well. The CL_b is given by:

$$\mathrm{CL}_b = P_b(X \leq X_{obs}) = \int_{-\infty}^{X_{obs}} \frac{dP_b}{dX} dX \tag{9.7}$$

Values approaching 1 of CL_b indicate poor compatibility with the background hypothesis. Renormalising the CL_{s+b} by CL_b gives the modified frequentist CL_s confidence:

$$\mathrm{CL}_s = \frac{\mathrm{CL}_{s+b}}{\mathrm{CL}_b} \tag{9.8}$$

In the case of a single channel this is equivalent to the Helene Zech approach and the Bayesian credible level with an uniform prior[90].

The 90% confidence level observed limit on the signal using the CL_s method is calculated by varying s until $\mathrm{CL}_s = 0.1$. This calculation must be done numerically, typically with the Q test statistic. As CL_s is not a true confidence level it does not strictly conform to the frequentist confidence level, however it results in a greater coverage probability. The CL_s approach can be considered more conservative[90].

The above discussion focuses on the observed limit given some data, however SNO+ as yet has no data. Therefore an expected limit can be calculated based on the expected background, to indicate the potential sensitivity of the experiment. This is done by assuming the potential data will be background alone and thus setting the data equal to background in the test statistic. As with the observed limit the signal s is varied until $\mathrm{CL}_s = 0.1$. The CL_s is typically termed $\langle \mathrm{CL}_s \rangle$ under the background alone assumption.

To account for different experiments having different background fluctuations, the $\langle \mathrm{CL}_s \rangle$ is evaluated with differing data values based on the background. The value of s for data equal to the background is the median exclusion limit, i.e. 50% of experiments will report this limit or better. The data is then varied by $\pm 2\sigma$ and $\pm 1\sigma$, where σ is the uncertainty on the background. The s values between

the $\pm 2\sigma$ values indicate the range of limits 95% experiments will set, and the $\pm 1\sigma$ indicate the limit 68% of experiments will set.

9.2 Expected Limits

The SNO+py software incorporates the CL_s technique described above. Combined with the background information given in chapter 7, energy resolution given in chapter 6, the rejection factors given in chapter 8, and 0.1% neodymium loading, allow limits to be calculated as a function of livetime. As discussed in chapter 7, the external backgrounds will be neglected and a fiducial volume of 50% applied. The half-life upper limit at 90% CL will be calculated and converted into a Majorana mass lower limit at 90% CL using the values given in section 1.3.1. I will quote the median limit where a single number is required.

Firstly the half-life and mass limits for SNO+ with no pileup rejection and perfect reconstruction efficiency are shown in figures 9.1(a) and 9.1(b) respectively. After four years of livetime a half-life lower limit of 3.3×10^{24}yr and mass upper limit of 280meV can be achieved.

Incorporating the pileup rejection and with it the realistic reconstruction efficiency, the half-life and mass limits improve to those shown in figures 9.2(a) and 9.2(b) respectively. This improves the four year livetime half-life limit to 5.1×10^{24}yr and the mass limit to 220meV. This demonstrates that the pileup rejection and event reconstruction techniques developed in this thesis succeed in improving the achievable SNO+ limit.

To quantify the performance of the pileup rejection and event reconstruction techniques, I have also calculated the half-life and mass limits for no pileup background and perfect reconstruction efficiency, as shown in figures 9.3(a) and 9.3(b) respectively. These plots show a four year livetime half-life limit of 5.76×10^{24}yr and mass limit of 210meV. This is slightly (1.1 times) better than with pileup

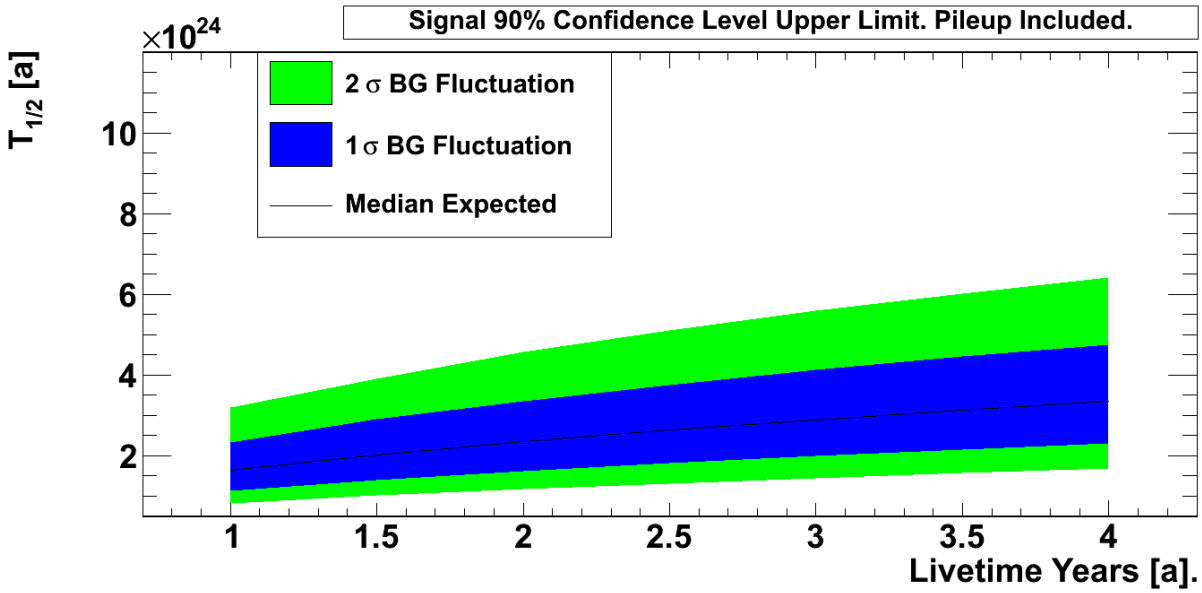

(a) Half-Life Limit

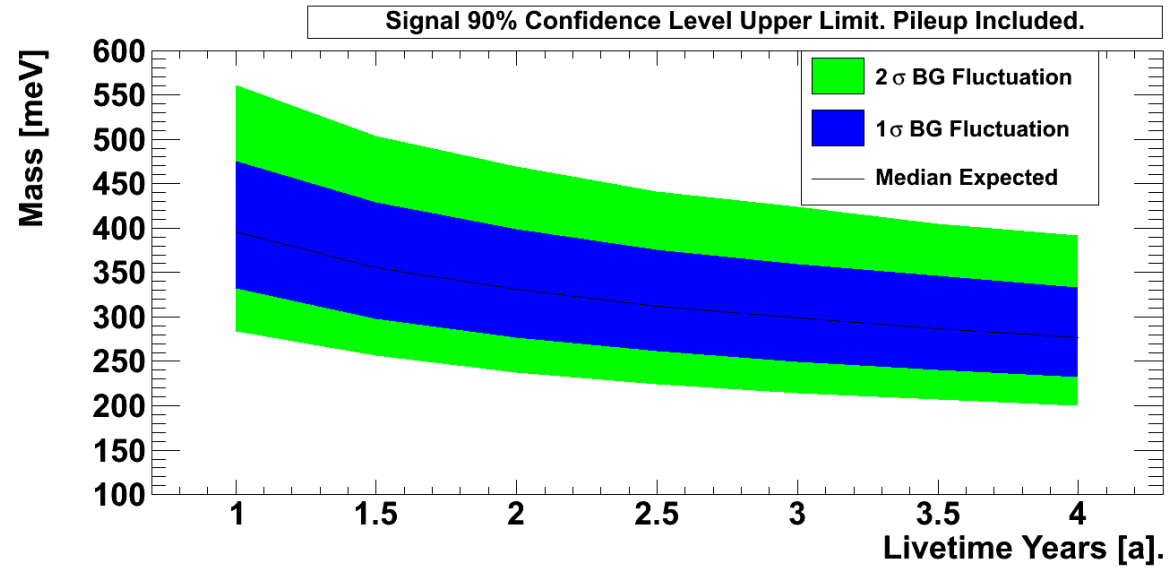

(b) Majorana mass limit

Figure 9.1: 90% Confidence Level limits for perfect reconstruction efficiency and pileup backgrounds without rejection.

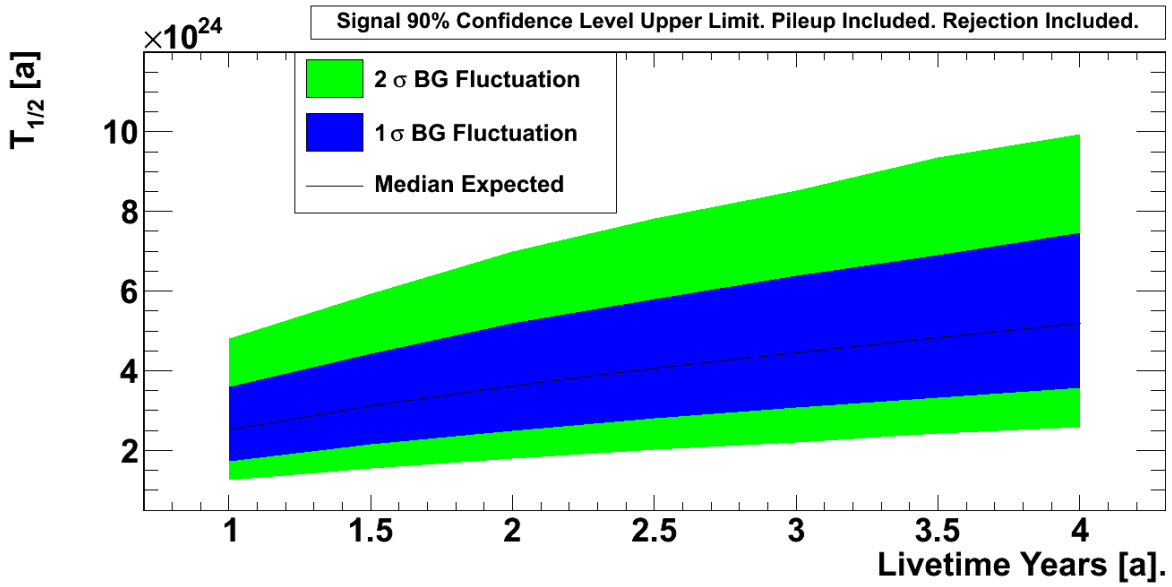

(a) Half-Life Limit

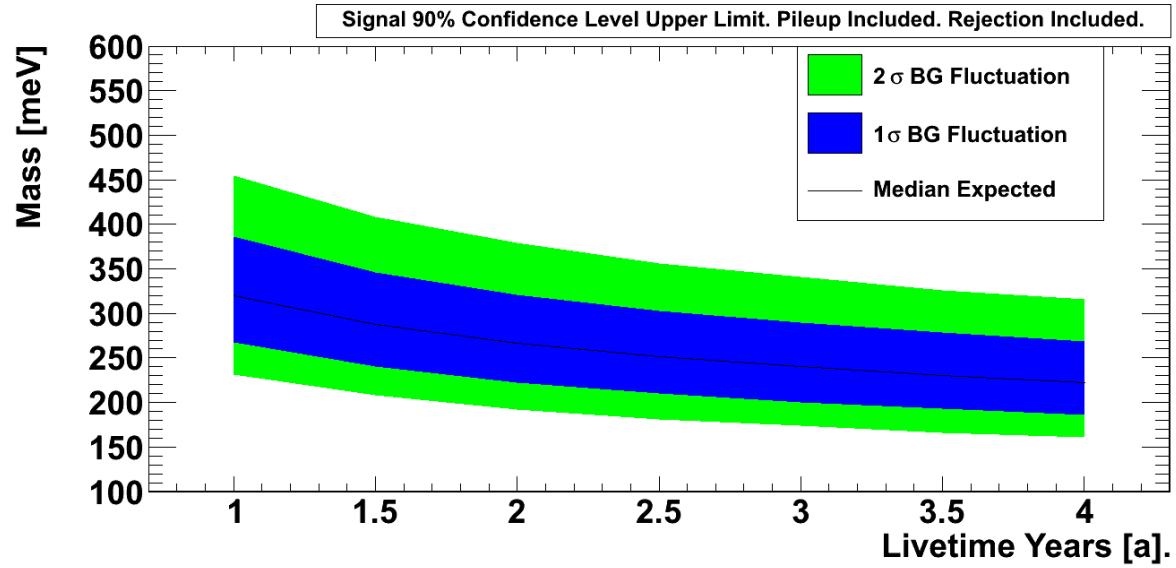

(b) Majorana mass limit

Figure 9.2: 90% Confidence Level limit for realistic reconstruction efficiency and pileup backgrounds with rejection.

rejection and realistic reconstruction efficiency.

In summary the pileup rejection algorithms work very well at improving the SNO+ achievable limit. This performance could be improved by raising the reconstruction efficiency by optimising the pileup cuts. This is something I plan to do in the future.

9.3 Limits in context

The SNO+ double beta phase is expected to start data taking in 2013, thereby giving two livetime years before 2015[1]. In that time an upper limit of 260meV is likely to be set by SNO+. This limit is far below the Klapdor-Kleingrothaus claim of 320meV, and thus SNO+ will test this claim by 2015.

As discussed in section the competitors to SNO+ in 2015 are likely to be EXO, CUORE, SuperNEMO, GERDA, and KamLAND-Zen. These experiments expect to set upper limits of 90meV, 370meV, 320meV, 310meV, and 80meV within a year of 2015. Thus SNO+ in its current state is competitive but not world leading.

9.4 Improvements

As the current SNO+ plan will not set a world beating limit on neutrinoless double beta decay, these are some suggestions to improve the experiment. Firstly the limits shown have a conservative fiducial volume cut (50%) to remove external backgrounds. This fiducial volume could be increased if these backgrounds are well understood, improving the limit. Work to identify these backgrounds using the special optical properties is ongoing, for example gamma beta decays in the AV produce extra Čerenkov light which can be identified separately to the accompanying scintillator light. However, even using the entire volume without

[1]This is in the ideal case, in reality only 80% of calender time is likely to be spent taking data.

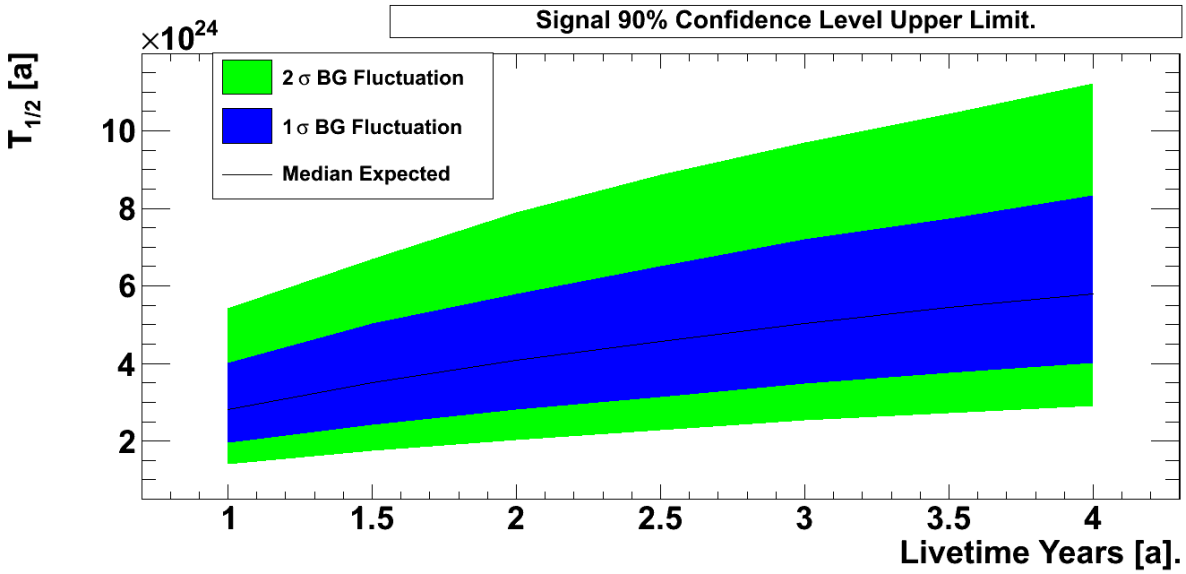

(a) Half-Life Limit

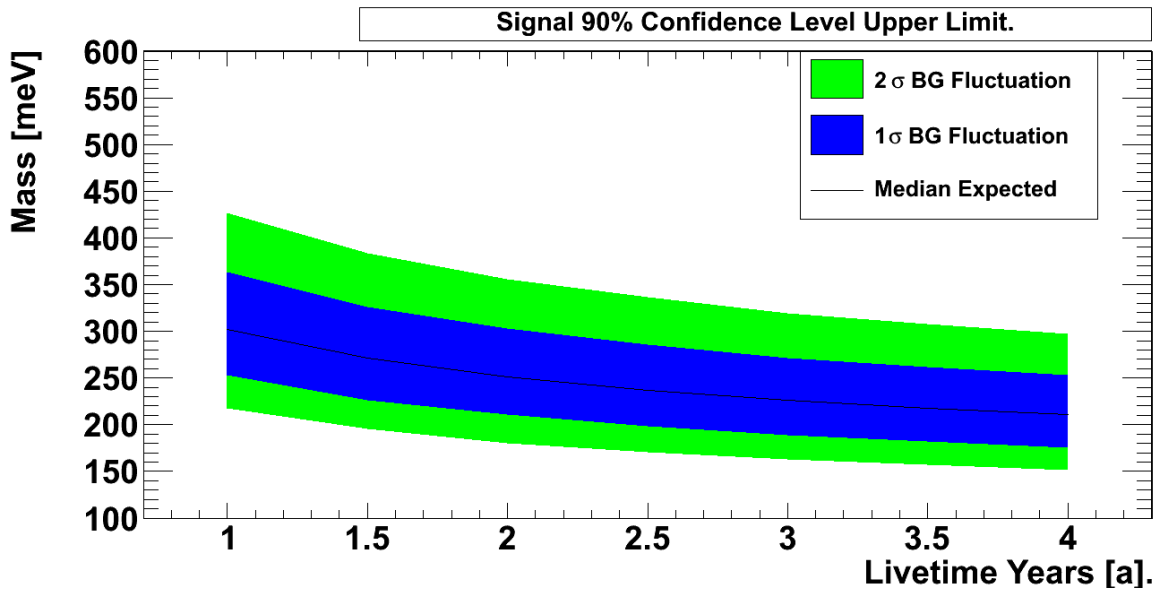

(b) Majorana mass limit

Figure 9.3: 90% Confidence Level limit for perfect reconstruction efficiency and no pileup backgrounds (e.g. if Nd-related backgrounds can be removed by purification such that pileup is negligible).

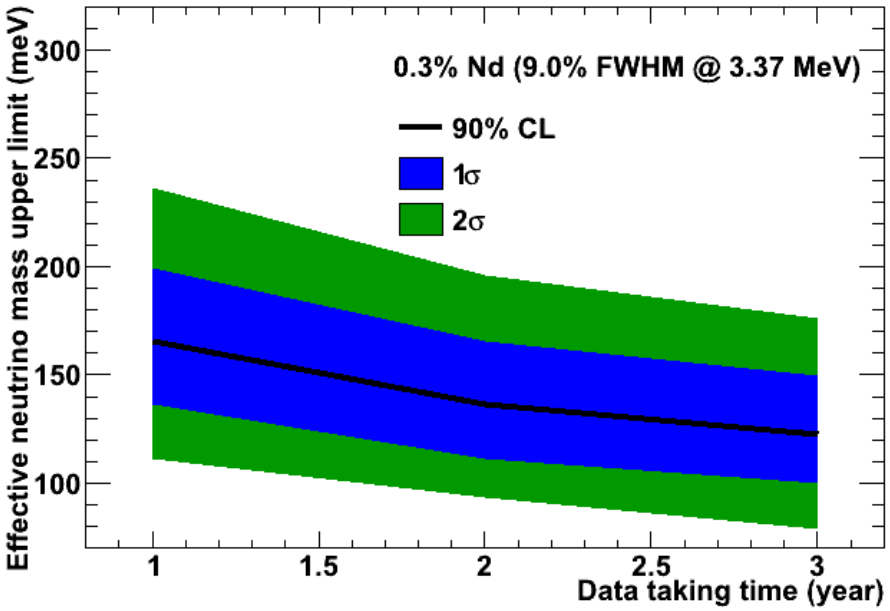

Figure 9.4: Ideal 0.3% Nd loading limit with perfect reconstruction efficiency and no pileup, as calculated by N Fatemi-Ghomi[92].

any increase in the background will improve the half-life limit by a factor $\sqrt{2}$ (see equation 1.13) and the Majorana mass limit by $\sqrt[4]{2}$. Therefore only a small gain can be found be increasing the fiducial volume.

A better method is to load more neodymium and thus increase the mass of the isotope. This is something the collaboration has discussed and S Biller *et al.* have shown that 0.3% loading is the optimum level[91] for SNO+. At 0.3% loading with perfect reconstruction efficiency and no pileup backgrounds the limit reduces to $m_{\beta\beta} \leq 140$meV by 2015 as shown in figure 9.4 from [92]. Different assumptions about energy resolution and matrix elements were used in this study, and pileup was absent.

Finally I suggest that the SNO+ collaboration further explores enrichment of neodymium. Enrichment will likely require an Atomic Vapour Laser Isotope Separation, AVLIS, facility. The AVLIS process relies on the difference in atomic electron energy levels due to different hyperfine splitting due to the different num-

ber of nucleons. Tuning the laser to an atomic energy level for the isotope of interest allows the laser to ionise only that isotope, and hence the resultant charge difference can be used to separate the isotopes.

An enrichment factor of 16, taking the ^{150}Nd fraction up from 5.6% to 90%, would improve the half-life sensitivity by a factor of 4, and the mass sensitivity by a factor of 2. Even at 0.1% loading this will allow SNO+ to set a limit with realistic reconstruction efficiency and pileup at around 130meV by 2015, and potentially 70meV for 0.3% loading. This is a very competitive limit in comparison with the other neutrinoless double beta decay experiments.

9.5 Conclusion

The improvements to RAT detailed in this thesis will enable SNO+ to more accurately simulate the SNO+ detector and experiment. Furthermore, these improvements have been shown to reproduce the SNO Monte Carlo which itself was calibrated to SNO data. This enables the reconstruction and pileup rejection techniques detailed to be used to more accurately predict the sensitivity of SNO+ to double beta decay.

Appendix A

Radioactive decay chains of ^{238}U and ^{232}Th

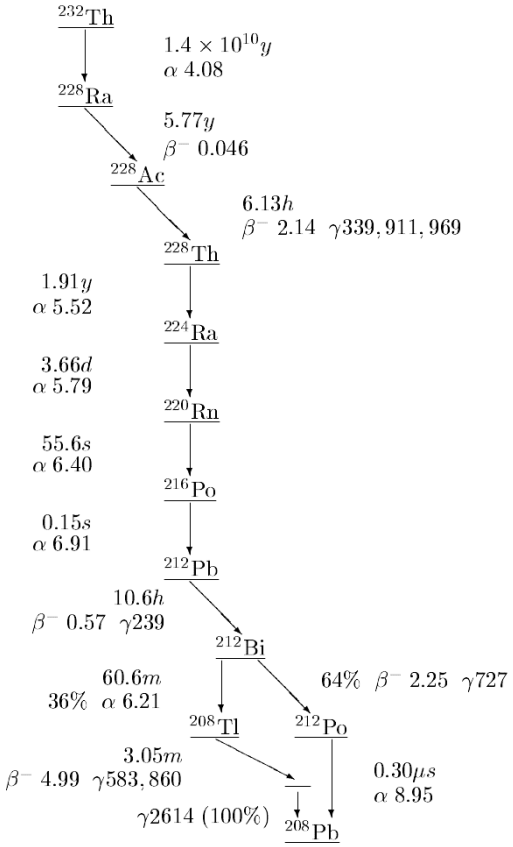

Figure A.1: ^{232}Th decay chain. Half lives, Q-values of beta and alpha decays in MeV, and gamma rays in keV are shown. Figure from [88].

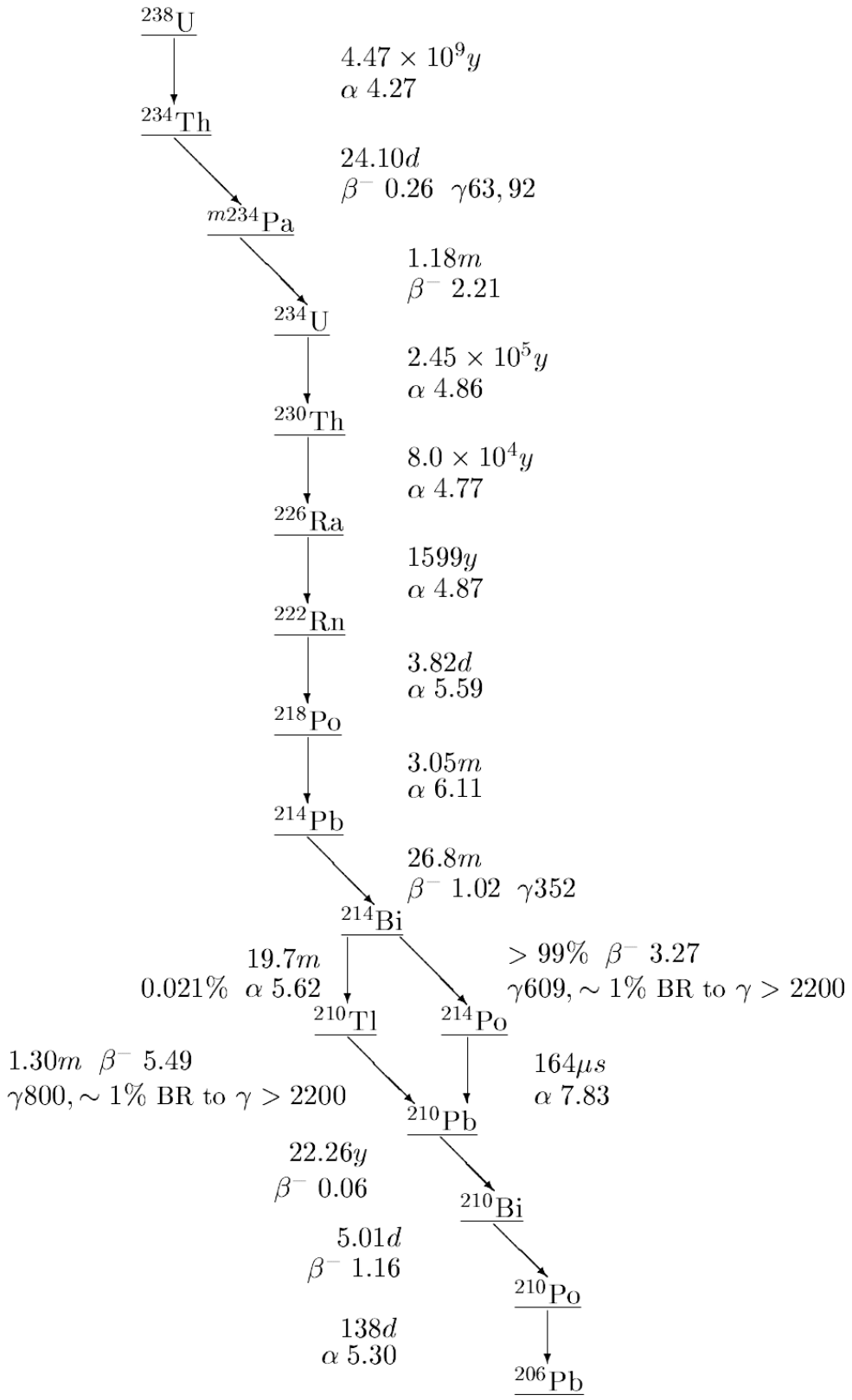

Figure A.2: ^{238}U decay chain. Half lives, Q-values of beta and alpha decays in MeV, and gamma rays in keV are shown. Figure from [88].

Appendix B

Photocathode Optical Equations

B.1 Fresnel Transmission/Reflection

The Fresnel reflection and Transmission equations are, note that $n_{1,2}$ may be complex:

$$\cos\theta_i = \vec{d}\cdot\vec{n} \tag{B.1}$$

$$\cos\theta_t = \sqrt{1-(\frac{n_1}{n_2})^2 * (1-\cos{\theta_i}^2)} \tag{B.2}$$

$$R_s = \left(\frac{n_1\cos\theta_i - n_2\cos\theta_t}{n_1\cos\theta_i + n_2\cos\theta_t}\right)^2 \tag{B.3}$$

$$R_p = \left(\frac{n_1\cos\theta_t - n_2\cos\theta_i}{n_2\cos\theta_i + n_1\cos\theta_t}\right)^2 \tag{B.4}$$

$$T_s = \left|\frac{4(n_2)^2\cos{\theta_i}^2\frac{n_1}{n_2}}{(n_1\cos\theta_i + n_2\cos\theta_t)^2}\right| \tag{B.5}$$

$$T_s = \left|\frac{4(n_2)^2\cos{\theta_i}^2\frac{n_1}{n_2}}{(n_1\cos\theta_t + n_2\cos\theta_i)^2}\right| \tag{B.6}$$

To get the actual transmission/refraction probability the above are combined with $s_{fraction}$ (as calculated previously) to give:

$$R = s_{fraction} * R_s + (1 - s_{fraction}) * R_p \quad \text{(B.7)}$$

$$T = s_{fraction} * T_s + (1 - s_{fraction}) * T_p \quad \text{(B.8)}$$

$$A = 1 - T - R \quad \text{(B.9)}$$

B.2 Thin film Transmission/Reflection

For a thin film with complex refractive index n_2 between media n_1 and n_3 of thickness t and a photon with wavelength λ, the reflection and transmission coefficients are:

$$\cos\theta_1 = \vec{d} \cdot \vec{n} \quad \text{(B.10)}$$

$$\cos\theta_2 = \sqrt{1 - (\frac{n_1}{n_2})^2(1 - \cos{\theta_1}^2)} \quad \text{(B.11)}$$

$$\cos\theta_2 = \sqrt{1 - (\frac{n_1}{n_3})^2(1 - \cos{\theta_1}^2)} \quad \text{(B.12)}$$

$$\eta = 2\pi t/\lambda \quad \text{(B.13)}$$

$$u = \Re(n_2 \cos\theta_2) \quad \text{(B.14)}$$

$$v = \Im(n_2 \cos\theta_2) \quad \text{(B.15)}$$

Note that t is a function of the photon z coordinate in the PMT coord system, and is defined in the model parameters. For s polarised photons:

$$r_{12} = \frac{n_1 \cos\theta_1 - n_2 \cos\theta_2}{n_1 \cos\theta_1 + n_2 \cos\theta_2} \quad \text{(B.16)}$$

$$r_{23} = \frac{n_2 \cos\theta_2 - n_3 \cos\theta_3}{n_2 \cos\theta_2 + n_3 \cos\theta_3} \quad \text{(B.17)}$$

$$t_{12} = \frac{2n_1 \cos\theta_1}{n_1 \cos\theta_1 + n_2 \cos\theta_2} \quad \text{(B.18)}$$

$$t_{23} = \frac{2n_2 \cos\theta_2}{n_2 \cos\theta_2 + n_3 \cos\theta_3} \quad \text{(B.19)}$$

$$g = \frac{n_3 \cos\theta_3}{n_1 \cos\theta_1} \quad \text{(B.20)}$$

For p polarised photons:

$$r_{12} = \frac{n_2 \cos\theta_1 - n_1 \cos\theta_2}{n_2 \cos\theta_1 + n_1 \cos\theta_2} \quad \text{(B.21)}$$

$$r_{23} = \frac{n_3 \cos\theta_2 - n_2 \cos\theta_3}{n_3 \cos\theta_2 + n_2 \cos\theta_3} \quad \text{(B.22)}$$

$$t_{12} = \frac{2n_1 \cos\theta_1}{n_2 \cos\theta_1 + n_1 \cos\theta_2} \quad \text{(B.23)}$$

$$t_{23} = \frac{2n_2 \cos\theta_2}{n_3 \cos\theta_2 + n_2 \cos\theta_3} \quad \text{(B.24)}$$

$$g = \frac{n_3 \cos\theta_3}{n_1 \cos\theta_1} \quad \text{(B.25)}$$

Then:

$$R_s = \frac{\mid r_{12} \mid^2 e^{2v\eta} + \mid r_{23} \mid^2 e^{-2v\eta} + 2 \mid r_{12} \mid\mid r_{23} \mid \cos 2u\eta + arg(r_{23}) - arg(r_{12})}{e^{2v\eta} + \mid r_{12} \mid^2 \mid r_{23} \mid^2 e^{-2v\eta} + 2 \mid r_{12} \mid\mid r_{23} \mid \cos 2u\eta + arg(r_{23}) + arg(r_{12})} \quad \text{(B.26)}$$

$$T_s = \frac{\Re(g) \mid t_{12} \mid^2 \mid t_{23} \mid^2}{e^{2v\eta} + \mid r_{12} \mid^2 \mid r_{23} \mid^2 e^{-2v\eta} + 2 \mid r_{12} \mid\mid r_{23} \mid \cos 2u\eta + arg(r_{23}) + arg(r_{12})} \quad \text{(B.27)}$$

Note the only difference between s and p polarised is the r_{12}, r_{23}, t_{12}, t_{23} values. To get the actual transmission/refraction probability the above are combined with

$s_{fraction}$ (as calculated previously) to give:

$$R = s_{fraction} * R_s + (1 - s_{fraction}) * R_p \tag{B.28}$$

$$T = s_{fraction} * T_s + (1 - s_{fraction}) * T_p \tag{B.29}$$

$$A = 1 - T - R \tag{B.30}$$

Bibliography

[1] C. D. Ellis *Proc Royal Soc.* **A99** (1921) 261.

[2] C. D. Ellis and W. A. Wooster, "The average energy of disintegration of radium e," *Proc Royal Soc.* **A117** (1927) 109.

[3] W. Pauli, "Letter, addressed to participants of the Tübingen conference on radioactivity," Dec, 1930. Available from the CERN Document server: `http://cdsweb.cern.ch/record/83282P`.

[4] J. Chadwick, "Possible existence of a neutron," *Nature.* **129** (1932) 312.

[5] F. Perrin *Comptes Rendus* **197** (1933) 1625.

[6] E. Fermi *Z. Phys.* **88** (1934) 161–177.

[7] H. Bethe and R. Peierls, "The neutrino," *Nature.* **133** (1934) 532–533.

[8] R. Davis, "Attempt to detect the antineutrinos from a nuclear reactor by the $Cl^{37}(\overline{\nu}, e^{-})A^{37}$ reaction," *Phys. Rev.* **97** no. 3, (Feb, 1955) 766–769.

[9] E. J. Konopinski and H. M. Mahmoud, "The universal fermi interaction," *Phys. Rev.* **92** no. 4, (Nov, 1953) 1045–1049.

[10] M. Goldhaber, L. Grodzins, and A. W. Sunyar, "Helicity of neutrinos," *Phys. Rev.* **109** no. 3, (Feb, 1958) 1015–1017.

[11] G. Danby, J.-M. Gaillard, K. Goulianos, L. M. Lederman, N. Mistry, M. Schwartz, and J. Steinberger, "Observation of high-energy neutrino reactions and the existence of two kinds of neutrinos," *Phys. Rev. Lett.* **9** no. 1, (Jul, 1962) 36–44.

[12] M. N. Z. Maki and S. Sakata *Prog. Theo. Physics* **28** (1962) 247.

[13] B. Pontecorvo, "Neutrino experiments and the question of leptonic-charge conservation," *Sov. Phys. JETP* **26** (1968) 984–988.

[14] R. Davis, D. S. Harmer, and K. C. Hoffman, "Search for neutrinos from the sun," *Phys. Rev. Lett.* **20** (1968) 1205–1209.

[15] I. collaboration] **Munich 1988, Proceedings, High energy physics** (1988) 1305–1306.

[16] K.-I. collaboration] *Phys. Lett.* **B205** (1988) 416.

[17] M. L. Perl, G. S. Abrams, A. M. Boyarski, M. Breidenbach, D. D. Briggs, F. Bulos, W. Chinowsky, J. T. Dakin, G. J. Feldman, C. E. Friedberg, D. Fryberger, G. Goldhaber, G. Hanson, F. B. Heile, B. Jean-Marie, J. A. Kadyk, R. R. Larsen, A. M. Litke, D. Lüke, B. A. Lulu, V. Lüth, D. Lyon, C. C. Morehouse, J. M. Paterson, F. M. Pierre, T. P. Pun, and P. A. Rapidis, "Evidence for anomalous lepton production in $e^+ - e^-$ annihilation," *Phys. Rev. Lett.* **35** no. 22, (Dec, 1975) 1489–1492.

[18] "Precision electroweak measurements on the z resonance," *Physics Reports* **427** no. 5-6, (2006) 257 – 454.

[19] **DONUT** Collaboration, K. Kodama *et al.*, "Observation of tau neutrino interactions," *Phys. Lett.* **B504** (2001) 218–224.

[20] **Super-Kamiokande** Collaboration, Y. Fukuda *et al.*, "Measurement of a small atmospheric nu/mu / nu/e ratio," *Phys. Lett.* **B433** (1998) 9–18, arXiv:hep-ex/9803006.

[21] **Super-Kamiokande** Collaboration, Y. Fukuda *et al.*, "Study of the atmospheric neutrino flux in the multi-GeV energy range," *Phys. Lett.* **B436** (1998) 33–41, arXiv:hep-ex/9805006.

[22] **SNO** Collaboration, Q. R. Ahmad *et al.*, "Direct evidence for neutrino flavor transformation from neutral-current interactions in the Sudbury Neutrino Observatory," *Phys. Rev. Lett.* **89** (2002) 011301, arXiv:nucl-ex/0204008.

[23] **T2K** Collaboration, K. Abe *et al.*, "Indication of Electron Neutrino Appearance from an Accelerator-produced Off-axis Muon Neutrino Beam," *Phys. Rev. Lett.* **107** (2011) 041801, arXiv:1106.2822 [hep-ex].

[24] K. Nakamura and P. D. Group, "Review of particle physics," *Journal of Physics G: Nuclear and Particle Physics* **37** no. 7A, (2010) 075021.

[25] V. N. Aseev *et al.*, "An upper limit on electron antineutrino mass from Troitsk experiment," arXiv:1108.5034 [hep-ex].

[26] C. Kraus *et al.*, "Final Results from phase II of the Mainz Neutrino Mass Search in Tritium β Decay," *Eur. Phys. J.* **C40** (2005) 447–468, arXiv:hep-ex/0412056.

[27] **KATRIN** Collaboration, J. Wolf, "The KATRIN Neutrino Mass Experiment," *Nucl. Instrum. Meth.* **A623** (2010) 442–444, arXiv:0810.3281 [physics.ins-det].

[28] K. Ichikawa, "Neutrino mass constraint from CMB and its degeneracy with other cosmological parameters," *J. Phys. Conf. Ser.* **120** (2008) 022004, arXiv:0711.2622 [astro-ph].

[29] C. Giunti, "Neutrino Flavor States and the Quantum Theory of Neutrino Oscillations," *AIP Conf. Proc.* **1026** (2008) 3–19, arXiv:0801.0653 [hep-ph].

[30] M. Goeppert-Mayer, "Double beta-disintegration," *Phys. Rev.* **48(6)** (1935) 512–516.

[31] V. Kolhinen, T. Eronen, D. Gorelov, J. Hakala, A. Jokinen, *et al.*, "Double-beta decay Q value of Nd-150," *Phys.Rev.* **C82** (2010) 022501.

[32] W. H. Furry, "On transition probabilities in double beta- disintegration," *Phys. Rev.* **56** (1939) 1184–1193.

[33] S. Bilenky, "Neutrinoless double beta-decay," *Phys.Part.Nucl.* **41** (2010) 690–715, arXiv:1001.1946 [hep-ph].

[34] A. Dueck, W. Rodejohann, and K. Zuber, "Neutrinoless Double Beta Decay, the Inverted Hierarchy and Precision Determination of theta(12)," *Phys. Rev.* **D83** (2011) 113010, arXiv:1103.4152 [hep-ph].

[35] C. Aalseth, F. Avignone, R. Brodzinski, W. Hensley, H. Miley, *et al.*, "Recent results of the IGEX Ge-76 double-beta decay experiment," *Phys.Atom.Nucl.* **63** (2000) 1225–1228.

[36] H. Klapdor-Kleingrothaus, A. Dietz, and I. Krivosheina, "Critical view to 'The IGEX neutrinoless double beta decay experiment'(Phys.Rev.D65:092007,2002)," *Phys.Rev.* **D70** (2004) 078301, arXiv:hep-ph/0403056 [hep-ph].

[37] C. Aalseth, F. Avignone, R. Brodzinski, S. Cebrian, E. Garcia, *et al.*, "The IGEX experiment revisited: A Response to the critique of Klapdor-Kleingrothaus, Dietz and Krivosheina," *Phys.Rev.* **D70** (2004) 078302, arXiv:nucl-ex/0404036 [nucl-ex].

[38] L. Baudis, M. Gnther, J. Hellmig, G. Heusser, M. Hirsch, H. Klapdor-Kleingrothaus, H. Ps, Y. Ramachers, H. Strecker, M. Vllinger, A. Bakalyarov, A. Balysh, S. Belyaev, V. Lebedev, S. Zhoukov, and S. Kolb, "The heidelberg-moscow experiment: improved sensitivity for 76ge neutrinoless double beta decay," *Physics Letters B* **407** no. 3-4, (1997) 219 – 224. http://www.sciencedirect.com/science/article/pii/S0370269397007569.

[39] H. V. Klapdor-Kleingrothaus and I. V. Krivosheina, "The evidence for the observation of 0nu beta beta decay: The identification of 0nu beta beta events from the full spectra," *Mod. Phys. Lett.* **A21** (2006) 1547–1566.

[40] **NEMO** Collaboration, J. Argyriades *et al.*, "Measurement of the Double Beta Decay Half-life of 150-Nd and Search for Neutrinoless Decay Modes with the NEMO-3 Detector," *Phys. Rev.* **C80** (2009) 032501, arXiv:0810.0248 [hep-ex].

[41] N. Ackerman *et al.*, "Observation of Two-Neutrino Double-Beta Decay in Xe-136 with EXO-200," arXiv:1108.4193 [nucl-ex].

[42] **EXO** Collaboration, R. Gornea, "Search for neutrino-less double beta decay with EXO-200 TPC and prospects for barium ion tagging in liquid xenon," *J. Phys. Conf. Ser.* **309** (2011) 012003.

[43] F. Alessandria *et al.*, "Sensitivity of CUORE to Neutrinoless Double-Beta Decay," arXiv:1109.0494 [nucl-ex].

[44] A. S. B. S. Collaboration), "Supernemo double beta decay experiment," in *Proceedings of the 12th International Conference of Topics in Astroparticle and Underground Physics*. September, 2011.

[45] **GERDA** Collaboration, H. Simgen, "Status of the GERDA experiment," *J. Phys. Conf. Ser.* **120** (2008) 052052.

[46] A. K. S. Collaboration), "Status of the kamland-zen experiment," in *Proceedings of the 12th International Conference of Topics in Astroparticle and Underground Physics*. September, 2011.

[47] **SNO** Collaboration, J. B. et al, "The sudbury neutrino observatory," *Nucl. Instrum. Meth.* **A449** (2000) 172–207.

[48] M. Chen. Private communication, 2011.

[49] B. S. A. Hamer, "Targets for the n16 calibration source." Sno-str-97-033, Aug, 1997.

[50] B. Moffat, R. Ford, F. Duncan, K. Graham, A. Hallin, *et al.*, "Optical calibration hardware for the sudbury neutrino observatory," *Nucl.Instrum.Meth.* **A554** (2005) 255–265, `arXiv:nucl-ex/0507026 [nucl-ex]`.

[51] A. Wright, "Lab optics report." Sno-doc-219-v1, Oct, 2008.

[52] H. C. Tseung, J. Kaspar, and N. Tolich, "Measurement of the dependence of the light yields of linear alkylbenzene-based and EJ-301 scintillators on electron energy," *Nucl.Instrum.Meth.* **A654** (2011) 318–323, `arXiv:1105.2100 [nucl-ex]`. * Temporary entry *.

[53] B. Krosigk, "Optical measurements lab." Sno-doc-805-v1, Feb, 2011.

[54] H. S. W. C. Tseung, "Birks' constant and alpha quenching factors from bucket." Sno-doc-905-v1, Mar, 2011.

[55] F. Boehm and P. Vogel, *Physics of Massive Neutrinos.* CUP, 1987.

[56] N.A.Jelley, *Fundamentals of nuclear physics.* CUP, 1990.

[57] R. Biggs. Private communication, 2011.

[58] M. D. Lay, *Creation and Detection of Čerenkov Light in the Sudbury Neutrino Observatory.* PhD thesis, University of Oxford, 1994.

[59] R. J. Boardman, *The Detection of Čerenkov Radiation from Neutrino Interactions.* PhD thesis, University of Oxford, 1992.

[60] M. E. Moorhead, *Reflectors in Čerenkov Detectors.* PhD thesis, University of Oxford, 1992.

[61] S. Gil, G. A. Clarke, L. McGarry, and C. Waltham, "Determination of absolute specular reflectivities in liquid media with variable angles of incidence," *Applied Optics* **34** (1995) 695–702.

[62] R. Dosajnh, "'end-of-salt' optics extraction (version 1.2)." Sno internal, Feb, 2004.

[63] M. Lay, "Parameterisation of the angular response of the R1408 Hamamatsu eight-inch photomultiplier tube to be used in the Sudbury Neutrino Observatory," *Nucl.Instrum.Meth.* **A383** (1996) 485–494.

[64] J. D. *et al*, "Optics6b." Sno internal, Apr, 2001.

[65] S. D. Biller, N. A. Jelley, M. D. Thorman, N. P. Fox, and T. H. Ward, "Measurements of photomultiplier single photon counting efficiency for the Sudbury Neutrino Observatory," *Nucl. Instrum. Meth.* **A432** (1999) 364–373.

[66] "Aluminium refractive indices.". http://refractiveindex.info/?group=METALS\&material=Aluminium.

[67] T. Latorre. Private communication, 2011.

[68] P. A. Cerenkov, "Visible radiation produced by electrons moving in a medium with velocities exceeding that of light," *Phys. Rev.* **52** (1937) 378–379.

[69] I. Coulter. Private communication, 2011.

[70] H. M. O'Keeffe, E. O'Sullivan, and M. C. Chen, "Scintillation decay time and pulse shape discrimination in oxygenated and deoxygenated solutions of linear alkylbenzene for the SNO+ experiment," *Nucl. Instrum. Meth.* **A640** (2011) 119–122, arXiv:1102.0797 [physics.ins-det].

[71] S. Morgan, "Characterisation and analysis of total internal reflection and refraction effects at sno+," Master's thesis, University of Oxford, 2010.

[72] T. Iwamoto, *Measurement of Reactor Anti-Neutrino Disappearance in KamLAND*. PhD thesis, Tohoku University, 2003.

[73] F. James and M. Roos, "Minuit - a system for function minimization and analysis of the parameter errors and correlations," *Comput. Phys. Commun.* **10** (1975) 343–367.

[74] M. G. Boulay, *Direct Evidence for Weak Flavour Mixing with the Sudbury Neutrino Observatory*. PhD thesis, Queen's University, 2001.

[75] **KamLAND** Collaboration, S. Abe *et al.*, "Measurement of the 8B Solar Neutrino Flux with the KamLAND Liquid Scintillator Detector," arXiv:1106.0861 [hep-ex].

[76] R. B. Firestone, *Table of Isotopes*. John Wiley and Sons, 1996.

[77] J. N. Bahcall *et al.*, "Standard Neutrino Spectrum from 8B Decay," *Phys. Rev.* **C54** (1996) 411–422, arXiv:nucl-th/9601044.

[78] J. R. Wilson, *A Measurement of the ^8B Solar Neutrino Energy Spectrum at the Sudbury Neutrino Observatory.* PhD thesis, University of Oxford, 2004.

[79] **SNO Collaboration** Collaboration, B. Aharmim *et al.*, "Measurement of the Cosmic Ray and Neutrino-Induced Muon Flux at the Sudbury Neutrino Observatory," *Phys.Rev.* **D80** (2009) 012001, arXiv:0902.2776 [hep-ex].

[80] B. von Krosigk, "Cosmic muon activation with emphasis on 11c." Sno-doc-711-v1, April, 2011.

[81] M. C. Helen O'Keeffe, "Expected radioactive backgrounds in sno+." Sno-doc-507-v2, May, 2010.

[82] J. Maneira, "External background in sno+t." Sno-doc-43-v1, August, 2007.

[83] R. Ford, M. Chen, O. Chkvorets, D. Hallman, and E. Vazquez-Jauregui, "SNO+ scintillator purification and assay," *AIP Conf.Proc.* **1338** (2011) 183–194.

[84] I. L. Bruce Cleveland, "Recent gamma activity measurements of several high-purity nd samples with the snolab ge detector." Sno-doc-509-v1, May, 2010.

[85] H. O'Keeffe, "Temperature dependent measurement of the density of lab." Sno-doc-276-v1, Apr, 2009.

[86] S. Quirk, "Solar neutrino studies." Sno-doc-83-v1, Nov, 2007.

[87] A. Wright, "Pileup studies." Sno-doc-118-v2, Jan, 2008.

[88] H. M. O'Keeffe, *Low Energy Background in the NCD Phase of the Sudbury Neutrino Observatory.* PhD thesis, University of Oxford, 2008.

[89] T. Junk, "Confidence Level Computation for Combining Searches with Small Statistics," *Nucl. Instrum. Meth.* **A434** (1999) 435–443, arXiv:hep-ex/9902006.

[90] A. L. Read, "Modified frequentist analysis of search results (The CL(s) method),". Prepared for Workshop on Confidence Limits, Geneva, Switzerland, 17-18 Jan 2000.

[91] S. Biller and N. Fatemi-Ghomi, "Optimisation of detector parameters for enriched nd loading scenarios." Sno-doc-1153-v1, Sep, 2011.

[92] N. Fatemi-Ghomi, "Double beta decay plots." Sno-doc-1137-v4, Sep, 2011.